UPC **CTTC**

Application of experimental and numerical methodologies for the development of an absorption heat pump for solar-driven systems

Centre Tecnològic de Transferència de Calor
Departament de Màquines i Motors Tèrmics
Universitat Politècnica de Catalunya

Jian Zheng
Doctoral Thesis

Application of experimental and numerical methodologies for the development of an absorption heat pump for solar-driven systems

Jian Zheng

TESI DOCTORAL

presentada al

Departament de Màquines i Motors Tèrmics
ESEIAAT
Universitat Politècnica de Catalunya

per a l'obtenció del grau de

Doctor per la UPC

Terrassa, March 30, 2023

Application of experimental and numerical methodologies for the development of an absorption heat pump for solar-driven systems

Jian Zheng

Directors de la Tesi

Dr. Jesús Castro González
Dr. Joaquim Rigola Serrano

Tutor

Dr. Asensio Oliva Llena

Tribunal Qualificador

Dr. José Fernandez Seara
Universidade de Vigo

Dr. Carlos David Perèz Segarra
Universitat Politècnica de Catalunya

Dr. Francisco Javier Rey
Universidad de Valladolid

Acknowledgements

Gracias a Outong Li, mi esposa y entrañable compañera. Gracias por tu compañía y compresión incondicional, en los periodos duros siemple me anima y apoya.

Gracias a mis padres con su soporte y comprensión.

Al Doctor Jeśus Castro, director de esta tesis, por su consejo y orientación, me ha permitido siempre avanzar y llegar a donde nunca hibiese creído. Gracias por la guía al camino académico y conocimientos en ambos simulación y experimentos.

Al Doctor Joaquim Rigola, tutor de esta tesis, por su orientación y inspiración en transferencia de calor y masa.

Al Doctor Assensi Oliva, que me dio muchas oportunidades y confianza.

A Manuel Ordoño, por el apoyo referente al técnico, mecánico. Que descanse en paz.

A Doctor Joan Farnós y Doctor Giorgos Papakokkinos, por el soporte y inpiración en absorción en experimentos y simulación.

A Victor Ruíz y Octavio Pavon, por el soporte y ayuda en electrónico y gestión general.

A todos los miembros del Centre Tecnològic de Transferència de Calor.

Contents

Abstract

In this dissertation, a small capacity (<30kW) solar-driven absorption machine is under investigation in terms of various characteristics. With the increased energy consumption condition, solar-driven climatization systems in industrial and commercial applications have driven more and more attention. However, these systems encounter many challenges in design and optimization. To improve the working performance and convert the absorption chiller to a heat pump, an already existent air-cooled absorption chiller prototype using water as a refrigerant in solar thermal systems is studied.

In Chapter 2, details of the thermophysical properties of the working pairs for the absorption system are studied. LiBr-H_2O, one of the most commonly used working pairs in the absorption system, and Carrol-H_2O are studied here (Carrol contains LiBr:Ethylene glycol with a weight ratio of 4.5:1), the last option to reduce crystallization risk. Though thermophysical properties are detailed and reported in much literature, some information is still limited, especially for Carrol-H_2O. The properties like activity coefficient, electrical conductivity, surface tension and contact angle are reported in this section.

In Chapter 3 the Minimum Wetting Rate (MWR) of the liquid falling film is modelled and experimentally validated with various fluids and surfaces. The MWR for the H_2O and LiBr-H_2O is around 0.1 $kgm^{-1}s^{-1}$, and the value could be reduced to 0.025 $kgm^{-1}s^{-1}$ when the hydrophilic coated surface is employed.

In Chapter 4, heat and mass transfer coefficients are investigated with simulations and experiments, with an emphasis on studying the influence of Al_2O_3 nanoparticles. The results show that nanoparticle could improve the heat and mass transfer coefficient for both working pairs. When the volumetric concentration of Al_2O_3 is around 4%, the vapour absorb rate for Carrol-H_2O could increase about 15-20%.

In Chapter 5 and 6 the system performance of the absorption machine is studied under cooling and heating application. As a culmination of the falling film studies, a sensitivity study is performed to assess the impact of different heat and mass enhancements on the absorption machine performance at a system level. The absorption machine with LiBr-H_2O at chiller application has a cooling capacity of around 6-8 kW with a coefficient of performance (COP) at 0.75. While as an absorption heat pump the heating capacity is around 15-20 kW with a coefficient of performance (COP) at around 1.6. The enhancements like surfactant, nanofluid, and mechanical vibration could improve the total working capacity by around 5-10%.

In Chapter 7, the integration of the absorption machine in a solar heating/cooling system is also studied, using a new concept of a high-performance flat plate solar thermal collector as the heat source based on Transparent Insulation Materials (TIM). For such purposes, system simulations are carried out using LiBr-H_2O and Carrol-H_2O as working fluids in heating and cooling applications with energy and exergy analysis. The solar collector has an efficiency of around 50-70% depending on the inlet water temperature. In summer, if the absorption chiller works non-stop for 24 h for 5 days, the solar-heated water could supply more than 60% of the total energy consumption while in winter the value change to 10-50% due to the weather condition change.

1

Introduction

Abstract

This first chapter presents a general overview of the work carried out. First, the motivation for the work performed is explained in the framework of the present global objective of CO_2 emissions reduction. Then, some fundamentals of several thermal-driven technologies for heating/cooling production are explained, emphasizing the absorption technology, the technology employed in this thesis. In the next section, a brief review of working fluid pairs for absorption technology is performed. Then, in the following two sections, a description of the absorption chiller prototype and flat plate solar thermal collector object of study is done. Furthermore, the following section explains a brief state of the art of small-capacity absorption systems development. Finally, the last two sections explain briefly the objectives and structure of this thesis, respectively.

1.1 Global energy consumption and CO_2 emission policies

Nowadays, the continuous increase in the world's primary energy consumption is a challenge to the sustainability development of modern industries. According to a recent British Petroleum (BP) report [1], in the last two years, renewables have grown more than the combined increase in coal and natural gas supplies. Meanwhile, in 2021, the primary energy consumption grew by 31 EJ, becoming the largest increase in history and more than reversing the sharp decline seen in 2020. Therefore, the global CO_2 emission reached 36.3 billion tonnes. This fact makes the target plan of cutting greenhouse gas emissions by at least 55% by 2030 proposed by the European Commission more relevant. In 2020, natural gas accounted for 31.7% of the EU final energy consumption in households, electricity for 24.8%, renewables and wastes for 20.3%, and oil & petroleum products for 12.3%(Eurostat 2020 [2]). Renewable energy consumption share in the whole market has been increasing in the recent decade, being distributed in many sectors. And worldwide, using air conditioners and electric fans to cooling accounts for nearly 20% of the total electricity used in buildings according to IEA [3]. Compared to the power generation sector, the transition to renewable energy sources and other low-carbon solutions in the heating and cooling sector has been slow, with only 23% of its energy consumption being supplied by these sources (Eurostat 2020 [2]). Replacing conventional vapor compression systems with solar-driven absorption climatization systems could represent a significant opportunity for reducing electricity consumption and mitigating associated greenhouse gas emissions.

1.2 Fundamentals of the solar-driven absorption system

1.2.1 The basic principle of absorption system and other thermal-driven systems

In terms of climatization or refrigeration technologies, many methods have been proposed or are used under various conditions. The most widely employed climatization applications currently are based on vapour compression. It is either electricity-based, taking the electricity from the net supply, or through an electricity generator that uses fossil fuels. Thermal-based systems using renewable energy could be an alternative option, but they still don't have an important role compared with the vapour compression system due to their limited performance, maturity, complexity, etc. However, they could be interesting if the thermal energy available has a low price, e.g., solar energy. One of the most used thermal-driven technologies for heating and cooling applications is the Rankine cycle. As shown in Figure 1.1, the Rankine cycle is a hybrid option, as they use a vapour compression cycle using mechanical work from a turbine of the vapour power cycle. The main components in the Rankine cycle are the boiler, pump, turbine and condenser. The liquid is delivered to the boiler by the pump and converted to vapour to power the turbine. Meanwhile, in the sorption systems, the mechanical compressor is replaced with a thermochemical compressor which also could transport vapour from low pressure to high pressure. Absorption and adsorption systems are shown in Figure 1.2 and 1.3, respectively. In an absorption system, the absorber transports refrigerant

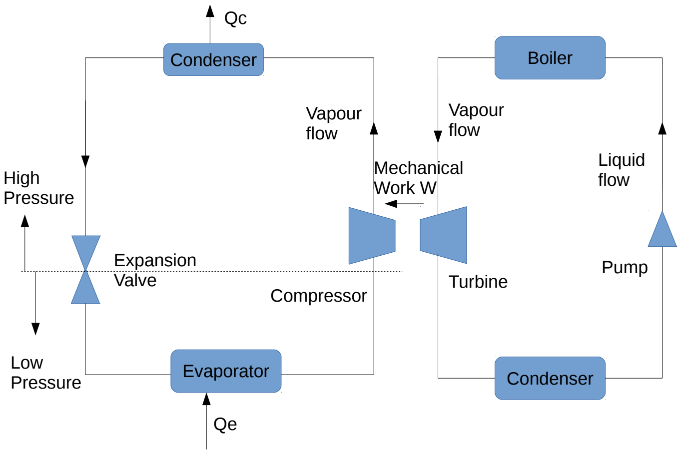

Figure 1.1: A sketch of a Rankine circle

vapor from a low-pressure to high-pressure area through thermodynamic equilibrium with the absorbent liquid solution. The refrigeration process occurs in the evaporator as the vapor is continuously absorbed. In contrast, in the adsorption system, the sorption process may be continuous or separated. In the separated process, the reactor works either as a generator or adsorber during different working periods, while in the continuous process, the desiccant wheel works as both a generator and adsorber, depending on the position. The operations of absorption and adsorption systems differ as shown below:

- In the absorption system, as shown in Figure 1.2, the absorbent solution will be circulated between the generator and absorber. The heat source operates in the generator to concentrate the solution. The high-concentration solution enters the low-pressure absorber, where this solution absorbs refrigerant vapour from the evaporator while it is cooled down. The refrigerant vapour generated from the generator enters the condenser, where it is turned into liquid. Finally, the evaporator turns the liquid refrigerant into vapor after an expansion process. The condenser and absorber will eject heat, while the generator and evaporator will absorb heat.

- In the adsorption system, as shown in Figure 1.3a, the reactor represents the

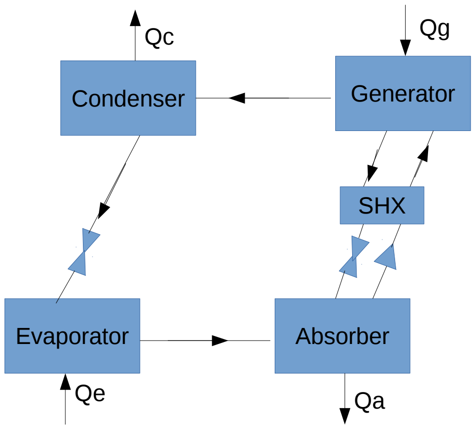

Figure 1.2: A sketch of absorption system

generator and adsorber, working in an intermittent procedure. When the reactor is used as an adsorber (gate valve 1 is open, and gate valve 2 is closed), the reactor will adsorb vapour from the evaporator while it is cooled down. In the desorption process (gate valve 1 is closed and gate valve 2 is open), the reactor is operated by the heat source, and the vapour leaves the reactor and enters the condenser, and finally enters the reservoir, which is connected to the evaporator, hence, a closed system. On the other hand, the system could also be continuous as shown in Figure 1.3b.

The traditional refrigerants in the vapour compression systems in climatization commonly used as hydro−chloroflurocarbons and hydrofluorocarbons have a significant effect on greenhouse gas emissions, as the global warming potential is of the order of 1000 times higher than CO_2 according to Cui et al. [4]. The refrigerant in this study is H_2O, which could grant eco-friendly advantages. Moreover, the heat source could be waste heat or other renewable energy, such as solar thermal energy.

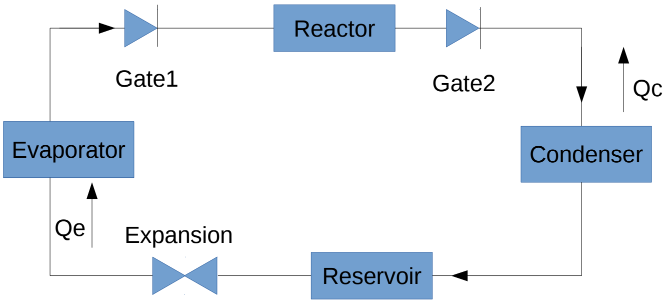

(a) A sketch of adsorption system with intermittent procedure

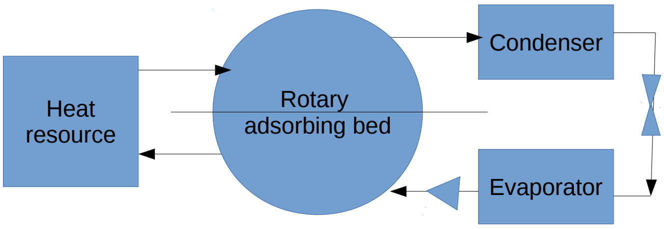

(b) A sketch of adsorption system with continuous procedure

Figure 1.3: Sketches of adsorption systems

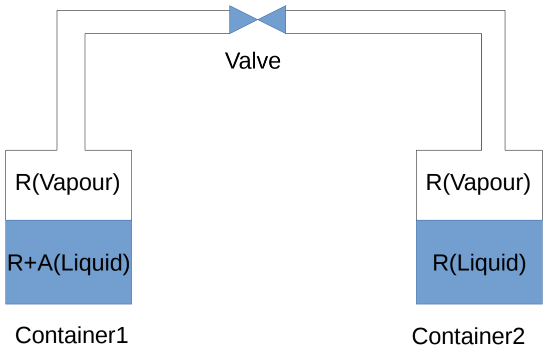

Figure 1.4: A sketch of thermodynamic equilibrium example, where R represents refrigerant and A is absorbent

1.2.2 Basic absorption thermodynamics

In the absorption system, see Figure 1.2, when the concentrated solution from the generator at high pressure enters the absorber at low pressure, the thermodynamic equilibrium changes. Along with the cooling down process of the liquid solution, the solution becomes subcooled and tends to absorb refrigerant vapour to maintain thermodynamic equilibrium at the corresponding pressure.

The principle of operation of an absorption system, based on thermodynamic equilibrium, is shown in Figure 1.4. In container 1 of refrigerant and absorbent, the conditions satisfy the thermodynamic equilibrium $P = f_{1,\mathrm{eq}}(T,C)$, and in container 2 of pure refrigerant, the condition is $P = f_{2,\mathrm{eq}}(T)$. The liquid solution has a lower equilibrium pressure than pure water at the same temperature. In contrast, if the pressure is the same, the saturated temperature for water is lower. Meanwhile, the water vapour that leaves from the solution has a similar temperature as the liquid, so the water vapour is superheated vapour. For example, according to the liquid and solution thermophysical properties extracted from [5], [6], [7], at 1000 Pa, the saturated temperature for pure water is around 7°C, and for 60% LiBr and Carrol solution, the saturation temperature is 46.6 and 33.2 °C, correspondingly. If the two vessels are connected like in Figure

1.4, by introducing a secondary circuit in the liquid side, the regulation of the solution temperature leads to the absorbing/desorbing process, according to the thermodynamic equilibrium condition. In the generator, a secondary circuit provides heat to the solution. The vapour produced leaves the generator, so the solution concentrates with the heat supplied. The concentrated solution will be cooled down and injected into the absorber. In this process, the liquid solution can be easily overcooled and encounter crystallization problems. The crystallization is a common problem in the absorption system in the salt-based circle if the condition is below the crystallization line of the salt. The dissolved electrolyte will precipitate in the solution and attributes of the resulting crystal. The solid precipitation may significantly affect the system performance and risk damaging the solution pump. In the design of the absorption machine, the crystallization issue is a relevant question to consider.

1.3 Working fluid pairs

Many reviews of working pairs (absorbent - refrigerant) of the absorption system discuss the possibilities of the different options [8], [9], [10], [11]. Besides, requirements for the working pairs are listed in [12],

- The difference in equilibrium pressures between refrigerant and absorbent should be as high as possible.
- Refrigerant should have high heat of vaporization and high concentration within the absorbent in order to maintain a low circulation rate between the generator and the absorber per unit of cooling capacity.
- Transport properties that influence heat and mass transfer, e.g., viscosity, thermal conductivity, and mass diffusion coefficient, should be favourable.
- Both refrigerant and absorbent should be non-corrosive, environmentally friendly, and low-cost.

With information from the literature, the refrigerant-absorbent could be NH_3 - (H_2O, $LiNO_3$, NaSCN, Ionic Liquids), H_2O - (LiBr, LiCl, $CaCl_2$ Ionic Liquids), HFC - (Organic absorbents), or Alcohol - (Organic Solvents). Both working pairs have their advantages and drawbacks. However, only two working pairs are widely used in the market, $H_2O{-}LiBr$, and $NH_3{-}H_2O$ due to the requirements mentioned above. For solar-driven air-cooled absorption heat pump (AHP)/ chiller (AC), only a system from Purix (2.5kW

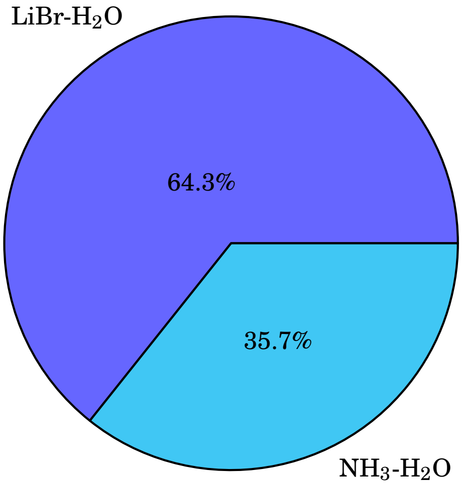

Figure 1.5: Market share of brands by working fluid according to [10]

cooling, 3.5kW heating) is available on the market with the working pairs LiBr-H_2O. Besides simple working pairs with absorbent-refrigerant, many authors also developed ternary or more species for the working fluid to acquire better performance. [13] and [14] did research about NH_3-H_2O-LiBr mixtures in an absorption heat pump and the *COP* of the mixture is higher than NH_3-H_2O. Moreover, additives to working pairs $LiBr-H_2O$ are also studied in many cases, [15] added $HO(CH_2)_3OH$, [16] added CH_3COOK and $CH_3CH(OH)COONa$, [17] used mixture of CHO_2Na and CHO_2K. Generally, the additive could reduce the crystallization risk and increase temperature lift or *COP*. Other more complicated systems are also studied, Saravanan et al. [18] did the thermodynamic analysis with various mixtures and found that H_2O-LiCl has favourable conditions from the point view of cut-off temperature and circulation ratio and H_2O+LiBr+LiCl+$ZnCl_2$ was better from the COP and efficiency ratio. On the other hand, the single-stage absorption chillers market is dominated by NH_3-H_2O and LiBr-H_2O while other working pairs are most studied in the experimental prototypes or simulations. Figure 1.5 and 1.6 show the most used working pairs in industrial applications and experimental prototype investigation.

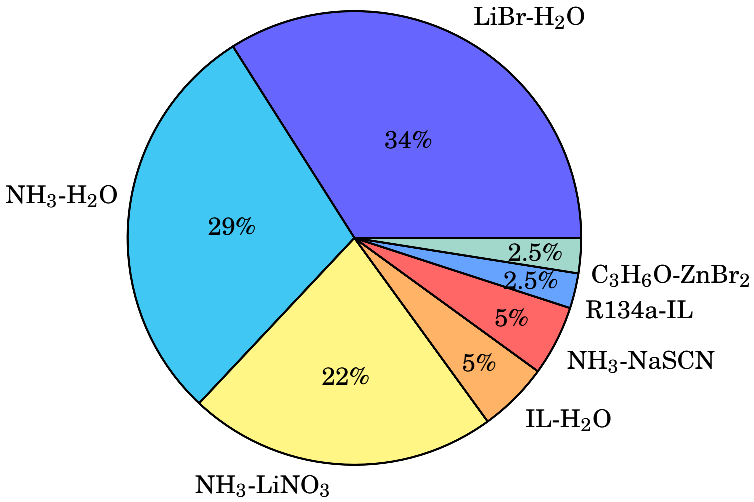

Figure 1.6: Percentage of the experimental prototypes developed during the past 35 years according to [10]

1.4 Heat exchangers in the absorption machine prototype

A direct air-cooled LiBr−H_2O compact absorption machine (pre-industrial prototype) was built by Castro in his dissertation [19] and further developed by Farnós in this dissertation [20]. In those works, the prototype was constructed from scratch according to the detailed simulation. To further investigate the performance and the possible improvements, the machine was torn apart with main components such as the generator, absorber, evaporator, condenser, solution pump, solution heat exchanger, and other auxiliary components. From the current condition, new proposals for transforming the prototype from an absorption chiller to an absorption heat pump have been carried out. In the absorption chiller mode, the evaporator will absorbe heat from secondary circuit to chill liquid stream like water while in the absorption heat pump mode, the condenser and absorber will reject heat for the climatization use.

- Horizontal falling film heat exchanger
  The horizontal falling film heat exchanger is widely used in many applications. Figure 1.7 shows the flow pattern of a horizontal tube, falling film heat exchanger. Due to the limited mass flow rate and space, the falling film design could ensure the contact area of the solution with the tube serpentine if complete wettability is

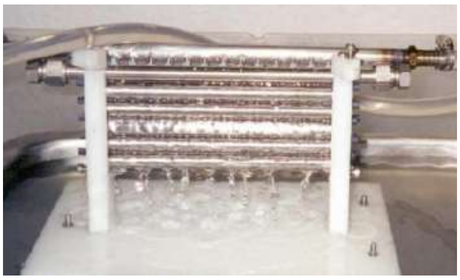

Figure 1.7: Flow pattern of a horizontal falling film over tube bundle in Castro [19]

Figure 1.8: A horizontal falling film type generator for a 10 kW absorption machine in [20]

achieved. A generator of the machine prototype is shown in Figure 1.8: the front metal plate was cut off to check the component's state after years of experiments. The tube bundle employed inside the generator is similar to Figure 1.9. Hot water travels inside the serpentine, and diluted solution flows over the tube bundle as a horizontal falling film and is heated by the horizontal tubes. During this heating process, the diluted solution will generate refrigerant vapour that goes into the condenser, and subsequently, the salt concentration increases. Then the concentrated solution enters the solution heat exchanger.

- Air-cooled, vertical falling film heat exchangers (condenser and absorber)
  Vertical falling film heat exchangers could be either vapour-to-air or liquid-to-air.

Figure 1.9: Heat exchanger for liquid-liquid SS serpentine in [20]

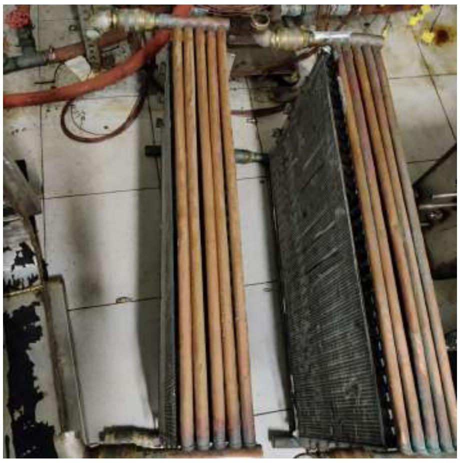

Figure 1.10: Air-cooled condensers in [20]

In the condenser, see Figure 1.10, the overheated vapour stream enters the heat exchanger and is distributed inside the tube bundle. Outside, the air cools down the tube. Therefore, the vapour condenses on the tube wall, and the liquid falls to the vessel and enters the evaporator through an expansion valve, as the pressure in the condenser is higher than in the evaporator.

Concerning the absorber, see Figure 1.11, the concentrated subcooled solution enters this heat exchanger and is distributed by a panel-distributed system. The mainstream is divided into hundreds of small flows and enters the distributor of each tube. The solution flow will form an annular film inside each tube, ensuring the contact area of the liquid and heat exchanger tube and a similar contact area for the vapour absorption. Alongside the finned tube, the temperature will decrease, and under the same pressure, the concentrated solution will absorb

Figure 1.11: Vertical falling film type absorber in [20]

refrigerant vapour to maintain equilibrium conditions. Finally, the diluted solution will enter a vessel, then it is pumped into the solution heat exchanger and evantually reaches the generator.

- Pool boiling evaporator
  The refrigerant vapour absorbed inside the absorber comes from the evaporator, as these two components are generally directly connected. The heat exchanger type of the evaporator could be pool boiling or horizontal falling film. In our case, the pool boiling design is chosen to avoid an additional refrigerant pump. The pool boiling evaporator of the prototype is shown in Figure 1.12. It has to be remarked that the tube serpentine is finned to increase the heat exchanger area. The liquid water from the condenser is heated by the secondary finned serpentine of the evaporator, as shown in Figure 1.13. Therefore, the liquid will boil inside the evaporator, and the vapour enters the absorber.

- Solution heat exchanger, solution pump, valves, sensors, ventilation system.
  Besides of the main components, a solution pump is employed to circulate the solution between the generator and the absorber. The solution from the generator travels to the absorber driven by the gravity and the pressure difference between the generator and absorber, in which the solution heat exchanger is utilized as an expansion valve and to preheat the cooled diluted solution from absorber to

Figure 1.12: A pool boiling type of evaporator in [20]

Figure 1.13: Heat exchanger for liquid-liquid copper finned serpentine before installation in Figure 1.12

generator. Two fans were set on top of the machine to cool down the absorber and condensor. To vigilant the system performance, temperature, pressure sensors and flowmeter are set in the system to record the working condition. Additional valves are set between components to control the operation of the machine.

1.5 Solar thermal collector

Solar thermal collectors operated under medium temperatures have different technologies in the current market. Besides flat plat solar collectors (FPC) 30-80°C, stationary compound parabolic collectors (CPC) 60-240°C, evacuated tubes collectors (ETC) 50-200°C, Linear Fresnel reflector (LFR) 60-300°C, small parabolic trough collectors (PTC), and cylindrical trough collectors (CTC) 60-300°C are other technological alternatives widely investigated according to Kalogirou [21]. Considering the cost, temperature range and maturity, FPC is the optimal heat source for solar absorption climatization. Since the conventional FPC has a limited working performance and temperature range, an evolution of the prototype of FPC with Transparent Insulation Material(TIM) developed by Kessentini et al. [22] at CTTC is used here. The target is operating at temperatures between 80-120◦C. Also, a new prototype is shown in Figure 1.14. The solar-heated water will be stored in an insulated tank and could be employed as the heat source in the absorption climatization system.

A scheme of the solar thermal collector is represented in Figure 1.15. The solar radiation passes through a high transmittance glass, a TIM layer, another glass cover, an aerogel layer and finally reaches the absorber. The whole system should be well insulated. In Figure 1.15, the water is circulated inside the absorber, and the tube is connected to the absorber copper plate, which is shown in Figure 1.16.

Figure 1.14: A FPC collector with TIM and aerogel of previous work [23], [24]

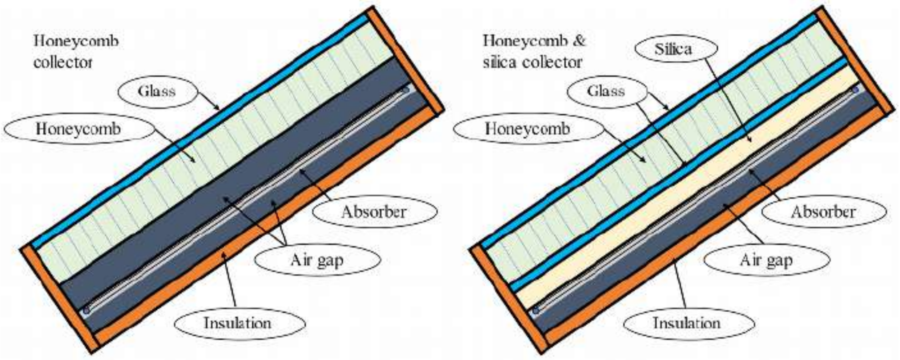

Figure 1.15: Sketch of FPC with only TIM [22], [25] (left) and sketch of FPC with aerogel and TIM [23], [24] (right)

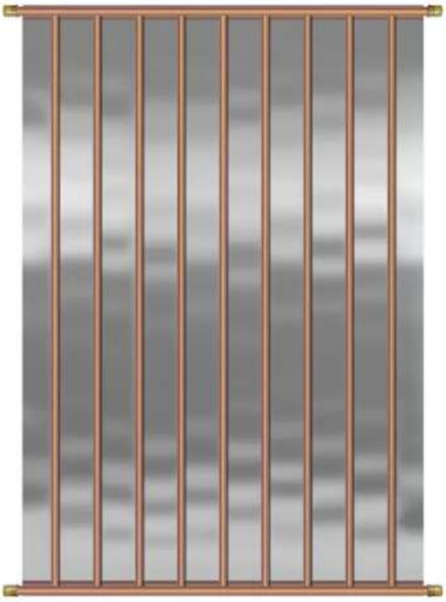

Figure 1.16: Solar absorber used in the Figure 1.15

1.6 Small capacity absorption systems on the commercial market and academic prototype investigation

Though the market share of the absorption climatization system only occupies a non-significant part, many companies have been working on this topic as shown in Table 1.1. Besides, all the models are absorption chillers, there is the neither available commercial unit for the absorption heat pumps nor air-cooled absorption unit.

In this thesis, the development of the absorption system is based on a prototype described in previous works [19, 20], which is a direct air-cooled machine driven by hot water. This system can also operate at subzero temperatures at the evaporator by using water as a refrigerant.

Table 1.1: Commercial products of small absorption system comparison

Company	Yazaki	Sonnenklima	Rotartica	Climatewell	SolarNext	SorTech	SJTU	Lucy New Energy
Country	Japan	Germany	Spain	Sweden	Germany	Germany	China	China
Product name	WFC-SC5	Suninverse 10	Solar045	Chimatewell 10	chillii PSC12	CS 08	SWAC-10	RXZ-11
Technology	absorption	absorption	absorption	absorption	absorption	absorption	adsorption	absorption
Working pairs	LiBr-H_2O	LiBr-H_2O	LiBr-H_2O	LiBr-H_2O	LiCl-H_2O	H_2O-NH_3	Silica gel-H_2O	LiBr-H_2O
Cooling capacity[kW]	17.6	10	4.5	11	10	12	15	10
Heating temperature[°C]	88/83	75/65	90/85	83	85/78	75/68	85/79	90/85
Cooling type	Water cooled	Water cooled	Water cooled	Water cooled	Water cooled	Water cooled	Water cooled	Water cooled
Cold water temperature [°C]	12.5/7	18/15	13/10	15	12/6	18/15	15/10	15/10
COP	0.70	0.77	0.67	0.68	0.62	0.56	0.39	0.72
Dimensions (L*W*H) [m*m*m]	0.6*0.8*1.94	1.13*0.8*1.96	1.09*0.76*1.15	1.2*0.8*1.6	0.8*0.6*2.2	0.79*1.06*0.94	1.8*1.2*1.4	1.07*0.93*1.65
Weight[kg]	420	550	290	875	350	260	1600	950

1.7 Numerical models for the solar heating/cooling absorption system and falling film heat & mass transfer processes

Numerical simulation is a helpful methodology for the development of an absorption machine. The resulting system performance includes the influence of the different components with complex geometries, where complex physical phenomena for the heat and mass transfer processes are involved. In order to solve and characterize such aspects, simplified semi-empirical models considering the computational cost have to be employed. [26, 27] developed steady-state simulation models to predict the performance of an absorption refrigeration system using LiBr-H_2O as a working pair. Evola et al. [28] proposed a model for the dynamic simulation of a solar-assisted single-stage LiBr-H_2O absorption chiller and validated the numerical model with a commercial absorption machine. In this dissertation, the numerical simulation is carried out on the NEST platform [29], [30]. In the platform each component is calculated as a single control volume, with inlet and outlet conditions to be solved. The models used in the simulation of the absorption system include both steady-state and dynamic conditions. In steady-state simulations, the system is assumed to be operated under certain fixed external conditions, so the performance is also maintained. Besides, in dynamic simulations, the system performs under transient external conditions. For example, long-term simulations with the whole solar heating/cooling systems are performed in transient conditions, as the metereological data varies with time. These dynamic simulations could demonstrate the design and optimization of the climatization system while investigating the near-real performance. Moreover, a multidimensional model is employed for studying the pure falling film heat and mass transfer problem with and without absorption by solving the coupled temperature and concentration distribution with an in-house code based on C++.

1.8 Research objectives

This thesis focuses on the evolution of an already-existent absorption chiller to a heat pump application for a solar-assisted system. The aspects studied are related to many aspects, such as working pairs, heat exchanger design, heat source design, exergy analysis, and control strategy basics. The research approach and methodology are based on the following two points:

- Numerical simulation. Both empirical correlation-based simulation at a system level and detailed multidimensional simulation for heat and mass transfer processes in falling film absorption are used to investigate and optimize the absorption system. The system simulation is helpful in predicting the system performance at steady-state and dynamic conditions. Exergy analysis is also utilized to optimise the absorption system design. In some cases, analytical solutions are employed to describe the problem, and mathematical modelling is used to calculate some thermodynamic and thermophysical properties.

- Experimental validations are also carried out to validate the numerical results. In this work, experiments for flat plate solar collector thermal characterization, and falling film temperature distribution measurement, have been performed. Moreover, some thermophysical properties, such as surface tension, contact angle, electrical conductivity, and nanofluid properties (thermal conductivity), are measured experimentally.

1.9 Structure and outlines of this thesis

The topics explained in this thesis are organized in different chapters. A summary of the contents is given below:

Chapter 2. Details of working pairs and properties with numerical modelling and experimental validation. Some thermodynamical/thermophysical properties of working fluid pairs are experimentally measured or mathematically modelled. The related properties are specific entropy, specific exergy, activity coefficients, electrical conductivity, surface tension, contact angle, and properties of nanofluid working pairs.

Chapter 3. Measurement of minimum wetting rate (MWR) and dry patch method modelling. MWR is measured on vertical tubes with various solid materials, and the effect of super hydrophilic coating surface and surfactant is studied. The content in this chapter is focused on the flow pattern of falling film and effect from surface treating, surfactants to it. The MWR on the stainless steel for the H_2O and LiBr-H_2O is around 0.1 $kgm^{-1}s^{-1}$, and the value could be reduced to 0.025 $kgm^{-1}s^{-1}$ when the hydrophilic coated surface is employed.

Chapter 4. Theoretical and numerical solutions of vertical falling film in mass and heat transfer problem. The heat transfer in the vertical falling film is investigated with analytical solutions, numerical modelling, and experimental validation. Also, falling film absorption is simulated using the smooth laminar theory for the working pairs LiBr-H_2O and Carrol-H_2O. Moreover, the impact of nanofluid with Al_2O_3 is also studied. The content in this chapter is focused on the heat and mass transfer of the vertical falling film. The results show that nanoparticle could improve the heat and mass transfer coefficient for both working pairs. When the volumetric concentration of Al_2O_3 is around 4%, the vapour absorb rate for Carrol-H_2O could increase about 15-20% with a coefficient of performance (COP) at around 1.6.

Chapter 5. Numerical studies on an air-cooled absorption machine. Steady-state and dynamic simulations for the absorption system with different working pairs (LiBr-H_2O and Carrol-H_2O) are carried out. Energy and exergy analysis is employed to demonstrate the effect of the working fluid pairs on the absorption system. In this chapter, the work will be focused on the energy and exergy analysis of the absorption system to locate an optimal operating condition or strategy. The absorption machine with LiBr-H_2O at chiller application has a cooling capacity of around 6-8 kW with a coefficient of performance (COP) at 0.75. While as an absorption heat pump the heating capacity is around 15-20 kW.

Chapter 6: Air-cooled absorption machine simulation with performance enhancement. Heat and mass transfer performance enhancements are employed in the simulation to predict enhanced performance. Surface treating components, surfactants, nanofluid, and mechanical vibration are studied to predict their effect on the final system performance. In this chapter, the work will be focused on the various methods of enhancements to the absorption system performance to achieve better performance. The enhancements like surfactant, nanofluid, and mechanical vibration could improve the total working capacity by around 5-10%.

Chapter 7. Integration of the air-cooled machine in a solar heating/cooling system. An FPC with TIM and aerogel is demonstrated for this work and described with experimental results. Then the solar collector is introduced to the absorption system as the heat source, and the whole system is simulated with the same platform. Meteorology data from Spain are employed to predict a long-term (5 days) real-time performance (winter and summer seasons) of the solar-assisted absorption system and the solar fraction. The solar collector has an efficiency of around 50-70% depending on the inlet water temperature. In summer, if the absorption chiller works non-stop for 24 h for 5 days, the solar-heated water could supply more than 60% of the total energy consumption while in winter the value change to 10-50% due to the weather condition change.

Chapter 8: General conclusions and future work.

NOMENCLATURE

Name	**Description**
C	Concentration [-]
COP	Coefficient of performance [-]
H	Height [m]
L	Length [m]
MWR	Minimum wetting rate [kg(m·s)$^{-1}$]
P	Pressure [Pa]
Q	Heat flux [kW]
T	Temperature [°C]
W	Width [m]
Abbreviation	**Description**
A	Absorbent
AC	Absorption chiller
AHP	Absorption heat pump
CPC	Compound parabolic collector
CTC	Cylindrical trough collector
ETC	Evacuated tube collector
LFR	Linear Frensnel reflector
PTC	Parabolic trough collector
R	Refrigerant
SHX	Solution heat exchanger
TIM	Transparent insulation material
Subscripts & Superscripts	**Description**
1,2	State point
a	Absorber
c	Condenser
e	Evaporator
g	Generator
eq	Equilibrium

References

[1] B. P. P.l.c., bp Statistical Review of World Energy (2022).

[2] Eurostat 2020, `https://ec.europa.eu/eurostat/data/database`.

[3] IEA, The Future of Cooling (2018).

[4] U. Energy, Buildings energy data book, Department of Energy.

[5] W. Biermann, Proprties of the Carrol system and a machine design for solar-powered, air-cooled, absorption space cooling. Phase I and Phase II. Final report, September 1977-March 1979, Tech. rep., Carrier Corp., Syracuse, NY (USA). Energy Systems Div. (1981).

[6] L. McNeely, Thermodynamic properties of aqueous solutions of lithium bromide, ASHRAE Transactions 85 (1) (1979) 413–434.

[7] A.~Kramida, Yu.~Ralchenko, J.~Reader, No Title, NIST Atomic Spectra Database (ver. 5.7.1), [Online]. Available: {\tt{https://physics.nist.gov/asd}} [2015, April 16]. National Institute of Standards and Technology, Gaithersburg, MD. (2019).

[8] J. Sun, L. Fu, S. Zhang, A review of working fluids of absorption cycles, Renewable and Sustainable Energy Reviews 16 (4) (2012) 1899–1906. `doi:10.1016/j.rser.2012.01.011`.

[9] L. Hui, N. K. Edem, L. P. Nolwenn, L. Luo, Evaluation of a seasonal storage system of solar energy for house heating using different absorption couples, Energy Conversion and Management 52 (6) (2011) 2427–2436. `doi:10.1016/j.enconman.2010.12.049`.

[10] A. Altamirano, N. L. Pierrès, B. Stutz, Review of small-capacity single-stage continuous absorption systems operating on binary working fluids for cooling: Theoretical, experimental and commercial cycles, International Journal of Refrigeration 106 (2019) 350–373. `doi:10.1016/j.ijrefrig.2019.06.033`.

[11] M. U. Siddiqui, S. A. M. Said, A review of solar powered absorption systems, Renewable and Sustainable Energy Reviews 42 (2015) 93–115. `doi:10.1016/j.rser.2014.10.014`.

[12] P. Holmberg, T. Berntsson, Alternative working fluids in heat transformers, Ashrae Transactions 96 (pt 1).

[13] M. O. McLinden, R. Radermacher, Others, Experimental comparison of ammonia-water and ammonia-water lithium bromide mixtures in an absorption heat pump.

[14] R. Radermacher, Y. Hwang, Vapor Compression Heat Pumps: With Refrigerant Mixtures, CRC Press, 2005.

[15] J.-S. Kim, Y. Park, H. Lee, Performance evaluation of absorption chiller using LiBr+ H2N (CH2) 2OH+ H2O, LiBr+ HO (CH2) 3OH+ H2O, and LiBr+ (HOCH2CH2) 2NH+ H2O as working fluids, Applied Thermal Engineering 19 (2) (1999) 217–225.

[16] A. De Lucas, M. Donate, J. F. Rodríguez, Vapour pressures, densities, and viscosities of the (water+ lithium bromide+ potassium acetate) system and (water+ lithium bromide+ sodium lactate) system, The Journal of Chemical Thermodynamics 38 (2) (2006) 123–129.

[17] D. L. Antonio, D. Marina, F. R. Juan, Vapor pressures, densities, and viscosities of the (H2O+ LiBr+ sodium formate) system and (H2O+ LiBr+ potassium formate) system, Journal of Chemical Engineering Data 48 (2003) 18–22.

[18] R. Saravanan, M. P. Maiya, Thermodynamic comparison of water-based working fluid combinations for a vapour absorption refrigeration system, Applied thermal engineering 18 (7) (1998) 553–568.

[19] J. Castro, Simulation of heat and mass transfer phenomena in the critical elements of H2O-LiBr absorption cooling machines. Experimental validation and application to design, Ph.D. thesis, Universitat Politecnica de Catalunya (2005).

[20] J. Farnós, Development of a prototype demonstration of a direct air-cooled LiBr H2O absorption cooling machine, Ph.D. thesis, Technical University of Catalonia - BarcelonaTech (2019).

[21] S. A. Kalogirou, Solar thermal collectors and applications, Progress in Energy and Combustion Science 30 (3) (2004) 231–295. `doi:10.1016/j.pecs.2004.02.001`.

[22] H. Kessentini, J. Castro, R. Capdevila, A. Oliva, Development of flat plate collector with plastic transparent insulation and low-cost overheating protection system, Applied Energy 133 (2014) 206–223. `doi:10.1016/j.apenergy.2014.07.093`.

[23] R. Febrer, J. Castro, J. Zheng, J. Rigola, A. Oliva, D. Kizildag, Mathematical Modeling and Experimental Validation of a Highly Efficient Flat Plate Solar Collector with compound Transparent Insulation Materials including a Silica Layer, Proceedings - ISES Solar World Congress 2021 (2021) 408–419`doi:10.18086/swc.2021.22.03`.

[24] J. Zheng, R. Febrer, J. Castro, J. Rigola, D. Kizildag, Experimental Testing of a Solar Thermal Collector with composite TIM of plastic Honeycomb and Silica Aerogel Polyurethane Containers, in: Proceedings - EuroSun 2022, 2022.

[25] D. Kizildag, J. Castro, H. Kessentini, E. Schillaci, J. Rigola, First test field performance of highly efficient flat plate solar collectors with transparent insulation and low-cost overheating protection, Solar Energy 236 (December 2021) (2022) 239–248. `doi:10.1016/j.solener.2022.02.007`.

[26] K. A. Joudi, A. H. Lafta, Simulation of a simple absorption refrigeration system, Energy Conversion and Management 42 (13) (2001) 1575–1605. `doi:10.1016/S0196-8904(00)00155-2`.

[27] G. A. Florides, S. A. Kalogirou, S. A. Tassou, L. C. Wrobel, Design and construction of a LiBr-water absorption machine, Energy Conversion and Management 44 (15) (2003) 2483–2508. `doi:10.1016/S0196-8904(03)00006-2`.

[28] G. Evola, N. Le Pierrès, F. Boudehenn, P. Papillon, Proposal and validation of a model for the dynamic simulation of a solar-assisted single-stage LiBr/water absorption chiller, International Journal of Refrigeration 36 (3) (2013) 1015–1028. `doi:10.1016/j.ijrefrig.2012.10.013`.

[29] J. Lopez, O. Lehmkuhl, R. Damle, J. Rigola, A parallel and object-oriented general purpose code for simulation of multiphysics and multiscale systems, in: Proceedings of the 24th International Conference on Parallel CFD, 2012.

[30] J. Castro, J. Farnós, G. Papakokkinos, J. Zheng, C. Oliet, Transient model for the development of an air-cooled LiBr-H2O absorption chiller based on heat and mass transfer empirical correlations, International Journal of Refrigeration 120 (2020) 406–419. `doi:10.1016/j.ijrefrig.2020.08.030`.

2

Thermophysical properties of the working pairs

Abstract

The knowledge of the thermophysical properties of working pairs in the absorption system are critical in the numerical simulation, and they are also indispensable in the design of the experiment. Though plentiful information on working pairs LiBr$-H_2O$ and Carrol$-H_2O$ are reported in recent decades, there are still limited experimental or modelling data for some properties. In this chapter, the properties of both working pairs LiBr-H_2O and Carrol-H_2O used in this dissertation that are barely reported before will be measured experimentally o numerically modelled. Firstly, activity coefficients and corresponding values of specific entropy and exergy are obtained with mathematical modelling. Entropy and exergy are critical parameters in the exergy analysis, and activity coefficients are necessary to calculate the chemical exergy of multicomponent solutions. Then, electrical conductivity is measured with experiments at various temperatures and concentrations. Electrical conductivity has a linear relationship between temperature and concentration of the solution, hence could be employed to measure the solution concentration in the circuit. Besides, surface tension and contact angle with liquid and gaseous surfactants are also measured under different conditions. It has to be remarked specially that the contact angle is critical in determining wettability and, by consequence, has a significant effect on the heat and mass transfer coefficients of falling films. Finally, nanofluid based on both working pairs are prepared with nanoparticles

CuO and Al_2O_3. The thermophysical properties of the working pairs with nanofluids are calculated with mathematical modelling. The electrical conductivity was reported in [1], the entropy and exergy were reported in [2], surface tension and contact angle were reported in [3] and [4], and properties of nanofluid were mentioned in [5].

2.1 Introduction

The exergy represents the maximum useful work possible during a physical or chemical procedure that brings the system into equilibrium, in some simplifications, reaching ambient temperature. In a thermal system, exergy also represents the quality of energy; therefore, exergy analysis could demonstrate more details than energetical analysis. Physical exergy is calculated with specific entropy, and specific entropy is generally calculated from other properties like specific heat and temperature. Meanwhile, the procedure to determine chemical exergy is more complicate, in which activity coefficients are necessary in the calculation. Activity coefficients of the binary and ternary systems are calculated in Section 2.2.1. The exergy and entropy is calculated in Section 2.2.2 and reported in previous work [2] with activity coefficients.

Electrical conductivity is a secondary thermophysical property of an electrolyte solution, which could be used to measure the density of the solution in a simple method (cost-compactness effective), is measured with experiments in Section 2.3 and reported in previous work [1].

Surface tension and contact angle are critical parameters that affect the heat and mass transfer coefficients of falling film absorption. Surface tension with and without surfactants for LiBr solution are reported in the literature, while there is limited information for Carrol solution according to the author's knowledge. Hence surface tension experimental measurements for both working pairs are reported in Section 2.4. Moreover, contact angle plays an important role in the wettability of the falling film type heat exchanger. The contact angle measurement is also reported in Section 2.4. Both experimental results were reported in previous work [4] and [3].

Finally, nanofluids are prepared with nanoparticles CuO and Al_2O_3 with dispersant E414 for both working pairs LiBr-H_2O and Carrol-H_2O. The thermophysical properties are calculated mathematically according to Xuan et al. [6]. The enhancement of thermal conductivity will affect the heat and mass transfer coefficients in the falling film. The results are showed in Section 2.5 and reported in previous work [5].

2.2 Thermodynamical and thermophysical properties of working pairs

In this section, activity coefficient, specific entropy, and specific exergy are modelled with different methods. The final results are shown as correlations for entropy, exergy for both working pairs LiBr-H_2O, Carrol-H_2O and activity coefficients for each component in the working pairs. Considering the working conditions of a typical absorption system ($T_{EVA,pri}$ = 7°C, $T_{ABS,pri}$ = 45°C) in [2], the partial pressure of EG in aqueous solution could be neglected (< 1Pa). Subsequently the activity coefficient of EG in the EG solution could also be neglected (<2.5E-5).

For LiBr-H_2O solution, thermophysical properties such as density, viscosity, enthalpy, specific heat, and VLE (Vapor-liquid equilirbium) are taken from [7] and [8]. For the Carrol solution case, these thermophysical properties are taken from [9]. The properties of H_2O in liquid and vapour phases are extracted from [10], and the properties of EG and its aqueous solution are extracted from [11]. Entropy is one of the important properties to determine the exergy, which is generally calculated from specific heat and temperature.

2.2.1 Activity coefficient for ternary solution system

Activity coefficient is a factor used in thermodynamics to account for deviations from ideal behaviour in a mixture of chemical substances. This factor is required to calculate the chemical exergy of a non-ideal mixture of electrolyte, organic compound, and H_2O.
a) The electrolyte activity coefficient
For strong electrolytes, the single ion activity coefficient model was extracted from Taghikhani et al. [12] as shown in Equation 2.1

$$\ln\gamma_{\text{ion}} = \frac{-A' z_{\text{ion}}^2 \sqrt{I_{\text{ion}}}}{1+\vartheta\sqrt{I_{\text{ion}}}} + B' \frac{I_{\text{ion}}^{3/2}}{1+\vartheta\sqrt{I_{\text{ion}}}} + C' \ln\left(1+\vartheta I_{\text{ion}}^{2/3}\right) \tag{2.1}$$

Where A' is the Debye-Hückel constant, which in mole fraction basis at 298.2K is equal to 8.766; and B', C' are two adjustable parameters, for Li^+ $B' = 244.05, C' = 1.39$, for Br^+ $B' = 120.94$, $C' = -0.82$, and ϑ is a dimensionless size parameter equal to 9. I_{ion} is the ionic strength, calculated as Equation 2.2

$$I_{\text{ion}} = \frac{1}{2} \sum_{\text{ion}} z_{\text{ion}}^2 \varphi_{\text{ion}} \tag{2.2}$$

where z_{ion} is the charge number of ion, φ_{ion} is the mole fraction of the corresponding ion. For LiBr, a single ionic type is chosen to calculate the mean activity coefficient of the salt according to the activity coefficient of its ions, as shown in Equation 2.3

$$\log\gamma_{\pm,\Xi\Pi} = \frac{\varpi_{\Xi}\log\gamma_{\text{M}} + \varpi_{\Pi}\log\gamma_{\Pi}}{\varpi_{\Xi\Pi}} \tag{2.3}$$

where $\gamma_{\pm,\Xi\Pi}$ is the mean activity coefficient of strong electrolyte $\Xi\Pi$, and ± represents the charge type of the component. ϖ_{Ξ} is the number of moles of cation produced by dissociation of a mole of the electrolyte, ϖ_{Π} is the number of moles of anion produced, and they satisfy Equation 2.4

$$\varpi_{\Xi\Pi} = \varpi_{\Xi} + \varpi_{\Pi} \tag{2.4}$$

b) The solvent activity coefficient

For the solvent, a LIQUAC method from [13], [14] is used to predict the activity coefficient of each component on the solvent side. The activity coefficient in the solvent will satisfy Equation 2.5

$$\ln\gamma_{\text{solv}}^{m} = \ln\gamma_{\text{solv}}^{m,\text{LR}} + \ln\gamma_{\text{solv}}^{m,\text{MR}} + \ln\gamma_{\text{solv}}^{m,\text{SR}} \tag{2.5}$$

where m represents the solvent species, the activity coefficient is defined on a mole fraction scale, and LR, MR, SR represent long-range, middle-range, and short-range term, respectively.

The long range term is calculated as shown in Equation 2.6

$$\ln\gamma_{\text{solv}}^{m,\text{LR}} = -\frac{2AM_{\text{solv}}d_{\text{mix}}}{b^{3}d_{\text{solv}}}\left[1 + b\sqrt{I_{\text{ion}}} - 1/b\sqrt{I_{\text{ion}}} - 2\ln\left(b\sqrt{I_{\text{ion}}}\right)\right] \tag{2.6}$$

where $I_{\text{ion}}$is the ionic strength of the ion, M_{solv} is the molar mass of the solvent in kg/mol, $d_{\text{solv}}$is the mole density of the regarded solvent in kg/mol, $d_{\text{mix}}$is the mole density of solvent calculated as Equation 2.7. The Debye-Hückel parameters A, b are shown as Equations 2.9,2.10, respectively.

$$d_{\text{mix}} = \sum_{\text{solv}} \varsigma'_{\text{solv}} d_{\text{solv}} \tag{2.7}$$

where $\varsigma'_{\text{solv}}$is the salt free volume fraction of the solvent as shown in Equation 2.8.

$$\varsigma'_{\text{solv}} = \frac{\varphi'_{\text{solv}}\varsigma_{\text{solv}}}{\sum_{\text{solv2}}\varphi'_{\text{solv2}}\varsigma_{\text{solv2}}} \tag{2.8}$$

where φ'_{solv} is the salt free molar fraction.

$$A = 13277.57\frac{\sqrt{d_{\text{mix}}}}{(D_{\text{mix}}T)^{3/2}} \tag{2.9}$$

where T is absolute temperature,

$$b = 6.359696\text{E}5\frac{\sqrt{d_{\text{mix}}}}{(D_{\text{mix}}T)^{1/2}} \tag{2.10}$$

where D_{mix} is the relative dielectric constant of the solvent mixture, calculated with Equation 2.11

$$D_{\text{mix}} = \sum_{\text{solv}} \varsigma'_{\text{solv}} D_{\text{solv}} \tag{2.11}$$

The middle range term for each group could be calculated as Equation 2.12. The EG could be divided into subgroups, $\left(\text{CH}_2^{[\text{OH}]}\right)_2$, and $(\text{OH})_2$, see Marcolli et al. [15].

$$\begin{aligned}
&\ln\left(\gamma^{m,\text{MR}}_{\text{group}}\right) = \\
&\quad \sum_{\text{ion}} \left[M_{\text{ion}} B_{\text{group,ion}}(I_{\text{ion}})\right] - \\
&\quad \frac{M_{\text{solv}} \sum_{\text{solv}} \sum_{\text{groups}} \varsigma^{\text{solv}}_{\text{groups}} \varphi'_{\text{solv}}}{M_{\text{mix}}} \\
&\quad \sum_{\text{groups}} \sum_{\text{ion}} \varphi'_{\text{groups}} M_{\text{ion}} \left(B_{\text{groups,ion}}(I_{\text{ion}}) + I_{\text{ion}} \frac{\partial B_{\text{groups,ion}}(I_{\text{ion}})}{\partial I_{\text{ion}}}\right) - \\
&\quad M_{\text{group}} \sum_{\Xi} \sum_{\Pi} \left[M_{\Xi} M_{\Pi} \left(B_{\Xi,\Pi}(I_{\text{ion}}) + I_{\text{ion}} \frac{\partial B_{\Xi,\Pi}(I_{\text{ion}})}{\partial I_{\text{ion}}}\right)\right]
\end{aligned} \tag{2.12}$$

In which, M_{mix} is molar mass of the mixture and could be obtained as Equation 2.13, M_{Ξ},M_{Π} are the cation and anion molar mass in $\text{kg} \cdot \text{mol}^{-1}$

$$M_{\text{mix}} = \sum_{\text{solv}} \left[\varphi'_{\text{solv}} M_{\text{solv}}\right] \tag{2.13}$$

$B_{i,j}(I_m)$)is an interaction parameter could be calculated as Equation 2.14, and its derivative as shown in Equation 2.15

$$B_{i,j}(I_{\text{m}}) = b'_{i,j} + c'_{i,j}\exp\left(a_1\sqrt{I_{\text{m}}} + a_2 I_{\text{m}}\right) \tag{2.14}$$

Table 2.1: Relative van der Waals surface area Q_k and volume R_k of different groups

	R_k	Q_k
CH_2	6.744	0.54
OH	1	1.2
H_2O	0.92	1.4
Li^+	0.1292	0.2556
Br^-	1.0688	1.0453

$$\frac{\partial B_{i,j}(I_\mathrm{m})}{\partial I_m} = \left(\frac{a_1}{2 \cdot \sqrt{I_\mathrm{m}}} + a_2\right) \cdot c_{i,j} \cdot \exp\left(a_1 \sqrt{I_\mathrm{m}} + a_2 I_\mathrm{m}\right) \tag{2.15}$$

where a_1,a_2 are middle range parameters in the LIQUAC method, and a_1(solv-ion) is -1. a_1(ion-ion) is -1, a_2(solv-ion) is 0.13, a_2(ion-ion) is 0.13. Also, $b_{i,j}, c_{i,j}$ are fitted parameters for different combinations of structural groups and ions, which are given in Table 2.2, extracted from Hansen et al. [16].

Finally, the middle term for solvent specie could be calculated according to groups as Equation 2.16:

$$\ln \gamma_\mathrm{solv}^{m,\mathrm{MR}} = \sum_\mathrm{groups} \left[\varsigma_\mathrm{groups}^\mathrm{solv} \ln\left(\gamma_\mathrm{solv}^{m,\mathrm{SR}}\right)\right] \tag{2.16}$$

Short range term could be calculated as Equation 2.17

$$\ln\left(\gamma_i^\mathrm{SR}\right) = \ln\left(\gamma_i^\mathrm{C}\right) + \ln\left(\gamma_i^\mathrm{R}\right) \tag{2.17}$$

The short terms consists of a combinatorial (C) and a residual (R) part, and the combinatorial term is calculated by Equation 2.18,

$$\ln\left(\gamma_i^\mathrm{C}\right) = 1 - V_i + \ln V_i - 5q_i \left[1 - \frac{V_i}{F_i} + \ln\left(\frac{V_i}{F_i}\right)\right] \tag{2.18}$$

Where , V_i and F_i are the are fractions divided by the mole fraction and are calculated as Equations 2.19,2.20:

$$V_i = \frac{r_i}{\sum_j \varphi_j r_j} \tag{2.19}$$

$$F_i = \frac{q_i}{\sum_j \varphi_j q_j} \tag{2.20}$$

where r_i is the van der Waals volume of the regarded component, q_i is the van der Waals surface area of the regarded component as shown in Table 2.1, see [16], φ_j is the

Table 2.2: Parameters system

i	j	a	b	c
$CH_n(OH)$	$CH_n(OH)$	0	0	0
$CH_n(OH)$	OH	986.5	986.5	2.1976
OH	OH	0	0	0
OH	$CH_n(OH)$	156.4	200	-0.8
$CH_n(OH)$	H_2O	2314	-2151	-1.6464
OH	H_2O	-189.7	0	0
H_2O	H_2O	0	0	0
H_2O	$CH_n(OH)$	-89.71	-200	-0.8
H_2O	OH	-153	100.86	-0.8
$CH_n(OH)$	Li^+	0.07505	-0.05934	
OH	Li^+	0.23521	-0.09633	
H_2O	Li^+	0.00319	-0.00099	
$CH_n(OH)$	Br^-	-0.10426	0.29235	
OH	Br^-	0.10294	-0.34848	
H_2O	Br^-	-0.00247	-0.00008	
Li^+	Br^-	0.40455	-0.26148	

mole fraction of the regarded compound. The residual part of the short-range term is calculated as Equation 2.21,

$$\ln\left(\gamma_i^{\mathrm{R}}\right) = q_i \left[1 - \ln\left(\sum_j \{\Theta_i \Psi_{i,j}\}\right) - \sum_j \frac{\Theta_j \Psi_{i,j}}{\sum_k \{\Theta_j \Psi_{i,j}\}}\right] \tag{2.21}$$

$\Theta_j, \Psi_{i,j}$, are the surface area fraction and adjustable temperature-independent parameter, calculated as Equations 2.22,2.23.

$$\Theta_j = \frac{\Psi_i q_i}{\sum_j \Psi_j q_j} \tag{2.22}$$

$$\Psi_{i,j} = \exp\left(-\frac{a'_{i,j}}{T}\right) \tag{2.23}$$

where $a'_{i,j}$ is short range fitting parameter, shown in Table 2.2, see [16]. This term was neglected intentionly in order to reduce the parameters.

c) Final results of activity coefficients

For the convenience of calculation and saving computation cost, the activity coefficient for LiBr solution and Carrol solution are computed and correlated as Equation 2.24.

Table 2.3: Correlation coefficients a_i for activity coefficients of LiBr solution

m	0	1	2	3
LiBr	-243.99	1366.76	-2551.7	1587.95
H_2O	5.57	-38.838	90.72	-81.509

Table 2.4: Correlation coefficients A_i for activity coefficients of LiBr solution

m	0	1	2	3
LiBr	0.509547	0.0497875	0.138108	4.13E-4
EG	-3.3185E-3	0.01571	-0.00244	0.012415
H_2O	-3.06125	127.064	-320.6699	209.154

$$\gamma_{\mathrm{m}} = \varphi_m \left(\sum a_i \iota_m^i \right) \tag{2.24}$$

where ι represents molality, a_i represents the correlated coefficent, m represents the component. The parameters of the LiBr-H_2O and Carrol-H_2O are shown in Table 2.3,2.4, repectively. The validity concentration range is 40%-65% and the validity temperature range is $30-50$°C for LiBr-H_2O and for the Carrol-H_2O, the concentration range is 50%-75% and the temperature range is $30-50$°C.

2.2.2 Specific entropy and exergy

Entropy and exergy calculation are well reported in the literature for the H_2O, EG, and LiBr aqueous solutions. Meanwhile, for the Carrol and EG aqueous solution, this information is limited.

a). Entropy

A simple method is used to calculate the entropy of the LiBr-H_2O solution by employing Equations 2.25, and 2.26. Since the entropy of 50wt%, and 0°C is set as 0 J·kg^{-1}·K^{-1}, the entropy at other temperature could be obtained, as mentioned in Kaita [8]. The result is compared with the result reported in Kaita [8] with an error of less than 0.5%. Thus, the same method is used to calculate the entropy of the Carrol and EG solutions. The final results of entropy are fitted as Equation 2.27, which shows the correlation to calculate the entropy. The subscripts i, j represent the exponential index for the temperature and concentration, respectively. The corresponding parameter B_{ij} is shown for each case (LiBr-H_2O, Carrol-H_2O and EG-H_2O) in the Tables 2.5,2.6, and 2.7, respectively.

Table 2.5: Entropy fitted parameter of LiBr-H_2O solution

$B_{i,j}$		j			
		0	1	2	3
i	0	5.13E-1	-1.39E-2	2.92E-5	9.04E-7
	1	1.23E-2	-9.16E-5	1.82E-8	-7.99E-10
	2	-1.36E-5	1.07E-7	-1.38E-9	1.53E-11
	3	1.02E-8	0	0	0

Table 2.6: Entropy fitted parameter of Carrol-H_2O solution

$B_{i,j}$		j			
		0	1	2	3
i	0	5.445E-3	1.4998E-2	-2.2E-5	1.82E-8
	1	-7.4E-5	-1.2E-4	1.45E-7	0
	2	2.3E-12	-3.76E-14	0	0
	3	3.24E-15	0	0	0

$$\frac{\partial s}{\partial T} = \frac{1}{T}\frac{\partial h}{\partial T} = \frac{C_\mathrm{p}}{T} \tag{2.25}$$

$$s(T,50) = \int_0^T \frac{C_\mathrm{p}}{T+273.15}\mathrm{d}T \tag{2.26}$$

$$s = \sum_i \sum_j B_{ij} T^i C^j \tag{2.27}$$

b). Exergy

Exergy is the critical point of thermodynamic second law analysis of the system, calculated as the sum of physical and chemical exergy. Physical exergy is equal to the

Table 2.7: Entropy fitted parameter of EG-H_2O solution

$B_{i,j}$		j		
		0	1	2
	0	0.452	1.52E-2	3.22E-5
i	1	0	-3.99E-3	-2.41E-4
	2	0	0	0

maximum amount of work obtainable when the stream of substance is brought from its present state to the environmental state (defined by P_0 and T_0) by physical processes involving only thermal interaction with the environment, see Kotas et al. [17]. The exergy of a fluid stream could be expressed as in Equation 2.28 neglecting kinetic and potential components of the exergy:

$$e_{\mathrm{phy}} = (h - h_0) - T_0(s - s_0) \tag{2.28}$$

where e,h,s are the specific exergy, enthalpy, and entropy, respectively, at the corresponding situation, and T_0, s_0, h_0 denote the temperature, entropy, and enthalpy at the reference point, respectively. Ambient temperature is set as the reference, depending on the ambient temperature of the thermal system.

On the other hand, chemical exergy is the maximum work that can be achieved when a substance is driven from its equilibrium state at a given concentration, and at the environmental pressure and temperature, to another equilibrium state where the chemical potentials are equal (unrestricted dead state), through a process in which heat, work and mass transfers with the environment, are involved, see Palacios-Bereche et al. [18]. The chemical exergy contains two parts, standard chemical exergy of pure species $\mathrm{e}_{\mathrm{ch\_std}}$ and exergy destruction due to dissolution process $\mathrm{e}_{\mathrm{ch\_dis}}$. The chemical exergy could be expressed as Equations 2.29,2.30,2.31:

$$e_{\mathrm{ch}} = e_{\mathrm{ch\_std}} + e_{\mathrm{ch\_dis}} \tag{2.29}$$

$$e_{\mathrm{ch\_std}} = (1/M_{\mathrm{sol}})\sum_{\mathrm{m}}[\varphi_{\mathrm{m}}\varepsilon_{\mathrm{m}}] \tag{2.30}$$

$$e_{\mathrm{ch\_dis}} = (1/M_{\mathrm{sol}})\sum_{\mathrm{m}}[\mathrm{R}T\varphi_{\mathrm{m}}\ln(a_{\mathrm{m}})] \tag{2.31}$$

where M_{sol} is the molar mass of solution, m is the component in the mix solution, φ_{m} is the molar fraction, ε_{m} is the standard chemical exergy, a_{m} is the activity of the m, and R is the ideal gas constant.

c). Activity of each component in the solution

Activity could be calculate as Equation 2.32

$$a_{\mathrm{m}} = \gamma_{\mathrm{m}}\varphi_{\mathrm{m}} \tag{2.32}$$

where γ_{m} is the activity coefficient of m, and φ_{m} is the mole fraction of m. The UNIQUAC method is used to calculate the activity coefficient of the EG-H_2O solution, while the

LIQUAC method is used to calculate the activity coefficient of the ternary solution. For more details about its calculation process, see Section 2.2.1. In a 30wt% EG solution, the activity of EG is around 0.15. Considering the low temperature in the evaporator and EG's low saturation vapour pressure, the partial pressure of EG vapour in the evaporator could be neglected (< 1Pa).

2.3 Electrical conductivity of concentrated LiBr EG and H_2O ternary system

LiBr is currently a widely used absorbent in the absorption chiller, and the measurement of the concentration of the working pairs in the chiller is often required. Several methods could be employed, like Coriolis flow-meters, or titration method(not applicable to a continuous process) and a Coriolis flow meter is generally expensive and costly in maintenance and space. Hence the electrical conductivity, as it is a function of temperature and LiBr concentration, could be used as a secondary property to measure the LiBr concentration indirectly. Labra et al. [19] did research about the determination of the concentration for a prototype absorption machine. Electrical conductivity was selected from other properties such as refractive index, density, and sound velocity as method of measurement of properties of working fluids used in the prototypes of absorption due to their low cost, easy installation, and small volume needed for the measurement. In the case of direct air-cooled cycles, the use of LiBr as absorbent is limited due to problems of crystallization as reported in Castro et al. [20]. Carrol contains EG and LiBr with a mass ratio of 4.5:1 and has advantages concerning crystallization due to higher solubility in Best et al. [21]. Moreover, the LiBr charge is reduced.

The electrical conductivity (EC), whose unit is mS/cm, or electrical resistivity in mmho/cm, is the ability of a substance for conducting an electrical current. If the temperature of the substance increases, the EC will increase due to the ionization of molecules, which will increase the ion density in the volume according to Semat et al. [22]. But due to the ionization process, the ion density and mobility is not always reflecting the direct proportion relationship. Though electrical conductivity could be a critical parameter to determine the concentration of the solution in an alternative way in a continuous process, only a few pieces of literature described the experimental data and theory. And about the Carrol aqueous solution, according to the author's knowledge, there is no literature about it. In terms of the accuracy, compared with the relative error of Coriolis sensor at ±0.1%, the electrical conductivity sensor has a higher error at ±0.5% which projects an error around 0.4% in concentration. Considering the concentration of absorbent is around 50-60%, the error of electrical conductivity sensor is less accurate than Coriolis densimeter but is acceptable for some applications, such as crystalization control. Besides, for the absorption system studied in this dissertation, the solution is driven by gravity and the pressure difference to travel from generator to solution heat exchanger and reaches absorber. The installation of the electrical conductivity sensor will barely affect the pressure drop and compactiveness of the system.

Frled et al. [23] shows the electrical resistivity of concentrated LiBr aqueous solutions at LiBr mass ratio 40−63%, at temperature range 15−80°C, with an absolute accuracy of analytical determination is ±0.7% at concentration 40−50%. DeDiego et al. [24] did experiments that included LiBr and fitted the experimental results to the Falkenhagen equation [25] at 25°C. Sun et al. [26] measured electrical resistivity of LiBr aqueous solution at a temperature range of 10−100°C and a concentrations range of 35−70wt%. The measurements were reproducible with an accuracy of one mmho, and were correlated with a polynomial. Osta-Omar et al. [27] measured the electrical conductivity of LiBr/H_2O solution from 25−95°C at a concentration range 45−65%. The maximum error with experiment data and the fitted equation is 5.8%. In this section, electrical conductivity was measured at the range of 35−80°C for temperature and 45−65wt% for concentration.

2.3.1 Experiment Set up for electrical conductivity

During the experiment of electrical conductivity measurement, the solution sample should be adequately prepared to decrease the uncertainty, as temperature, concentration should be uniform in the sample. As shown in Figure 2.1, sensor 5 is an electrode to measure electrical conductivity with accuracy at 0.5%, having a temperature sensor integrated. Also, to avoid the stratification of different organic/inorganic groups and ions, a stirring machine (3) is used to stir the solution, and (4) is a magnetic stick used for stirring the solution sample. Element 6 are PT100 temperature sensors with error ±0.03°C to measure the temperature of different points in solution, and element 7 are thermal couples to control the surrounding temperature, element 8 are thermal blankets to heat the whole system. Element 2 is a data acquisition machine, and 9 is the control computer. The LiBr and EG used had a purity > 99%. The solution was prepared with a balance with an accuracy of 0.01g. The solution density was measured with a densimeter. For each case, the solution sample will be sealed with a rubber tap to avoid potential evaporation and absorption in the heating or cooling process. The experiment result is reproducible within 1.0 mS/cm. The relative error of the mass fraction of the

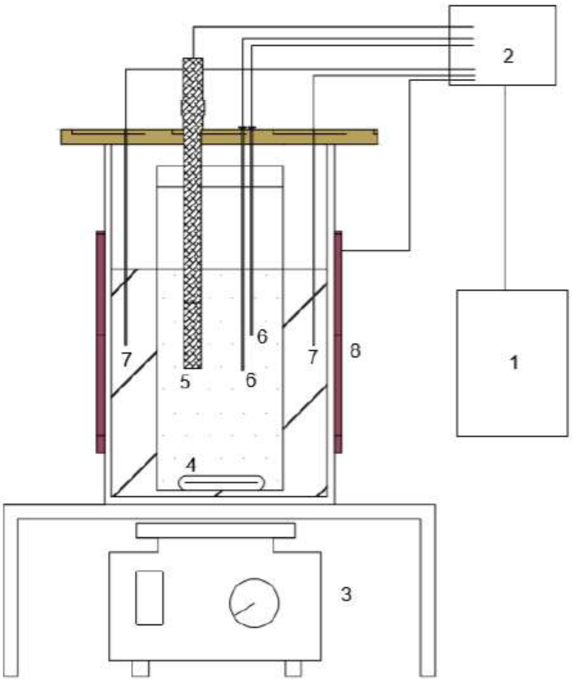

Figure 2.1: Experiment scheme of conductivity measurement. 1 is PC, 2 is DAC system, 3 is a magnetic stir machine, 4 is the magnetic stick, 5 is the electrical conductivity sensor, 6,7 are PT100, and 8 is electrical thermal blanket

solution is ±0.4%, and for the electrical conductivity of Carrol, LiBr aqueous solution is ±0.3%, ±0.4%, respectively. Compared to the relative error of a Coriolis sensor at ±0.1%, the electrical conductivity sensor has an acceptable level of accuracy for certain applications, such as crystalization control or determining concentration differences during high concentration changes.

2.3.2 Experiment results and analysis

For each measurement, the data must last about a minute for its recording to avoid latencies of the sensor. As shown in Figure 2.2, the electrical conductivity will increase along with the temperature at the same absorbent concentration and decrease with absorbent concentration at the same temperature. One of the aspects that favour the use

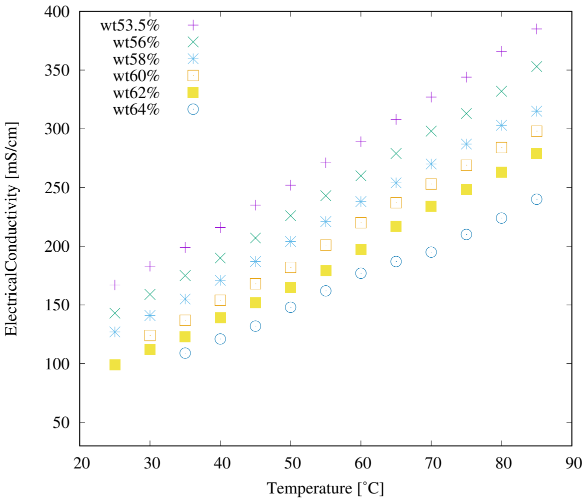

Figure 2.2: Electrical conductivity of LiBr aqueous solution at various concentrations

Table 2.8: Deviation ϱ en % between different authors and this work at 35°C

EC(mS/cm) at 35°C	54%		56%		58%		60%		62%	
	EC	ϱ	EC	ϱ	EC	ϱ	EC	ϱ	EC	ϱ
This work	199	-	175	-	155	-	137	-	123	-
Frled [23]	187	6.2	169	3.2	154	0.8	135	1.6	118	3.7
Sun [26]	188	5.7	169	3.4	153	1.6	135	1.3	117	4.5
Labra [19]	203	2.2	188	7.9	165	6.4	142	3.7	128	4.1

of electrical conductivity to measure the absorbent concentration is the high linearity when the concentration or the temperature changes. In Figure 2.3, the results are compared with experimental data from [23], [26], [19], at three temperatures, 35, 50, 70 °C, for better visualization. The maximum of the average absolute deviation of the electrical conductivity is shown in Table 2.8. The discrepancy from different authors could be caused by various factors, such as the purity of the material, the accuracy of the balance, the relative error of the electrode and the preparation procedure, etc.

Figure 2.4 show the experimental results of the electrical conductivity of Carrol solution at various concentration and temperatures. From these, it is observed that the electrical conductivity of the Carrol solution is lower than the LiBr solution at the same

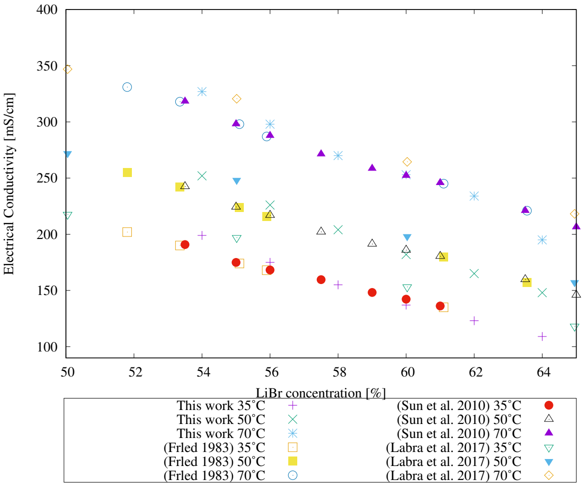

Figure 2.3: Experiment results compared with other authors [23], [26], [19] at selected concentrations

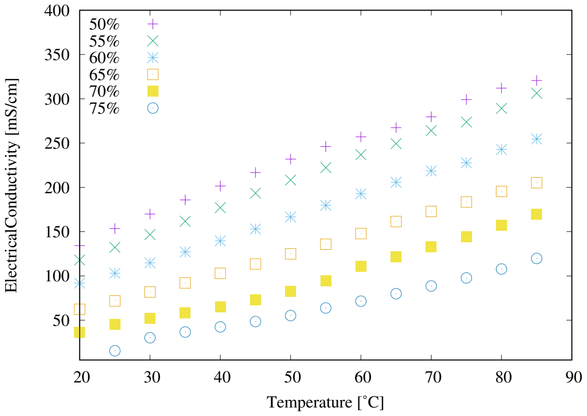

Figure 2.4: Electrical conductivity of Carrol aqueous solution at various concentrations

Table 2.9: Correlation coefficients for the experimental data

	A_0	A_1	A_2	A_3	B_1
Carrol solution	6.97E1	4.96E-1	-6.66E-3	7.49E-5	-0.25783
LiBr solution	6.97E1	2.93E-1	-2.61E-3	-2.05E-4	-0.18627
	B_2	B_3	C_1	C_2	C_3
Carrol solution	3.06E-4	-2.85E-6	2.42E-3	1.71E-5	-5.58E-5
LiBr solution	-1.52E-5	4.48E-6	2.21E-3	-4.93E-5	1.69E-4

Final sum of squares of residuals is 2.838 and 0.296 for Carrol and LiBr solution, respectively

ratio of electrolyte due to the presence of organic component. The linear relationship remains the same for the Carrol solution.

2.3.3 Summary of electrical conductivity

The experimental result of LiBr aqueous solutions shows a max discrepancy of 6.2% when compared with other authors. The high linearity shows the possible replacement of the EC electrode to the mass flowmeter. As shown in Table 2.9, the equation shows the relationship between temperature, EC, and concentration. The average error between the empirical equation and the experimental result is 0.25% and 0.3% in Carrol and LiBr aqueous solution. For temperature range 30−80 °C, concentration 40%−70%, the electrical conductivity is in the range of 100−400 mS/cm for both solutions. For the LiBr and Carrol aqueous solution, an empirical relation with temperature, electrical conductivity, and concentration is shown as Equation 2.33.

$$\begin{aligned} C =& A_0 + A_1 * T + A_2 * T^2 + A_3 * T^3 + B_1 * EC + B_2 * EC^2 + B_3 * EC^3 + \\ & C_1 * EC * T + C_2 * EC^2 * T + C_3 * EC * T^2 \end{aligned} \tag{2.33}$$

C is the concentration of solute %, EC is the electrical conductivity of mS/cm, T is the temperature of the solution of °C.

2.4 Surface tension and contact angle of LiBr-H_2O and Carrol-H_2O

Surface tension is the tendency of liquid surfaces at rest to shrink into the minimum surface area possible. Adding surfactants to the liquid could reduce the surface tension and produce the Marangoni effect due to the salting out phenomena, which enhances the heat and mass transfer at the fluid interface. Many authors did measurements of the surface tension of the LiBr solution with different concentrations of additives. The surface tension of LiBr and LiCl solutions with additives 1−octanol and 2−EH was measured in Yao et al. [28], employing a drop-volume method. The results show the surface tension varies with different LiBr concentrations and temperatures, and the 2−EH(2−Ethylhexanol) could reduce the surface tension to 35.24 $mN \cdot m^{-1}$ while 1-octanol could reduce it to 25.17$mN \cdot m^{-1}$ at 25°C. The surface tension of 60wt% LiBr solution with 2−EH was reported in Kim et al. [29] with the Du Noüy ring method and the results showed the surface tension changed from 81.3 to 34.9 $mN{\cdot}m^{-1}$ with 2−EH concentration at 0 − 200ppm. Besides 2−EH and 1−octanol, CTAC/CTAB (cetyltrimethyl ammonium chloride/cetyltrimethyl ammonium bromide) were also used as additives to reduce the surface tension by Cai et al. [30] since 1−octanol is easy to decompose at high temperature. Apart from adding liquid additives, gaseous surfactants could also play an important role in reducing the surface tension according to Yuan and Herold [31]. In which a drop volume method was employed to measure the surface tension change for H_2O and 60wt% LiBr solution with the presence of 2−EH dissolved in the air, and the results showed that the surfactants were more efficient in the vapour phase than in the liquid phase. In the case of the working pair Carrol−H_2O (proposed by [9] to reduce the crystallization risk), phenylmethylcarbinol (PMC, 1−Phenylethanol) was used as a surfactant, as suggested by Klein et al. [32].

Besides the surface tension of the solution, the contact angle also plays a relevant role in the heat and mass transfer performance, as it is a dominant parameter for the wettablity of the solid surfaces. The contact angle depends not only on the liquid properties but also on the solid base surface characteristics. Therefore the contact angle measurement is essential for the design of a falling film-type heat exchanger. The contact angle of LiBr solution on different surfaces was measured by Martinez-Urrutia et al. [33, 34] using a goniometer with the sessile drop method. The results showed that the surface tension and contact angle have a linear relationship with all the materials. As alternative to goniometer, a simple optical method was proposed by Lamour et al. [35] to determine the contact angle with an acceptable error without expensive equipment.

In this section, experimental results of the surface tension of the working pairs LiBr-H_2O and Carrol-H_2O with and without additives and their contact angles with different materials are presented. The Du Noüy ring method was used to measure the surface tension of working pairs LiBr/H_2O and Carrol/H_2O with surfactant concentrations 20−2000 ppm in the liquid phase, and the surfactants were 2−EH, 1−Phenylethanol, respectively. Besides, the contact angle of both working pairs was measured with the simplified optical method at stainless steel and PVC plates.

2.4.1 Experimental Set-ups

a). Surface tension

The surface tension measurement procedure used was employed in two previous works [3, 4], with the Du Noüy ring method, in that case only adding liquid additives to the solution. The sample container is covered with heaters with a controller to maintain a corresponding temperature when this variable is considered. Several thermocouples are placed in the liquid to ensure a uniform temperature distribution in the liquid sample. In order to estimate possible errors and uncertainties, it was taken into account that the tensiometer has a resolution of 0.1 $\mathrm{mN{\cdot}m^{-1}}$, the chemicals used here have a purity of at least 99%, and the sample is prepared with a balance with a resolution of 10 mg. However, more factors should be considered when there is an additive in the vapour phase to acquire high precision results. The surface tension measurement set−up is shown in Figure 2.5. From left to right, compressed air enters the set−up, controlled by a rotameter. In the tube, airflow will mix with the additive vapour flow from the flask, and the mixture will finally enter the test chamber. The flask is filled with the corresponding additive and heated by a heating mantle.

b). Contact angle

The measurement set-up is shown in Figure 2.6, and consists of a camera, lens, moving stage, micropipette and light source, etc. For the solid base for the contact angle measurement, stainless steel and PVC plates were used from untreated raw material with a dimension of 3cm*3cm. Then a 3μL droplet is introduced on the dry plate, and the image is finally taken through the montage. The contact angle is calculated by the software *ImageJ*.

2.4.2 Sample preparation and measurement process

a). Surface tension

When the surface tension is measured with only a liquid sample, their preparation to assure repeatability is not complex. However, additional procedures are considered when there is a surfactant in the vapour phase: the air velocity is controlled to a maximum value of 0.05 $\mathrm{m{\cdot}s^{-1}}$, to avoid its effect on the measurement, as mentioned in [31]. A rotameter controls the volumetric flow, being the velocity calculated according

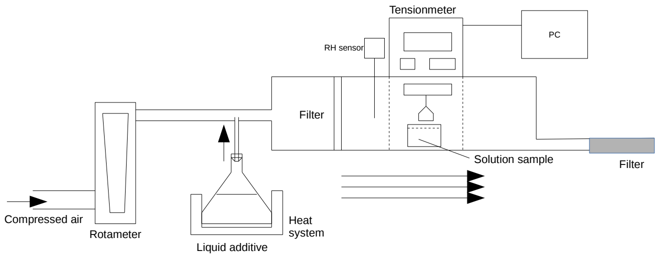

(a) Sketch of the test rig of surface tension

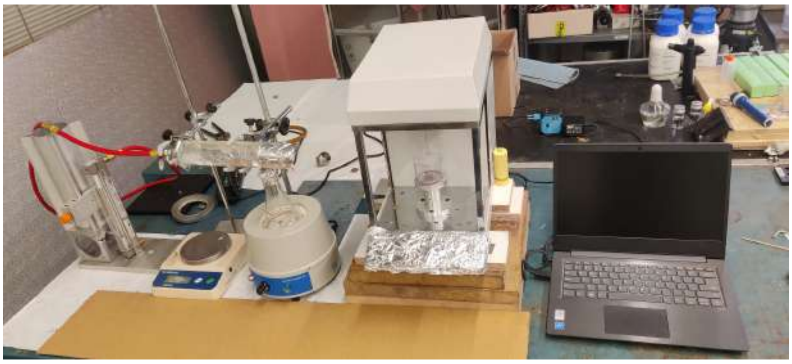

(b) Foto of the test rig of surface tension

Figure 2.5: Experimental set-up for the measurement of surface tension

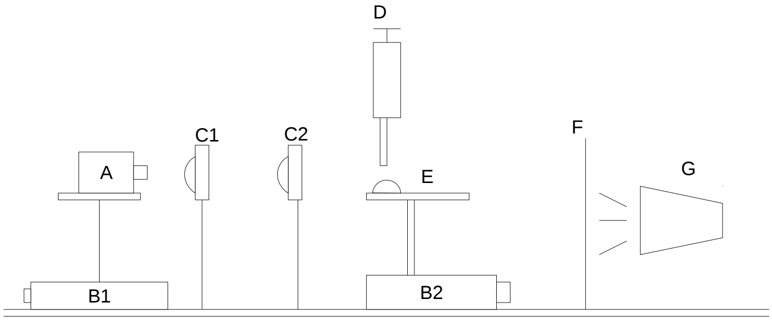

(a) Sketch of the test rig of contac angle

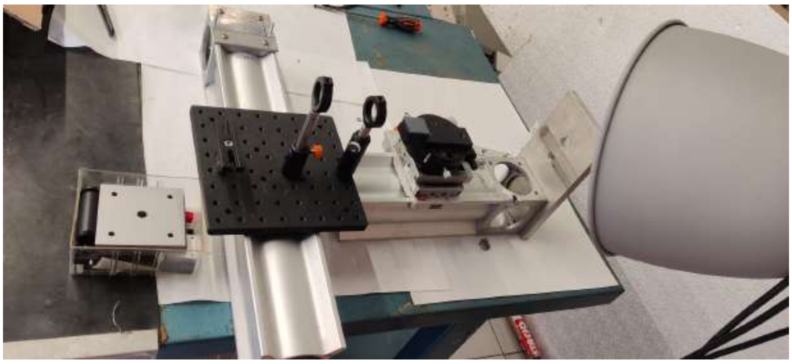

(b) Foto of the test rig of contact angle

Figure 2.6: Experimental set-up for the measurement of contact angle: A is the camera, B1, B2 are moving stage, C1, C2 are lens, D is micropipette, E is drop sample, F is the diffuser, and G is the light source

to the test chamber geometry. When the flask starts boiling stably, the additive is supposed to be mixed well with air in the length of 30 cm. Then, the airflow enters the measurement chamber, where a Du Noüy ring method is used to measure the surface tension. Before and after the test chamber, there is a filter to avoid contamination from the ambient. In the test chamber, the additive may condense on the liquid surface of the test sample. To specify the reason causing the surface tension decrease, multiple measurements should be carried out before, during, and after the mixture flow.

The evaporation rate is calibrated considering the mass change vs. time. Before each test, the same amount of additive mass in the flask is fixed, and after the boiling begins, the remaining additive mass is measured every 2 minutes until a stable mass reduction rate is acquired. When the evaporation rate is considered stable in the test, i. e. after 5 minutes of boiling, the air and additive mixture distribution is considered adequate. The effect of mass change in the flask on the evaporation rate is neglected since the difference is less than 1%. The measurement of a solution sample is repeated up to six times to determine the uncertainty. The uncertainty of this measurement is calculated as shown in Appendix A.1. The uncertainty $\varepsilon_{\text{final}}$ is 1.5% of the pure liquid sample and 2.3% of surfactants in the vapour phase. The error due to the chemical products and preparation process represents around 30% of the total error. The other 70% came from the tensiometer and the repeatability of the process.

Before the test, the sample should be prepared and kept in a closed vessel. Moreover, to acquire a stable evaporating rate, manual calibration should be done with the flask and heating mantle until reaching a repeatable evaporation rate before the test. For example, 200 ppm of additive mixture means an evaporation rate of 0.1 g per 20 minutes with a 20 LPM airflow. To perform a test, set a volumetric airflow with the rotameter, start the heating mantle, place the sample in the chamber when the boiling begins, and make the measurement every minute. Before performing a new test, all the related apparatus must be well cleaned with alcohol to eliminate the condensation of the surfactant. A correction of the surface tension measurement is automated with ASTMD-971 method [36], as shown in Equation 2.34 and 2.35:

$$\sigma = \sigma_{\text{mea}} * \chi \tag{2.34}$$

$$\chi = \sqrt{0.7250 + 0.01452 * P/o^2/(\rho_{\text{l}} - \rho_{\text{air}}) + 0.04534 - 1.679 * r'/R'} \tag{2.35}$$

where $\sigma, \sigma_m athrmmea, and \chi$ are the real surface tension, measured surface tension, and correction parameter, respectively. o is the perimeter of the platinum ring in cm, R' is the diameter of the ring in cm, ρ_{l} and ρ_{air} are the density at 25°C of liquid and air, respectively, in g/mL. And r' is the thickness of the wire of the ring, also in cm.

b). Contact angle

The solution sample was prepared using a balance with resolution at 10mg using LiBr, EG, and distilled H_2O with a purity of 99%, 99.5%, and 99%, respectively. Then the micropipette used caused an error of 1% (reading error) in transporting the surfactant into the solution sample. The liquid samples should be prepared carefully without contamination and kept sealed before the measurement. For the Carrol solution, the stratification will significantly affect the final result, so the Carrol solution should be well mixed before the contact angle measurement. In order to measure the contact

Table 2.10: Surface tension of H_2O and EG compared with reference data, and the reference values of H_2O are taken from Vargaftik et al. [37], the reference values of EG are taken from Azizian et al. [38]

Temperature [°C]		σ [mN·m^{-1}]		Reference value [mN·m^{-1}]		Discrepancy [%]	
Water	EG	Water	EG	Water	EG	Water	EG
21.2	25	72.9	47.1	72.4	47.6	0.5	1.1
30	30	70.3	46.4	71.2	48.1	1.3	3.5
40	40	68.1	45.8	69.6	47.1	0.7	2.8
50	50	66.1	45.0	67.9	45.9	2.7	2.0
60	60	63.7	44.1	66.2	–	3.8	–

angle, a 3μL droplet is introduced on the dry clean plate with micropipette.

2.4.3 Experimental results of surface tension without additives

The surface tension of an aqueous solution is affected by many factors, such as the purity of the substance, the measurement method, the relative humidity, etc. Hence, the data from different authors won't fully agree between them. In this section, the surface tension of pure liquid of distilled H_2O and EG is measured to validate the precision of measurement. And when those two working pairs are compared, due to the presence of organic compound EG, the Carrol solution has lower surface tension than the LiBr solution. The surface tension of H_2O, EG, LiBr solution is measured at the specific condition and compared with results from references as shown in Table 2.10 and 2.11. There is good agreement between the results with other authors.

Besides, the results of LiBr−H_2O and Carrol−H_2O is shown as Figure 2.7 and 2.8. The experimental data of the LiBr solution is compared with data in Wang et al. [41]. The surface tension data is fitted with a nonlinear least-squares method as Equation 2.36 with an average relative error of 1.47%, and the maximum relative error is 2.68%. The subscripts i,j represent the exponential index for the temperature and concentration, respectively. The corresponding parameter B_{ij} is shown for LiBr−H_2O and Carrol−H_2O in the Table 2.12 and 2.13, respectively.

$$\sigma = \sum_i \sum_j B''_{ij} C^i T^j \tag{2.36}$$

Table 2.11: Surface tension results of LiBr and Carrol solution at different concentrations and compare them with other references

Liquid type	Experimental results		Reference value	
	T[°C]	σ[mN·m]	T[°C]	σ[mN·m^{-1}]
Distilled H_2O	21.2	72.9	20	72.4 [39]
EG	21.2	47.3	20	47.3 [40]
50%LiBr	21.2	82.9±0.2	20	88.1±0.15 [28]
			24	77.6±0.4 [29]
55%LiBr	22.5	86.2±0.3	28	86.42 [30]
60%LiBr	21.2	91.3±0.6	25±0.2	94.3±0.5 [31]
			20	94.4±0.1 [28]
55%Carrol	21.3	72.5±0.2	-	-
60%Carrol	21.3	74.7±0.3	-	-

Table 2.12: Surface tension fitted parameter of LiBr−H_2O

$B''_{i,j}$		j			
		0	1	2	3
i	0	71.69	3.04	-0.00631	3.06×10^{-4}
	1	0	-0.108	6.06×10^{-4}	0
	2	0	0.00142	0	0
	3	0	0	0	0

Final sum of squares of residuals is 0.116

Table 2.13: Surface tension fitted parameter of Carrol−H_2O

$B''_{i,j}$		j			
		0	1	2	3
i	0	88.19	-5.11	0.028	-1.23×10^{-4}
	1	0	0.121	1.84×10^{-4}	0
	2	0	-8.56×10^{-4}	0	0
	3	0	0	0	0

Final sum of squares of residuals is 0.187

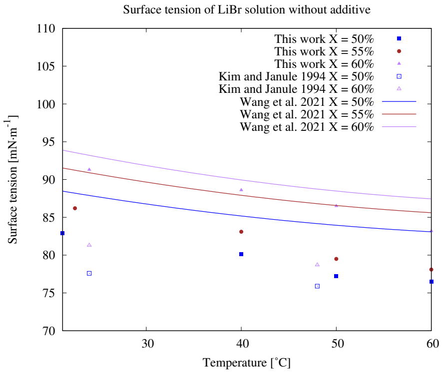

Figure 2.7: Experimental results of surface tension of LiBr$-$H$_2$O without additive against temperature and concentration compared with experimental data from [29], and empirical correlation from [41]

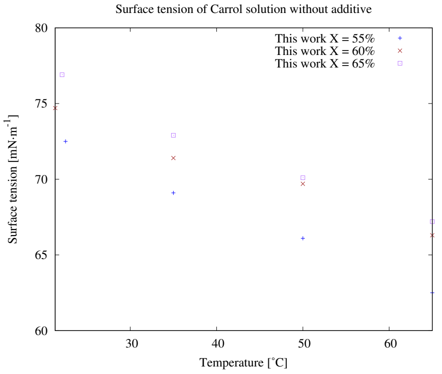

Figure 2.8: Experimental results of surface tension of Carrol$-$H$_2$O without additive against temperature and concentration

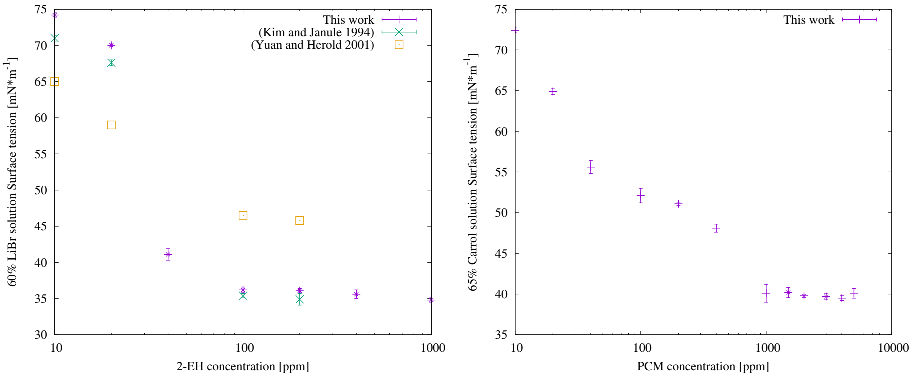

Figure 2.9: Surface tension results of two working pairs with a surfactant, and measurements were made under 22.5±1°C, 35±1RH%. The left figure represents the surface tension change of 60wt% LiBr solution with 2−EH, compared with [29], [31], and the right one represents the Carrol solution at 60wt% with PMC.

2.4.4 Experimental results of surface tension with liquid additives

One of the most commonly used surfactants for LiBr solution 2−EH is used here, and for the Carrol solution, PMC is introduced. The experimental results are shown in Figure 2.9, where different surfactants concentration are also used. In the case of LiBr solution, with high additive concentration, the surface tension reaches a minimum value of 34.5 $mN{\cdot}m^{-1}$, while the surface tension of Carrol solution with surfactant could be reduced to 39 $mN{\cdot}m^{-1}$. And from the result, it could be concluded that the surfactant solubility limit of 2−EH in the LiBr solution is much lower than 1−Phenylethanol in the Carrol solution. The solubility limit observed in this part is around 100 ppm and the surface tension remains at the minimum value, while [31] calculated the solubility limit as 27 ppm. For the Carrol solution, the solubility observed is about 1000 ppm, but more research is needed to quantify with accuracy this solubility limit.

Besides the additive in the liquid sample, the additive in the vapour phase is also considered a key parameter to surface tension, as [31] found that for LiBr solution, the effect of 2−EH from the vapour side is more significant than the effect from the liquid side with a drop volume method.

2.4.5 Experimental results of surface tension with gaseous additives

A liquid sample of LiBr 50% has been measured multiple times to verify the test procedure. At the beginning, the σ is 83.1 mN·m^{-1} before the test, after 1 minute boiling of the additive, the σ is 66.33 mN·m^{-1}. After 3 minutes of boiling, the mixture is assumed with an adequate distribution in the chamber. The measured σ is 46.2 mN·m^{-1}, and after another 5 minutes, the σ remains the same, so the measurement is considered stable. Then the gaseous additive flow is stopped, and after 10 minutes, the σ recovers to 65.65 mN·m^{-1} and stays. The surface tension increases when the airflow stops and will stay lower than the initial value due to the condensation of surfactant on the liquid interface. The additive will condense on the liquid surface but not reach the same concentration as the air-surfactant mixture vapour flow. Also, when the surfactant concentration in air is higher than 2000 ppm, the surface tension may remain almost constant even the mixture vapour flow is removed due to the high condensation level. Hence the measurement is set under the surfactant range under 2000 ppm. The results of the experiment is demonstrated in Figure 2.10 and 2.11 for LiBr$-$H$_2$O and Carrol$-$H$_2$O. Analysing the current results, the concentration of surfactant to reach minimum surface tension in vapor phase is higher than it in liquid phase for both solutions. However, the minimum surface tension measured values indicate that with suficient gaseous or liquid surfactant, the surface tension will finally reach the same level for the same liquid. As shown in Figure 2.9 and 2.10, the result of surface tension with gaseous additives is more progressive due to the distribution of the additives on the liquid-vapour interface. Also, the surface tension measurement discrepancy with liquid additive may be caused by the measurement method since the Du Noüy ring method is employed in this work, and the drop volume method is used in [31]. In the drop volume method, the surface will renew with every droplet, but the surface will not refresh with the Du Noüy ring or Willam plate method. Regarding the Carrol$-$H$_2$O, the limit concentration of the additive in the gaseous o liquid phase will not change much.

2.4.6 Contact angle measurement results

The contact angle is measured through the method proposed in Lamour et al. [35] with a relative uncertainty of 1% as shown in Appendix A.1. In order to assure the coherence of the experimental procedure, the contact angle measurement uses the liquid sample extracted from the MWR experiment (see chapter 4), which properties are reported in

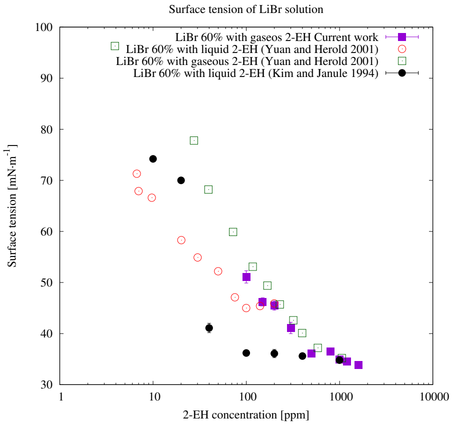

Figure 2.10: Experimental results of surface tension of LiBr−H_2O under 2−EH vapour and airflow mixture compared with other authors [31], [29]

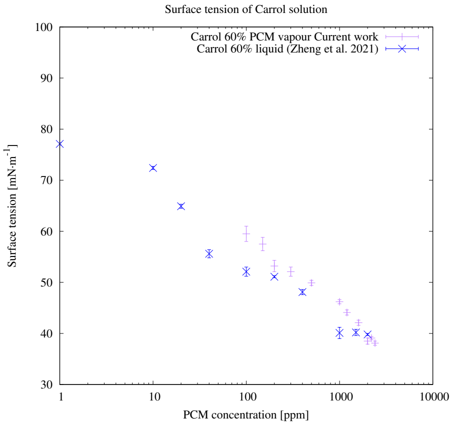

Figure 2.11: Experimental results of surface tension of Carrol−H_2O under PMC vapour and airflow mixture and compared with the surface tension with liquid surfactant in [4]

Table 2.14. The contact angle results are shown in Figure 2.12, in which the 60% LiBr solution has a higher contact angle on SS than on the PVC plate, and the 60% Carrol solution has a lower contact angle when compared with LiBr solution. Also, Figure 2.12 shows the linear relationship between surface tension and contact angle. The surface roughness may be the reason for the significant deviation. In this work, the SS solid base is untreated raw material, while in [33, 34] the SS plate surface roughness R_a is 0.01 μm and 287.4 nm, respectively. Besides the surface roughness, other parameters like liquid purity, droplet sample volume, and minor contamination of the system could also affect the final results of the contact angle. Moreover, the contact angle of solution with surfactant is also measured. It appears that the surfactant concentration of the liquid droplet is uncertain, and no reliable data could be obtained due to this uncertainty. According to [31], the solubility of LiBr solution is 27 ppm. However, the droplet sample is 3 μL, which means that if the surfactant concentration is higher than 27 ppm, the distribution of the surfactant cannot be predicted. This could lead to high uncertainty in the surfactant concentration of the sample extracted by the micropipette. Therefore, alternative methods or techniques may need to be considered to obtain accurate data on the contact angle of the solution with surfactant.

2.4.7 Concluding remarks of surface tension and contact angle

In this section, the surface tension of working pairs LiBr/H_2O and Carrol/H_2O is measured, and results are correlated with experimental results. When the liquid surfactant is added to the 60% mass LiBr solution, the surface tension will change from 91.3 to 34.8 $mN{\cdot}m^{-1}$ at additive 2−EH concentration 0−1000 ppm. Meanwhile, in the 65% Carrol solution with a liquid surfactant, the surface tension could be reduced from 74.7 to 39.8 $mN{\cdot}m^{-1}$ at additive 1-Phenylethanol concentration 0-5000 ppm. And the solubility limit observed of 2−EH in 60% LiBr solution is around 100 ppm, while the PMC in 65% Carrol solution is around 1000ppm. When gaseous surfactant is introduced to the solution, the surface tension will also decrease, as in the case it is injected in the liquid phase. However, a higher concentration is needed in the vapour phase to reach the surface tension limit than the additives mixed with the liquid solution for LiBr−H_2O. Meanwhile, for the Carrol−H_2O, this value will barely change.

In terms of contact angle, from concentration 40-60% LiBr solution, varies from 85-100° at stainless steel plate and 80-92° on a PVC plate, and for the Carrol solution on a stainless plate, the contact angle is 77-92°.

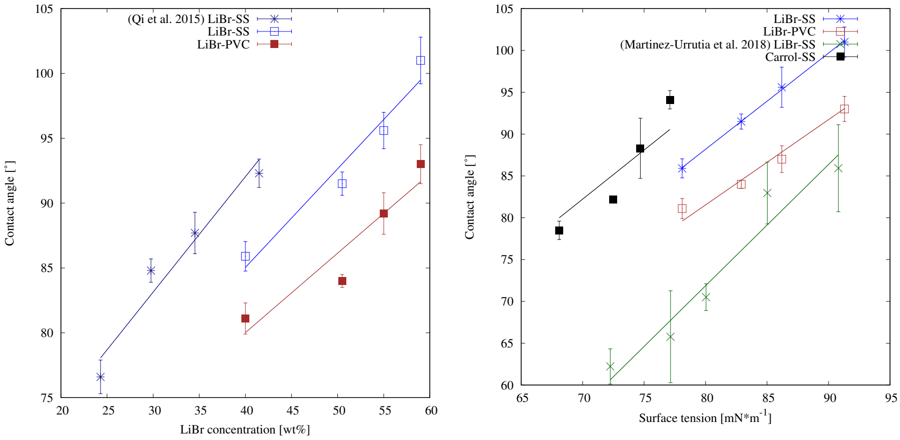

Figure 2.12: Experimental results of contact angle of LiBr and Carrol solution, and the measurements were made under 22.5±1°C, 35±1RH%, compared with [34], [33]. The left figure represents the LiBr solution contact angle change against concentration, and the right one represents the contact angle evolution of both LiBr and Carrol solution against surface tension, and the concentration is the only variable in the measurement. No additive is added in the measurement of contact angle.

Table 2.14: Properties of liquid tested in the experiments

	Thermophysical properties			
	σ [mN·m^{-1}]	ρ [kg·m^{-3}]	μ [Pa·s^{-1}]	θ [°]
Water – SS	72.2	997	8.9×10^{-4}	70
Water+2–EH – SS				70
Water – SS*				30
Water – Copper				60
LiBr 30% – SS	75	1262	0.0021	75
LiBr 50% – SS	83.1	1550	0.0035	85
LiBr 50%+2–EH – SS				85
LiBr 50% – Copper				65
Carrol 60% – SS	74	1538	0.0081	85
Carrol 60% + PMC – SS				85
Carrol 60% – SS*				30
Carrol 60% – Copper				65
EG – SS	46	0.016	1160	60
EG – SS*				30
EG – Copper				50

SS* represents the hydrophilic coating SS tube

2.5 Thermophysical properties of nanofluid working fluid absorbents

In this PhD thesis, nanofluids based on CuO and Al_2O_3 are prepared. Dispersant E414 was used as an anchor to ensure the stability of the nanofluid. The results show the nanofluid is stable within months. Thermophysical properties are calculated mathematically, and due to the low volume fraction (<1%), most properties will not change much like density, viscosity, specific heat and enthalpy. Meanwhile, the nanoparticles have an imporant effect on the thermal conductivity. According to the mathematical modelling, the thermal conductivity could increase up to 10% depending on the nanoparticle fraction. Nanofluid is a liquid with the suspension of nanoparticles whose diameter is within 1-100 nm, and the nanoparticles are generally not soluble in the liquid. Nanofluids have great potential for improving heat-transfer efficiency and are employed in various thermal applications in the automotive industry, heat exchangers, solar power generation, absorption systems, and more. The enhancement of the thermophysical properties of nanofluid compared to the base fluid is generally related to the volume fraction of the nanoparticle. Many authors studied the enhanced thermophysical properties of nanofluid, in which thermal conductivity was the most investigated. Jung et al. [42] measured the thermal conductivity of $LiBr-H_2O$ binary mixture with Al_2O_3 with a dispersion of PVA and shown that LiBr 50% solution with Al_2O_3 at 0.1% volume fraction could increase 2% of the thermal conductivity. Khamliche et al. [43] reports experimental data of thermal conductivity of binary fluid with nanoparticle silver. With volume fraction at 0.1%, the thermal conductivity increased 30% for pure liquid EG.

Lee et al. [44] used oxide nanofluids with Al_2O_3 and CuO particles and measured the thermal conductivity by a transient hot-wire method. Their results indicate that the theoretical model can predict the thermal conductivity of nanofluids containing large agglomerated Al_2O_3 particles but may be inadequate for CuO particles. Due to not only the shape but also the particle size affect the thermal conductivity increase. Xue et al. [45] proposed a novel model of the effective thermal conductivity for nanofluid. Nanofluid of oil/carbon nanotube, H_2O/Al_2O_3 show good agreement with the experimental data. Wang et al. [46] used the one-dimensional, steady-state parallel-plate method to measure the thermal conductivity of nanoparticle fluid mixtures. The Al_2O_3 and CuO used to have a diameter of 28 and 23nm, respectively. Due to the different mixture methods, the experimental data vary importantly with the sample nanofluid. Masuda et al. [47] reported that Al_2O_3 at a volume fraction of 3% can increase the thermal conductivity of H_2O by 20%, Lee et al. [44] obtained an increase of 8% and Wang et al. [46] obtained

12%. Jana et al. [48] used single and hybrid nanoparticles for the thermal conductivity enhancement of the liquid. The particles used are CNTs(Carbon nanotubes) (10nm in diameter and 5-10μm in length), AuNP(Au nanoparticle), and CuNP(Cu nanoparticle) of 15 and 35 nm, respectively. The thermal conductivity could increase 80% at a volume fraction of 0.3% CuNP in the mixture CuNPs+laurate salt + H_2O, and for CNTs + H_2O, the increase at 0.3% is 22%. As nanofluid enhances thermophysical properties, it could increase the heat and mass transfer coefficient in many applications. Gao et al. [49] investigated the effect of CuO nanoparticles in falling film absorption numerically. Zhang et al. [50] studied the influence of nanofluid with Cu, Al_2O_3, and CNTs on the falling film absorption. They found that the small nanoparticles size and larger mass fraction lead to a better the effective absorption ratio, and the absorption rate could increase by 125%. In this section, a numerical model is built to investigate the effect of nanofluid with nanoparticle of Al_2O_3 and CuO on heat transfer in the falling film compared with the analytical model. Besides, experimental data are used to validate the results to measure the liquid interface and bulk temperatures, validating the falling film temperature distribution of the model.

2.5.1 Preparation of nanofluids

Two different nanofluids were prepared by suspending Al_2O_3 in the H_2O and EG. Also, according to Wang et al. [41], if mixing dispersant (E414) with the corresponding liquid, the stability of the nanofluid could be improved. First, E414 is mixed to pure distilled H_2O or EG. Then, the liquid is stirred for one hour. In the next step, Al_2O_3 powder is added, and the suspension is stirred again for another hour. Finally, the mixture is introduced in an ultrasonic sonicator bath for 30 minutes. Figure 2.13 shows the example of nanofluid and the materials used. 2.14 show the nanofluid of EG with CuO and Al_2O_3, in which CuO is black and Al_2O_3 is white. The picture is taken one month after the nanofluid preparation.

After acquiring, nanofluid is not put into the process immediately as the suspension's stability of the nanoparticles has to be confirmed. Figure 2.14 shows the nanofluid of H_2O and EG with 0.5vol%, volumetric percentage (ϕ), after one hour, one day, and one week. The nanofluid is considered stable if no sediment is observed in the liquid, . Two samples of H_2O and EG with nanoparticles of Al_2O_3 are shown in Figure 2.13. The ϕ is calculated as Equation 2.37.

$$\phi = \frac{m'_\mathrm{p}/\rho_\mathrm{p}}{m'_\mathrm{p}/\rho_\mathrm{p} + m'_\mathrm{l}/\rho_\mathrm{l}} \tag{2.37}$$

Figure 2.13: Nanofluid of LiBr 50% at 1 vol% with E414

Figure 2.14: Nanofluid of EG with 0.1 vol% CuO and Al_2O_3 and 2% E414

Table 2.15: Thermophysical properties of of basefluid with ϕ=5% Al_2O_3 at 25 °C

		LiBr 50wt%[a]	Carrol 60wt%[b]	H_2O[c]	EG[d]
ρC_p	basefluid	3.16E6	3.42E6	4.17E6	2.70E6
$[J \cdot m^{-3} K^{-1}]$	nanofluid	3.01E6	3.26E6	3.97E6	2.57E6
μ	basefluid	3.53E-3	6.88E-3	8.9E-4	1.61E-2
$[m^2 s^{-1}]$	nanofluid	3.95E-3	7.71E-3	9.96E-4	1.83E-2
λ	basefluid	0.444	0.51	0.62	0.25
$[W \cdot m^{-1} K^{-1}]$	nanofluid	0.503	0.577	0.677	0.285

---

[a] LiBr solution properties are extracted from [7]

[b] Carrol solution properties are extracted from [9]

[c] H_2O properties are extracted from [10]

[d] H_2O properties are extracted from [10]

where m'_p is the mass of nanoparticles, m'_l is the liquid mass, ρ_p, ρ_l are the density of the nanoparticles and the liquid, respectively.

2.5.2 Thermophysical properties of nanofluids

The modified thermophysical properties of nanofluid is calculated according to Xuan et al. [6]. The viscosity μ, specific heat C_p, density ρ, and thermal conductivity λ could be calculated as Equation 2.38–2.40.

$$\mu_{eff} = \mu_f(1 + 2.5\phi) \tag{2.38}$$

$$(\rho C_p) = (1-\phi)(\rho C_p)_l + \phi(\rho C_p)_s \tag{2.39}$$

$$\frac{\lambda_{eff}}{\lambda_l} = \frac{\lambda_p + 2\lambda_l - 2\phi(\lambda_l - \lambda_p)}{\lambda_p + 2\lambda_f + \phi(\lambda_f - \lambda_p)} \tag{2.40}$$

The detailed properties of nanofluid based on LiBr 50wt% solution with $Al_2O_3 \phi = 5\%$ are listed in Table 2.15 The viscosity increased around 10%, the ρC_p decreased around 5% and the thermal conductivity increased around 14%.

NOMENCLATURE

Name	**Description**
a	Activity [-]
a'	Short range fitting parameter Equation 2.23 [-]
a_1,a_2	Middle range parameter in the LIQUAC method Equation 2.14 [-]
A'	Debye-Hückel constant [-]
A_0,A_1,A_2,A_3	Fitted coefficients Equation 2.33 [-]
b	Debye-Hückel parameters Equation 2.6 [-]
b'	Fitted parameters of group Equation 2.14 [-]
B	Fitted parameters Equation 2.27 [-]
B'	Interaction parameter (Equation 2.1) [-]
B''	Fitted coefficient Equation 2.36 [-]
B_0,B_1,B_2,B_3	Fitted coefficients Equation 2.33 [-]
c'	Fitted parameters of ion Equation 2.14 [-]
C	Solute weight concentration [%]
C'	Ajustable parameter (Equation 2.1) [-]
C_0,C_1,C_2,C_3	Fitted coefficients Equation 2.33 [-]
COP	Coefficient of performance [-]
$C\mathrm{p}$	Specific heat capacity $[\mathrm{J}\cdot(\mathrm{kg}\cdot\mathrm{K})^{-1}]$
d	Molar density [kg·mol^{-1}]
D	Relative dielectric constant [-]
e	Exergy $[\mathrm{J}\cdot\mathrm{kg}^{-1}]$
EC	Electrical conductivity [mS·cm^{-1}]
E_D	Exergy destruction rate [W]
F	Fraction of Van der Walls surface area [-]
h	Specific enthalpy $[\mathrm{J}\cdot\mathrm{kg}^{-1}]$
I	Ionic strength [-]
m'	Mass [kg]
$\dot{m}$	Mass flow rate $[\mathrm{kg}\cdot\mathrm{s}^{-1}]$
M	Molar mass [g·mol^{-1}]
o	Perimeter of the platinum ring [cm]
P	Pressure Pa]
q	Van der Waals surface area [-]
Q	Heat flux [W]
Q_k	Relative van der Walls surface area [-]
r	Van der Waals volume [-]
r'	Thickness of the wire of the ring [cm]
s	Specific entropy $[\mathrm{J}\cdot(\mathrm{kg}\cdot\mathrm{K})^{-1}]$
R_k	Relative van der Wall volume [-]
R	Gas constant $[\mathrm{J}\cdot(\mathrm{kg}\cdot\mathrm{K})^{-1}]$
R'	Diameter of the ring [cm]

Name	**Description**
T	Temperature [°C]
V	Fraction of Van der waals volume [-]
W	Potential [W]
z	Charge number of ion [-]
Greek letter	**Description**
α	Heat transfer conductence [W·K^{-1}]
β	Mass transfer coefficient [m·s^{-1}]
γ	Activity coefficient [-]
ε	Standard chemical exergy [$\mathrm{J \cdot kg^{-1}}$]
η	Percentage [%]
θ	Contact angle [$\circ$]
ϑ	Dimensionless size parameter [-]
ι	Molality [mol·L^{-1}]
Θ	Surface area fraction [-]
λ	Thermal conductivity [Wm^{-1}K^{-1}]
μ	Dynamic viscosity [Pa·s^{-1}]
Ξ	Cation [-]
Π	Anion [-]
ϖ	Number of moles of ion produced [mol]
ρ	Density [kg·m^{-3}]
ϱ	Deviation [$-$]
σ	Surface tension [mN·m]
ς	Volume fraction of group [-]
ϕ	Volume fraction of particle [-]
φ	Molar fraction [-]
χ	Correction parameter Equation 2.34 [-]
Ψ	Adjustable temperature-independent parameter [-]
Abbreviation	**Description**
2-EH	2-Ethylhexanol
CTAC	Cetyltrimethyl ammonium chloride
CTAB	Cetyltrimethyl ammonium bromide
PMC	Phenylmethylcarbinol, 1$-$Phenylethanol
RH	Relative humidity
SS	Stainless steel
VLE	Vapor-liquid equilibrium

wt	Weight ratio

Subscripts & Superscripts	**Description**
0	Reference point
air	Airflow
ABS	Absorber
ch	Chemical
C	Combinatorial part
dis	Chemical dissolvation
D	Destruction
eff	Effective
ex	Exergy
EVA	Evaporator
f	Fluid
group	Constructure group in organic compound
i,j	Subscripts as sequence of numbers, superscripts as exponent
ion	Ion
l	Liquid
LR	Long range
m	Component
mea	Measure
mix	Mixture
mol	Molar
MR	Middle range
p	Nanoparticle
phy	Physical
pri	Primary
R	Residual part
solv	Solvent
solv2	Other solvent
std	Standard chemical
SR	Short range
SYS	System
tot	Total

References

[1] J. Zheng, J. Chiva, J. Castro, Y. Liu, A. Oliva, Electrical conductivity of concentrated LiBr Ethylene-Glycol and water ternary system, Journal of Physics: Conference Series 2116 (1) (2021) 012069. `doi:10.1088/1742-6596/2116/1/012069`.

[2] J. Zheng, J. Castro, A. Oliva, C. Oliet, Energy and exergy analysis of an absorption system with working pairs LiBr-H2O and Carrol-H2O at applications of cooling and heating, International Journal of Refrigeration 132 (September) (2021) 156–171. `doi:10.1016/j.ijrefrig.2021.09.011`.

[3] J. Zheng, J. Castro, E. Garcia-Rivera, C. Oliet, A. Oliva, Study of the influence of surfactants and surface treatments on the minimum wetting rate of falling films of aqueous LiBr and Carrol solutions, International Journal of Refrigeration 141 (May) (2022) 146–157. `doi:10.1016/j.ijrefrig.2022.05.023`.

[4] J. Zheng, J. Castro, C. Oliet, A. Oliva, Surface tension and contact angle measurement of LiBr and Carrol solution, in: International sorption Heat pump Congress, 2021, pp. 74—-78.

[5] J. Zheng, J. Castro, G. Papakokkinos, A. Oliva, Sensitivity study to an absorption system performance considering heat and mass transfer enhancements, in: Purdue Congress, 2022.

[6] Y. Xuan, W. Roetzel, Conceptions for heat transfer correlation of nanofluids, International Journal of Heat and Mass Transfer 43 (19) (2000) 3701—-3707. `doi:10.1016/j.aej.2017.01.005`.

[7] L. McNeely, Thermodynamic properties of aqueous solutions of lithium bromide, ASHRAE Transactions 85 (1) (1979) 413–434.

[8] Y. Kaita, Thermodynamic properties of lithium bromide-water solutions at high temperatures, International Journal of Refrigeration 24 (5) (2001) 374–390. `doi:10.1016/S0140-7007(00)00039-6`.

[9] W. Biermann, Proprties of the Carrol system and a machine design for solar-powered, air-cooled, absorption space cooling. Phase I and Phase II. Final report, September 1977-March 1979, Tech. rep., Carrier Corp., Syracuse, NY (USA). Energy Systems Div. (1981).

[10] A.~Kramida, Yu.~Ralchenko, J.~Reader, No Title, NIST Atomic Spectra Database (ver. 5.7.1), [Online]. Available: {\tt{https://physics.nist.gov/asd}} [2015, April 16]. National Institute of Standards and Technology, Gaithersburg, MD. (2019).

[11] I. H. Bell, J. Wronski, S. Quoilin, V. Lemort, Pure and Pseudo-pure Fluid Thermophysical Property Evaluation and the Open-Source Thermophysical Property Library CoolProp, Industrial & Engineering Chemistry Research 53 (6) (2014) 2498–2508. `doi:10.1021/ie4033999`.

[12] V. Taghikhani, H. Modarress, J. H. Vera, Individual anionic activity coefficients in aqueous electrolyte solutions of LiCl and LiBr, Fluid Phase Equilibria 166 (1) (1999) 67–77. `doi:10.1016/S0378-3812(99)00291-5`.

[13] J. Kiepe, O. Noll, J. Gmehling, Modified LIQUAC and modified LIFAC - A further development of electrolyte models for the reliable prediction of phase equilibria with strong electrolytes, Industrial and Engineering Chemistry Research 45 (7) (2006) 2361–2373. `doi:10.1021/ie0510122`.

[14] A. Mohs, J. Gmehling, A revised LIQUAC and LIFAC model (LIQUAC*/LIFAC*) for the prediction of properties of electrolyte containing solutions, Fluid Phase Equilibria 337 (2013) 311–322. `doi:10.1016/j.fluid.2012.09.023`.

[15] C. Marcolli, T. Peter, Water activity in polyol / water systems : new UNIFAC parameterization, Atmospheric Chemistry and Physics 5 (2) (2005) 1501–1527.

[16] H. K. Hansen, P. Rasmussen, A. Fredenslund, M. Schiller, J. Gmehling, Vapor-Liquid Equilibria by UNIFAC Group Contribution. 5. Revision and Extension, Industrial and Engineering Chemistry Research 30 (10) (1991) 2352–2355. `doi:10.1021/ie00058a017`.

[17] T. J. Kotas, The Exergy Method of Thermal plant Analysis, Paragon Publishing, 2013.

[18] R. Palacios-Bereche, R. Gonzales, S. A. Nebra, Exergy calculation of lithium bromide-water solution and its application in the exergetic evaluation of absorption refrigeration systems LiBr-H2O, International Journal of Energy Research 36 (2) (2012) 166–181. `doi:10.1002/er.1790`.

[19] L. Labra, D. Juárez-Romero, J. Siqueiros, A. Coronas, D. Salavera, Measurement of properties of a lithium bromide aqueous solution for the determination of the

concentration for a prototype absorption machine, Applied Thermal Engineering 114 (2017) 1186–1192. `doi:10.1016/j.applthermaleng.2016.10.162`.

[20] J. Castro, A. Oliva, C. D. Pérez-Segarra, J. Cadafalch, Evaluation of a small capacity, hot water driven, air-cooled H2O-LiBr absorption machine, HVAC and R Research 13 (1) (2007) 59–75. `doi:10.1080/10789669.2007.10390944`.

[21] R. Best, W. Rivera, A. Oskam, Thermodynamic Design Data for Absorption Heat Pump Systems Operating on Water-Carrol. Part II: Heating, Heat Recovery Systems and CHP 15 (5) (1995) 435–444.

[22] H. Semat, R. Katz, Electrical conduction in liquids and solids, Physics (1958) 524–538.

[23] I. Frled, Electrical Conductivity of Concentrated Lithium Bromide Aqueous Solutions, J. Chem. Eng. Data 28 (1983) 127–130.

[24] A. De Diego, A. Usobiaga, J. M. Madariaga, Modification of the falkenhagen equation to fit conductimetric data for concentrated electrolyte solutions, Journal of Electroanalytical Chemistry 430 (1-2) (1997) 263–268. `doi:10.1016/S0022-0728(97)00261-1`.

[25] H. Falkenhagen, M. Leist, G. Kelbg, Zur theorie der leitfähigkeit starker nicht assoziierender elektrolyte bei höheren konzentrationen, Annalen der Physik 446 (1) (1952) 51–59.

[26] J. Sun, L. Fu, S. Zhang, W. Hou, Concentration measurement of lithium bromide aqueous solution by electrical resistivity, ASME International Mechanical Engineering Congress and Exposition, Proceedings (IMECE) 5 (PARTS A AND B) (2010) 185–188. `doi:10.1115/IMECE2010-37350`.

[27] S. Osta-Omar, C. Micallef, Determination of Concentration of the Aqueous Lithium–Bromide Solution in a Vapour Absorption Refrigeration System by Measurement of Electrical Conductivity and Temperature, Data 2 (1) (2017) 6. `doi:10.3390/data2010006`.

[28] W. Yao, F. Setterwall, H. Bjuretröm, Surface Tension of Lithium Bromide Solutions with Heat-Transfer Additives, Journal of Chemical and Engineering Data 36 (1) (1991) 96–98. `doi:10.1021/je00001a029`.

[29] K. J. Kim, V. P. Janule, Surface tension of aqueous lithium bromide with 2-ethyl-1-hexanol, Journal of Chemical & Engineering Data 21 (6) (1994) 839–848. `doi:10.1016/0735-1933(94)90037-X`.

[30] W. H. Cai, W. W. Kong, Y. Wang, M. S. Zhu, X. L. Wang, Surface tension of lithium bromide aqueous solution/ammonia with additives and nano-particles, Journal of Central South University 22 (5) (2015) 1979–1985. `doi:10.1007/s11771-015-2718-0`.

[31] Z. Yuan, K. E. Herold, Surface tension of pure water and aqueous lithium bromide with 2-ethyl-hexanol, Applied Thermal Engineering 21 (2001) 881–897.

[32] G. Löf, Design methods for active solar systems, The MIT Press, 1993.

[33] A. Martinez-Urrutia, P. Fernandez de Arroiabe, M. Ramirez, M. Martinez-Agirre, M. Mounir Bou-Ali, Contact angle measurement for LiBr aqueous solutions on different surface materials used in absorption systems, International Journal of Refrigeration 95 (2018) 182–188. `doi:10.1016/j.ijrefrig.2018.05.041`.

[34] R. Qi, L. Lu, Y. Jiang, Investigation on the liquid contact angle and its influence for liquid desiccant dehumidification system, International Journal of Heat and Mass Transfer 88 (2015) 210–217. `doi:10.1016/j.ijheatmasstransfer.2015.04.080`.

[35] G. Lamour, A. Hamraoui, A. Buvailo, Y. Xing, S. Keuleyan, V. Prakash, A. Eftekhari-Bafrooei, E. Borguet, Contact angle measurements using a simplified experimental setup, Journal of Chemical Education 87 (12) (2010) 1403–1407. `doi:10.1021/ed100468u`.

[36] A. D97, Standard test method for pour point of petroleum products, Annual Book of Standards.

[37] N. B. Vargaftik, B. N. Volkov, L. D. Voljak, International Tables of Water Surface Tension, J. Phys. Chem. Ref. Data 12 (3) (1983) 817–820.

[38] S. Azizian, M. Hemmati, Surface tension of binary mixtures of ethanol + ethylene glycol from 20 to 50°C, Journal of Chemical and Engineering Data 48 (3) (2003) 662–663. `doi:10.1021/je025639s`.

[39] W. D. Harkins, The physical chemistry of surface films, Reinhold, 1952.

[40] A. W. Adamson, A. P. Gast, Others, Physical chemistry of surfaces, Vol. 15, Interscience publishers New York, 1967.

[41] G. Wang, P. Dong, Y. Lu, M. Zeng, Q. Zhang, Experimental and theoretical investigation on the surface tension of nano-Lithium Bromide solution, International Communications in Heat and Mass Transfer 123 (March) (2021) 105231. `doi:10.1016/j.icheatmasstransfer.2021.105231`.

[42] J. Y. Jung, C. Cho, W. H. Lee, Y. T. Kang, Thermal conductivity measurement and characterization of binary nanofluids, International Journal of Heat and Mass Transfer 54 (9-10) (2011) 1728–1733. `doi:10.1016/j.ijheatmasstransfer.2011.01.021`.

[43] T. Khamliche, S. Khamlich, T. B. Doyle, D. Makinde, M. Maaza, Thermal conductivity enhancement of nano-silver particles dispersed ethylene glycol based nanofluids, Materials Research Express 5 (3). `doi:10.1088/2053-1591/aab27a`.

[44] S. Lee, S. Choi, S. Li, J. Eastman, Measuring Thermal Conductivity of Fluids Containing Oxide Nanoparticles, Journal of Heat Transfer 121 (1999) 280–289.

[45] Q. Z. Xue, Model for effective thermal conductivity of nanofluids, Physics Letters, Section A: General, Atomic and Solid State Physics 307 (5-6) (2003) 313–317. `doi:10.1016/S0375-9601(02)01728-0`.

[46] X. Wang, X. Xu, S. U. S. Choi, Thermal Conductivity of Nanoparticle-Fluid Mixture, Journal of Thermophysics and Heat Transfer 13 (4) (1999) 474–480.

[47] H. Masuda, A. Ebata, K. Teramae, Alteration of thermal conductivity and viscosity of liquid by dispersing ultra-fine particles. Dispersion of Al2O3, SiO2 and TiO2 ultra-fine particles, ASHRAE Transactions.

[48] S. Jana, A. Salehi-Khojin, W. H. Zhong, Enhancement of fluid thermal conductivity by the addition of single and hybrid nano-additives, Thermochimica Acta 462 (1-2) (2007) 45–55. `doi:10.1016/j.tca.2007.06.009`.

[49] H. Gao, F. Mao, Y. Song, J. Hong, Y. Yan, Effect of adding copper oxide nanoparticles on the mass/heat transfer in falling film absorption, Applied Thermal Engineering 181 (August). `doi:10.1016/j.applthermaleng.2020.115937`.

[50] L. Zhang, Z. Fu, Y. Liu, L. Jin, Q. Zhang, W. Hu, Experimental study on enhancement of falling film absorption process by adding various nanoparticles, International Communications in Heat and Mass Transfer 92 (2018) 100–106. `doi:10.1016/j.icheatmasstransfer.2018.02.011`.

3

Minumum wetting rate modelling and experimental validation

Abstract

The liquid falling film is widely employed in heat and mass transfer processes and various engineering applications. Wettability is one of the critical parameters especially in the design of falling film type of heat exchanger. High wettability could guarantee a low minimum mass flow rate which could decrease the pumping power and, therefore, the size of the solution pumps and the working fluid loaded. However, studies about the relationship between surface tension, contact angle, and minimum wetting rate are limited. In this section, working pairs LiBr−H_2O and Carrol−H_2O (Carrol contains LiBr and EG −Ethylene glycol− with a mass ratio at 4.5:1) with additives 2−EH (2−Ethyl−1−hexanol) and PMC (1−Phenylethanol) are studied focusing on the minimum wetting rate (MWR). MWR is measured in an annular falling film experimental set-up employing the dewetting method using different materials' tubes and fluids. The experimental results of the MWR test agree with theoretical predictions and empirical correlations with a discrepancy of less than 10%. When the metal tube is coated with a hydrophilic surface, a contact angle value of 30° is achieved, and the minimum mass flow of H_2O to achieve complete wettability on the coated SS tube is reduced from 0.096 to 0.025 $kg{\cdot}m^{-1}{\cdot}s^{-1}$.

3.1 Introduction of minmum wetting rate

Wetting ability is a critical parameter of the absorber in the absorption system to achieve a low mass flow. The wettability is determined by the minimum wetting rate (MWR) parameter, defined as the minimum flow rate per unit length required to maintain a fully wetting tube. For a small-capacity absorption machine, low MWR is especially critical since small pumps are desirable with minimum pumping power. Furthermore, for air−cooled systems with a vertical falling film type absorber, the MWR is an even more critical parameter, as the solution flow is distributed to many tubes. For example, in [1], [2], [3], the wettability is explained as a critical factor of the performance due to the difficulties in flow distribution with tube columns in the absorber. MWR value depends mainly on surface tension σ, contact angle θ, and viscosity μ, among other properties. In general lowering surface tension and the contact angle could lead to a lower MWR on the same material. On the one hand, mixing additives into the solution is a standard method to reduce the surface tension of the solution; on the other hand, the contact angle is a parameter that depends on both the liquid and solid phases of the contact area. Though many efforts are dedicated to this topic, surface tension and contact angle measurements show ineluctable differences between different references.

After the surface tension and contact angle are measured, these data are sufficient to correlate the MWR empirically. The MWR is the lowest flow rate needed to ensure that the surface remains covered by a continuous, thin liquid film. The mean film thickness at MWR is known as mean liquid film thickness (MLFT). Many authors have proposed the correlation of MWR under different conditions with theoretical or experimental methods. The correlations are listed in Table 3.1. All the correlations in the table are reformed to a similar format for the convenience of comparison. According to the power exponent, the table shows that contact angle and surface tension are the dominant variables in this function. On the other hand, MWR correlation could provide empirical information required by the simulation of the absorption system in [4] and [5]. Ponter et al. [7] used a similar method and solved NS equations on a dry patch of a uniform laminar stream and validated with experimental results. In his results, the observed MWR on a 30 cm long copper tube with ethanol-H_2O at 20°C, with surface roughness $15{-}25\times10^{-6}$ cm, is 0.880 $g\cdot cm^{-1}\cdot s^{-1}$ while at a stainless steel tube is 0.555 $g\cdot cm^{-1}\cdot s^{-1}$. Munakata et al. [8] mentioned that the wetting behaviour of the liquid in the range of high viscosity (> 0.1 $Pa\cdot s^{-1}$ like Glycerol-H_2O mixture) is sharply different from the previous works. Instead of only considering the inertia force, the model was modified with the viscous force, obtaining a semi−empirical equation. The work

Table 3.1: Correlations for MWR

Author	Expressions	Method	Liquids
[6]	$\Gamma = 0.254(1-\cos\theta)^{0.6}\sigma^{0.6}\rho^{0.6}\mu^{0.2}$	Theoretical	–
	$\delta = 1.34\left(\frac{\sigma}{\rho}\right)^{\frac{1}{5}}\left(\frac{\mu}{\rho g}\right)^{\frac{2}{5}}$		
[7]	$\Gamma = 0.71(1-\cos\theta)^{0.6}\sigma^{0.6}\rho^{0.6}\mu^{0.2}$	Theoretical	–
	$\delta = \left(\frac{3\Gamma\mu}{\rho^2 g}\right)^{\frac{1}{3}}$	Nusselt film theory	–
[8]	$1.59(\frac{\Gamma}{\mu})^{\frac{2}{3}} + 0.945(\frac{\Gamma}{\mu})^{\frac{5}{3}} = (\frac{\rho\sigma^3}{g\mu^4})^{(\frac{1}{3})}$	Experimental*	Glycerol–H_2O
	$\delta = \left(\frac{3\Gamma\mu}{\rho^2 g}\right)^{\frac{1}{3}}$	Nusselt film theory	–
[9]	$\Gamma = 0.905(1-\cos\theta)^{0.6}\sigma^{0.6}\rho^{0.6}\mu^{0.2}$	Theoretical	–
	$\delta = \left(\frac{45}{7}\right)^{\frac{1}{5}}\left(\frac{\mu^2\sigma}{\rho^3 g^2}\right)^{\frac{1}{5}}(1-\cos\theta)^{\frac{1}{5}}$	Laminar rivulet thickness	–
[10]	$\Gamma = (0.424(1-\cos\theta)^{0.623} + 0.165(1-\cos\theta)^{2.09})\sigma^{0.6}\rho^{0.6}\mu^{0.2}$	Theoretical	–
	$\delta = 15(1-\cos\theta)^{1.1}\frac{\mu^2\sigma}{\rho^3 g^2}$		
[11]	$\Gamma = 0.13(1-\cos\theta)^{0.764}\sigma^{0.764}\rho^{0.255}\mu^{-0.018}$	Experimental	Glycerol–H_2O Ethanol–H_2O $CaCl_2$–H_2O

*The correlation was extract from [8] at a specific case with H_2O on stainless steel tube

focused on experiments and tested with a different liquid distributor of stainless steel wetted–wall columns; the experimental results agreed with the predicted numerical results in the wide range of Ka. Doniec [9] used a similar method and proposed a more detailed numerical result. However, exact equations should be applied for films with thicknesses below 0.1 mm and small contact angles (below 5°) since discrepancies may exceed 10%. El-Genk et al. [10] used minimization of the total energy of a stable liquid rivulet method (MTE). When their results were compared to other correlations, the expression of minimum dimensionless mass flow rate $\Delta_{\min}$ as a function of contact angle is close to results from Hartley et al. [12], work based on film breakdown (FB). However, their results were higher than [9] and [13], in which the $\Delta_{\min}$ is solved with minimum liquid film thickness based on MTE. Moreover, the predictions of the MWR for a stable dry patch agree with experimental results with ±20%. Morison et al. [11] obtained experimental data with H_2O, H_2O/glycerol, ethanol/H_2O, and $CaCl_2$/H_2O with an absorber with several tubes and a distributor instead of a single tube absorber. According to the results, it was reported that viscosity and density had a non-significant effect on MWR and the main influences were surface tension and contact angle. For H_2O at 25 °C, the contact angle was 88°, and the surface tension 72 $mN{\cdot}m^{-1}$, for a flow rate of 0.104 ± 0.005 $kg{\cdot}m^{-1}{\cdot}s^{-1}$. Lu et al. [14] presented the influence of different liquid distribution systems and physical properties of the working fluid on the wetting behaviour on a vertical flat plate. The experiments are carried out under the Reynolds number range of $0.5 < Re < 460$, with the fluorescence intensity technique for the flow visualization and different types of distributors. Higher MWR values were required for wetting experiments than for dewetting experiments, the phenomena was observed in the experiments. Dewetting means start the experiment with a higher flow rate than MWR, then gradually reduce the flow rate until the film break. Furthermore, the experimental results from [14] for MWR agreed well with El-Genk et al. [10]. Thus, from all the information above, decreasing surface tension or contact angle is efficient in decreasing the MWR.

In this section, the MWR is measured with H_2O, EG, LiBr−H_2O, and Carrol−H_2O on different tubes (stainless steel, copper) to validate the models employed. The properties of the liquids are listed in Chapter 2. Considering the effect of surface tension and contact angle on the MWR, surfactants are introduced to the liquid and analysed for their influence on MWR. Moreover, a sol−gel treatment to SS surface proposed by Ye et al. [15] is employed to create a hydrophilic coating to explore the effect of contact angle, which according to the correlations more critical than surface tension. The solution(LiBr-H_2O, Carrol-H_2O) condition of temperature and concentration are extracted from [5] to predict the MWR in a falling film-type vertical tube absorber.

3.2 MWR experimental set-up

The liquids used in these measurements are H_2O, EG, LiBr-H_2O 50% solution, and Carrol-H_2O 60% solution. To obtain the MWR, dewetting method as mentioned in Lu et al. [14] is employed. For LiBr−H_2O and Carrol−H_2O, the corresponding additive is added to the liquid solution, as explained in the previous part. The measurement set−up is shown as Figure 3.1. The liquid is loaded into the distributor and forms a liquid film around the vertical tube. Then the liquid solution is pumped to the distributor again. A Coriolis flowmeter is employed to measure the density and mass flow rate, and two PT100 sensors are used to measure the temperatures at the inlet/outlet. A laser distance sensor is placed to detect any vibration effect and the concentric level, assuring that the tube is vertical. Besides, a thermographic camera is employed to catch the dry patch if there is difficulty with visual discrepancy. The maximum relative uncertainty for the MWR is around 8%, as shown in A.1.

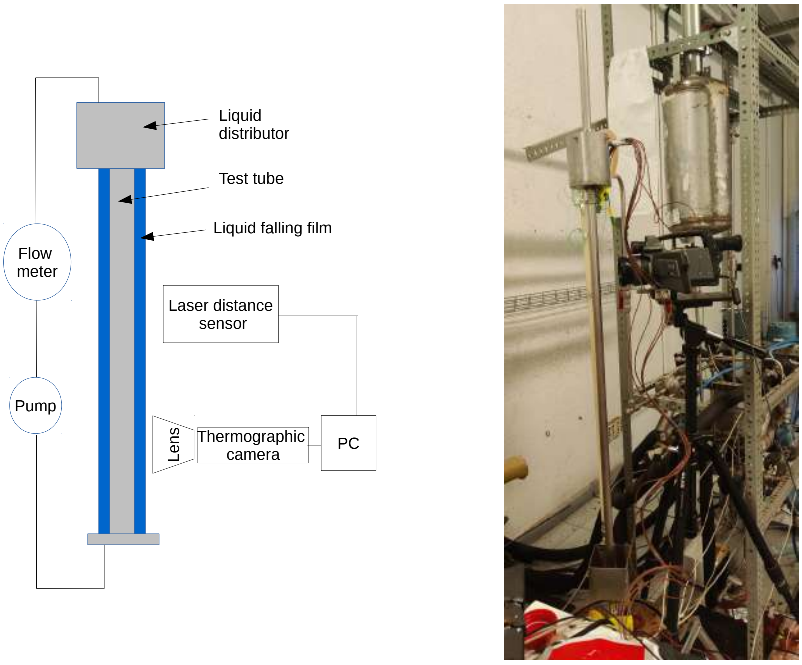

(a) Sketch of the test rig

(b) Foto of the experimental setup

Figure 3.1: MWR measurement experimental setup

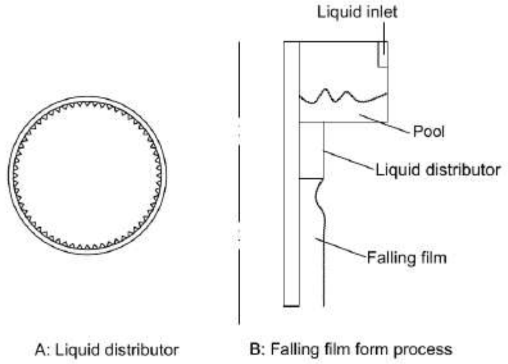

Figure 3.2: Sketch of the liquid distributor system

3.3 Sample preparation and measurement process

The gear pump is turned on until a stable falling film is formed on the tube to perform each experimental test. Then the flow rate is slowly decreased until a steady dry patch appears. When the dry−patch could remain for more than 5 minutes using the dewetting method, the MWR is considered stable. The liquid film distributor system is shown in Figure 3.2. There is a sawtooth structure inside the distributor that could ensure that the distributor outlet's velocity is nearly uniform.

All temperature is set around 20°C to avoid evaporation in the film. The temperature difference between the inlet and outlet of the falling film is less than 1°C.

3.4 MWR experimental results

The MWR results are shown in Figure 3.3 and Table 3.2 with correlations from other authors. In the experiment, besides the materials of tubes, a hydrophilic treatment proposed by Ye et al. [15] is also considered. Since the treatment process includes a high−temperature procedure, only the metal tubes from the proposed ones have been treated. After the treatment, only the SS tube surface shows a uniform surface of enough quality. Therefore the hydrophilic copper tube is not considered. Finally, three different metal tubes are employed: untreated SS 316L tube, untreated copper tube, and SS tube with super−hydrophilic coating. The properties of the corresponding liquid

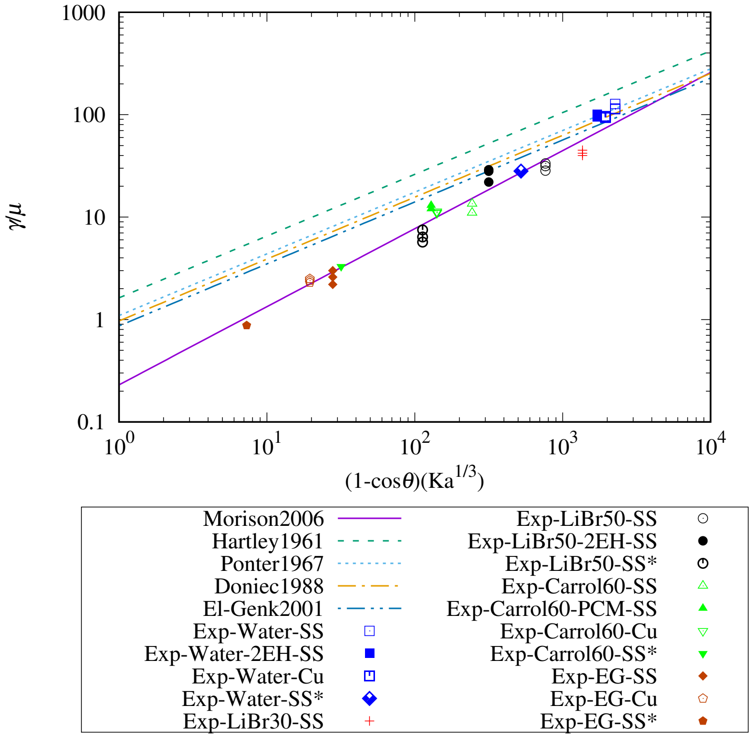

Figure 3.3: Dimensionless measurement results with different kinds of liquids, tubes and compared with correlations of other authors. The results contain EG, H_2O with and without surfactant (2−EH), LiBr 30% and LiBr 50% solution with and without surfactant (2−EH), and Carrol 60% solution with and without surfactant (PMC) on stainless steel tube (SS), or copper tube (Cu). A SS tube with a hydrophilic coating (SS*) is also introduced.

Table 3.2: Average MWR in kg(m·s)$^{-1}$ for different liquids and tubes. The liquid and tubes are the same as shown in the Figure 3.3.

	MWR at different tubes material [kg(m·s)$^{-1}$]		
Fluid	SS	SS*	Copper
H_2O	0.096	0.025	0.085
H_2O+2-EH	0.092	–	–
LiBr30	0.083	–	–
LiBr50	0.109	0.026	0.101
LiBr50+2-EH	0.104	–	–
Carrol60	0.093	0.027	0.091
Carrol60+PMC	0.083	–	–
EG	0.041	0.014	0.04

are shown in Table 4.1. The contact angle θ is considered the same on the plate and the tube with the same material. The temperature is all controlled at 20 °C.

As shown in the Figure 3.3, the dimensionless group $(1-\cos\theta)Ka^{1/3}$ is used to predict the dimensionless relation $\frac{\Gamma}{\mu}$. As shown in Table 3.1, the main variables of the equation are the fluid properties as σ, μ, ρ, and θ. The measured contact angle has repeatability around ±10% with the same sample and experimental procedure as described in [16] and Chapter 2, and surface tension σ and contact angle θ have a linear relationship.

The measured contact angle is considered the equilibrium contact angle and employed in the MWR correlation. Since the dewetting method is employed, the equilibrium contact angle instead of the advancing contact angle is used here. Also, [7], [10], and [11] confirmed that advancing contact angle could represent the wetting experiment and the equilibrium value for the dewetting process. Also, according to Lam et al. [17], the difference between advancing contact angle and receding contact angle is generally $5-20°$, and for the $(1-\cos\theta)$, the difference could be at most around 6%.

The contact angle of H_2O or LiBr$-H_2O$ on a copper base is higher than on the SS plate, according to Martinez-Urrutia et al. [18]. Considering in the real case that the MWR should be applied in the long term of use, the tubes used in the experiments have been exposed to ambient for more than one year and cleaned with alcohol. Thus the contact angle on the copper plate is lower than a new bright copper plate and more adequate for a real case. As shown in Table 4.1, H_2O on SS and copper plate has a contact angle of 70 and 60 °, correspondingly. The MWR for H_2O on SS tube is 0.096 kg(m·s)$^{-1}$ while on copper tube is 0.085 kg(m·s)$^{-1}$. Meanwhile in Morrison et al. [11], MWR for H_2O on a SS tube is 0.104 kg(m·s)$^{-1}$, in Munakata et al. [8] is 0.1 kg(m·s)$^{-1}$.

Table 3.3: Thermophysical properties of of test liquids

	Dimension	H_2O^a	EG^b	LiBr solution^c	Carrol solution^d
ρ	[kg·m^{-3}]	9.97E2	1.11E3	1.63E3	1.54E3
μ	[m^{2}s^{-1}]	8.9E-4	1.61E-2	4.28E-3	6.88E-3
C_p	[J·kg^{-1}K^{-1}]	4.18E3	2.43E3	1.94E3	2.22E3
T_in	[°C]	29	29	29	29
λ	[W·m^{-1}K^{-1}]	0.62	0.25	0.43	0.51
C_in	[−]	-	-	55%	60%
D	[m^{2}s^{-1}]	-	-	8.11E-9	8.21E-9
Re	[−]	674.2	37.3	140.1	87.2

---

[a] H_2O properties are extracted from [19]

[b] EG properties are extracted from [19]

[c] LiBr solution properties are extracted from [20]

[d] Carrol solution properties are extracted from [21]

Comparing with the correlation of Morison et al. [11], the experimental data fits well in a wide range of $(1-\cos\theta)Ka^{1/3}$, in which the relative error also decreases slightly along with the decrease of $\frac{\Gamma}{\mu}$. As the $\frac{\Gamma}{\mu}$ increases, the instability of the falling film will also increase when the $\frac{\Gamma}{\mu} > 75$. Under these circumstances, the falling film will leave a stable wavy-laminar regime and slowly turns into a transient or turbulent flow (Ishigai et al. [22]), becoming a steady dry patch more challenging to capture. High viscosity ($> 0.1\mathrm{Pa}\cdot\mathrm{s}^{-1}$) has not been taken into consideration due to the typical values of the working pairs considered in absorption systems since high viscosity will reduce the heat and mass transfer rate in the absorption system ([5]).

Moreover, according to the equations in Table 3.1, low surface tension will lead to a low MWR for the same liquid. LiBr−H_2O mixed with 2−EH and Carrol−H_2O with PMC are used in the surface tension measurement part; the surfactants are added in an amount several times higher than the Critical Micellar Concentration (CMC) to ensure its concentration. From Figure 3.3, we could conclude that though the Ka decreases with the presence of the surfactants, the $\frac{\Gamma}{\mu}$ also decreases, but not as much as predicted with the correlation. Furthermore, the observed dry patch may not maintain stability during the experiment compared with the solution without surfactant. Though the concentration of surfactants used here is around 1000 ppm, the dynamic surface tension may differ with the measured one in the sample since the distribution of surfactants may not remain uniform on the interface in a stream.

As shown in Table 3.2, with surfactant 2−EH, the MWR of H_2O on SS tube reduced slightly, from 0.096 to 0.092 $kg(m \cdot s)^{-1}$ on average. In terms of LiBr 50wt% and Carrol 60wt% solution with surfactant 2−EH, PMC, respectively, the MWR decrease from 0.109 to 0.101 (LiBr) and 0.093 to 0.091 (Carrol) $kg(m \cdot s)^{-1}$ on average. According to Table 3.1, the MWR most likely has a relationship with the surface tension σ with an exponent of 0.6−0.764. Subsequently, in the experiment with LiBr 50wt%, σ decreases 40−60%, while the MWR only decreases around 20%.

On the other hand, though for pure fluid contact angle has a linear relationship with surface tension, as explained in Chapter 2, the contact angle will not change linearly for the mixture of fluid + surfactant according to the experimental tests. More precisely, the concentration of the surfactant for the sample is already low (≤1000 ppm), hence there is no guarantee for the concentration of the surfactant in the sample for the contact angle (≤5μL), so it has not been possible to perform this measurement. Therefore, here in the calculation of $\cos\theta$, the contact angle of the liquid is considered the same as the liquid without surfactants.

At the same time, the contact angle after the hydrophilic coating could not be measured precisely and varies between 10−35°, which is much lower than the original material. Here the mean value of θ is used. The data of liquid on the hydrophilic SS also agree with the correlation. As shown in Table 3.2, the MWR of H_2O on the SS tube has decreased from 0.096 to 0.025 $kg(m \cdot s)^{-1}$. LiBr−H_2O and Carrol−H_2O have reached a similar value with the hydrophilic coating SS tube.

Liquid viscosity is a relevant parameter that distinguishes the correlations from the different authors. In this work, the correlation from Morison et al. [11] is used to check its effect of surface tension and contact angle on MWR. The viscosity is calculated according to several references depending on the liquid type. For the liquids studied, this effect is relevant compared with other thermophysical properties, as viscosity varies significantly. We consider that the viscosity of each tested fluid is well investigated in other references, so the correlations for its calculation have been considered enough reliability. In the experiments, the temperature is maintained constant in each test. The μ could change from 8.9×10^{-4} (H_2O) to 1.6×10^{-2} (EG) $Pa \cdot s^{-1}$, i. e. it increases 18 times. Meanwhile, the σ, ρ, and θ only could change in a limited range. For σ is $35-90$ $mN \cdot m^{-1}$, for (1-$\cos\theta$) is in the range of $0.13-1$ and density changes within $997-1550$ $kg \cdot m^{-3}$. Hence, the exponent of μ (0.2) in the reference [6], [7], [9], [10] should decrease, since high viscosity tends to result in a low Re flow and thus have a slightly negative effect on the MWR.

Low surface tension and contact angle will generally lead to a lower MWR (without surfactants), while viscosity will generally lead to a lower Re. Reducing the contact angle is the most effective way to acquire a lower MWR.

NOMENCLATURE

Name	**Description**
C	Concentration [−]
D	Mass diffusivity coefficient [$\mathrm{m}^2 \cdot \mathrm{s}^{-1}$]
g	Acceleration of gravity [$\mathrm{m} \cdot \mathrm{s}^{-2}$]
Ka	Kapiza number $\left(\frac{\sigma\rho^3}{\mu^4 g}\right)^{\frac{1}{3}}$
Re	Reynolds number $\frac{4\Gamma}{\mu}$
T	Temperature[°C]
Greek letter	**Description**
Γ	Mass flow rate per length [$\mathrm{kg}(\mathrm{m} \cdot \mathrm{s})^{-1}$]
δ	Mean film thickness [m]
Δ	Dimensionless film thickness [-]
θ	Contact angle [$\circ$]
λ	Thermal conductivity [$\mathrm{Wm}^{-1}\mathrm{K}^{-1}$]
μ	Dynamic viscosity [$\mathrm{Pa} \cdot \mathrm{s}^{-1}$]
ρ	Density [$\mathrm{kg} \cdot \mathrm{m}^{-3}$]
σ	Surface tension [mN·m]
Abbreviation	**Description**
CMC	Critical micellar concentration
EG	Ethylene glycol
MLFT	Minimum liquid film thickness
MWR	Minimum wetting rate
MTE	Minimum total energy
PMC	Phenylmethylcarbinol, 1−Phenylethanol
SS	Stainless steel
SS*	Hydrophilic coated stainless steel
VLE	Vapor-liquid equilibrium
wt	Weight ratio
Subscripts & Superscripts	**Description**
in	inlet
min	Minimum

References

[1] J. Castro, A. Oliva, C. D. Pérez-Segarra, J. Cadafalch, Evaluation of a small capacity, hot water driven, air-cooled H2O-LiBr absorption machine, HVAC and R Research 13 (1) (2007) 59–75. `doi:10.1080/10789669.2007.10390944`.

[2] J. Castro, A. Oliva, C. D. Perez-Segarra, C. Oliet, Modelling of the heat exchangers of a small capacity, hot water driven, air-cooled H2O-LiBr absorption cooling machine, International Journal of Refrigeration 31 (1) (2008) 75–86. `doi:10.1016/j.ijrefrig.2007.05.019`.

[3] J. Castro, C. Oliet, I. Rodríguez, A. Oliva, Comparison of the performance of falling film and bubble absorbers for air-cooled absorption systems, International Journal of Thermal Sciences 48 (2009) 1355–1366. `doi:10.1016/j.ijthermalsci.2008.11.021`.

[4] J. Castro, J. Farnós, G. Papakokkinos, J. Zheng, C. Oliet, Transient model for the development of an air-cooled LiBr-H2O absorption chiller based on heat and mass transfer empirical correlations, International Journal of Refrigeration 120 (2020) 406–419. `doi:10.1016/j.ijrefrig.2020.08.030`.

[5] J. Zheng, J. Castro, A. Oliva, C. Oliet, Energy and exergy analysis of an absorption system with working pairs LiBr-H2O and Carrol-H2O at applications of cooling and heating, International Journal of Refrigeration 132 (September) (2021) 156–171. `doi:10.1016/j.ijrefrig.2021.09.011`.

[6] D. E. Hartley, W. Murgatroyd, Criteria for the break-up of thin liquid layers flowing isothermally over solid surfaces, International Journal of Heat and Mass Transfer 7 (1964) 1003–1015. `doi:10.1016/j.ces.2014.01.034`.

[7] A. B. Ponter, G. A. Davies, T. K. Ross, P. G. Thornley, The influence of mass transfer on liquid film breakdown, International Journal of Heat and Mass Transfer 10 (3) (1967) 349–352. `doi:10.1016/0017-9310(67)90151-2`.

[8] T. Munakata, K. Watanabe, K. Miyashita, Minimum wetting rate on wetted-wall column, Journal of Chemical Engineering of Japan 8 (6) (1975) 440–444.

[9] A. Doniec, Flow of a laminar liquid film down a vertical surface, Chemical Engineering Science 43 (4) (1988) 847–854. `doi:10.1016/0009-2509(88)80080-0`.

[10] M. S. El-Genk, H. H. Saber, Minimum thickness of a flowing down liquid film on a vertical surface, International Journal of Heat and Mass Transfer 44 (15) (2001) 2809–2825. `doi:10.1016/S0017-9310(00)00326-4`.

[11] K. R. Morison, Q. A. G. Worth, N. P. O'Dea, Minimum wetting and distribution rates in falling film evaporators, Food and Bioproducts Processing 84 (4 C) (2006) 302–310. `doi:10.1205/fbp06031`.

[12] D. E. Hartley, W. Murgatroyd, Criteria for the break-up of thin liquid layers flowing isothermally over solid surfaces, International Journal of Heat and Mass Transfer 7 (9) (1964) 1003–1015.

[13] J. Mikielewicz, J. R. Moszynski, Minimum Thickness of a Liquid Film Flowing Vertically Down a Solid Surface, International Journal of Heat and Mass Transfer 19 (7) (1976) 771–776. `doi:10.1016/0017-9310(76)90130-7`.

[14] Y. Lu, F. Stehmann, S. Yuan, S. Scholl, Y. Lu, F. Stehmann, S. Yuan, S. Scholl, Falling film on a vertical flat plate – Influence of liquid distribution and fluid properties on wetting behavior, Applied Thermal Engineering 123 (2017) 1386–1395. `doi:10.1016/j.applthermaleng.2017.05.110`.

[15] L. Ye, Y. Zhang, C. Song, Y. Li, B. Jiang, A simple sol-gel method to prepare superhydrophilic silica coatings, Materials Letters 188 (2017) 316–318. `doi:10.1016/j.matlet.2016.09.043`.

[16] J. Zheng, J. Castro, C. Oliet, A. Oliva, Surface tension and contact angle measurement of LiBr and Carrol solution, in: International sorption Heat pump Congress, 2021, pp. 74—-78.

[17] C. N. C. Lam, R. Wu, D. Li, M. L. Hair, A. W. Neumann, Study of the advancing and receding contact, Advances in Colloid and Interface Science 96 (2002) 169–191.

[18] A. Martinez-Urrutia, P. Fernandez de Arroiabe, M. Ramirez, M. Martinez-Agirre, M. Mounir Bou-Ali, Contact angle measurement for LiBr aqueous solutions on different surface materials used in absorption systems, International Journal of Refrigeration 95 (2018) 182–188. `doi:10.1016/j.ijrefrig.2018.05.041`.

[19] A.˜Kramida, Yu.˜Ralchenko, J.˜Reader, No Title, NIST Atomic Spectra Database (ver. 5.7.1), [Online]. Available: {\tt{https://physics.nist.gov/asd}} [2015, April 16]. National Institute of Standards and Technology, Gaithersburg, MD. (2019).

[20] L. McNeely, Thermodynamic properties of aqueous solutions of lithium bromide, ASHRAE Transactions 85 (1) (1979) 413–434.

[21] W. Biermann, Proprties of the Carrol system and a machine design for solar-powered, air-cooled, absorption space cooling. Phase I and Phase II. Final report, September 1977-March 1979, Tech. rep., Carrier Corp., Syracuse, NY (USA). Energy Systems Div. (1981).

[22] S. Ishigai, S. Nakanisi, T. Koizumi, Z. Oyabu, Hydrodynamics and Heat Transfer of Vertical Falling Liquid Films, Chemical Pharmaceutical Bulletin 17 (11) (1994) 1460–1462.

4

Vertical falling film simulation and experimental validation

Abstract

A smooth laminar 2-D theoretical model of the vertical falling film was built with an in-house code based on C++ and compared with analytical results. The model was developed for the vertical liquid falling film with and without absorption, considering the thermophysical properties enhancement with nanoparticles. The working pairs of absorption studied are LiBr-H_2O and Carrol-H_2O. Furthermore, an experimental setup is commissioned to validate the pure heat transfer process. Different methods are employed to measure the temperature of the falling film. With the low flow rate of the liquid, the simulation and experimental results match well with various liquids such as water, EG, LiBr solution, and Carrol solution. However, when the flow rate increases, the discrepancy also increases due to the limit of smooth film theory. Additionally, experimental validation of the pure heat transfer problem with nanofluid shows some differences between the model and experiment. In general, the temperature distribution in pure heat transfer problems could be well predicted by the simulation or analytical results along with the falling film. Considering the absorption in the falling film (combined heat and mass transfer), the heat transfer process will significantly change in the vertical direction since the absorption enthalpy is also introduced to the liquid.

4.1 Introduction of vertical liquid falling film

Falling liquid film heat exchangers are widely employed in various industrial procedures, such as refrigeration, separation, distillation, etc. In order to model the falling liquid films, the smooth laminar film hypothesis is usually applied due to the simplification in the simulation and the possibility of employing analytical solutions for some situations. For other fluid regimes, additional effects should be considered, e. g., waves, recirculations, turbulence, etc. Ishigai et al. [1] proposed a fluid-dynamic classification of the vertical falling film:

1. Laminar flow $0 \le Re \le 1.88(Ka^{0.3})$
2. First transient $1.88(Ka^{0.3}) \le Re \le 8.8(Ka^{0.3})$
3. Stable wavy-laminar $8.8(Ka^{0.3}) \le Re \le 300$
4. Second transient $300 \le Re \le 1600$
5. Fully turbulent $1600 \le Re$

Where the $Re = 4\Gamma/\mu$ and $Ka = \left(\frac{\sigma\rho^3}{\mu^4 g}\right)^{\frac{1}{3}}$. And the film regime was demonstrated by Yue et al. [2] by Figure 4.1. Which indices that the smooth laminar falling film only exits in a very low Re number for water. And as shown in Table 4.1 in Chapter 3, the corresponding Re for water, EG, LiBr and Carrol solution are 674.2, 37.3, 140.1, 87.2, respectively.

Enormous effort for the investigation of heat and mass transport in falling film absorption has been realized by developing analytical solutions, numerical simulations, and experiments. Nakoryakov and Grigoryeva [3] did a detailed analytical solution of the smooth laminar falling film model with the series expansion method of solutions to eigenfunctions. Besides, Meyer and Ziegler [4], Turkyilmazoglu [5] also solved the analytical absorption falling film model with similar hypotheses at various conditions with Fourier analysis and Laplace Transform. Zhang et al. [6] showed the analytical solution of the vertical falling film without absorption and validated the results with experimental results.

Otherwise, a numerical model can be conceived in many detail levels. On the one hand, empirical information of heat and mass transfer coefficients according to the correlations form [7, 8] can be used to develop a 1D step-by-step procedure. On the other hand, a more detailed model based on the simplification of the governing equations can also be defined for solving the simultaneous heat and mass transfer in the falling film absorption process. An example of this type of modelization is Yang et al. [9], who investigated the smooth laminar absorption falling film process of LiBr-H_2O and LiCl-H_2O and compared with their experimental results, in which there is 5% of air

Re=127.23
Re=466.5
Re=1000.85
Re=2014.43
Re=2516.27
Re=3498.75
Re=4481.22
Re=4877.04

Figure 4.1: Vertical falling film photograph, from Yue el al. [2]

in the system. There was good agreement between the experimental data and the numerical data in the Re range $60 < Re < 200$. And later, in results of Yang et al. [10], Yang and Derming compared the smooth film simulation results with a wavy film model, and the results indicated that film waves have a decisive effect on the absorption rates. The mass transfer coefficient could be two times higher in a wavy film than in a smooth film. Yuksel and Schlunder [11] investigated turbulent falling film heat and mass transfer in numerical models and experiments. In their experiments, the absorption rate and the surface temperature were measured using an infrared sensor (8-20 μm), considering that water is opaque to infrared, and water vapour is translucent. Patnaik et al. [12] did a computational model of vertical falling film of aqueous LiBr with empirical correlations of heat and mass transfer and validate the numerical modelling with the experiment set-up. Lamourelle and Sandall [13] investigated the gas absorption into a turbulent liquid falling film with numerical method and experiment, and the results showed that the mass transfer coefficient is proportional to $\sqrt{D}$ (where D is mass difussivity). Garcia-Rivera et al. [14] studied the falling film with simulation and experiments considering the presence of mist flow of the vapor. In a later work, the research was extended in Garcia-Rivera et al. [15] to study the effect of non-absorbable gas. Brauner et al. [16] show the turbulent wavy flow models for intermediate and high Re. Miller investigated more details in the LiBr falling film in his dissertation [17]. The thermographic phosphors method was introduced to measure the film interface temperature. Medrano et al. [18] experimented inside of a tube with a falling film which is more realistic.

In terms of the performance enhancement methods, concerning pure experimental research, Miller and Perez-Blanco [19] did an experiment about vertical falling film LiBr with advanced surfaces. Their results showed that a pin-fin tube with 6.4 mm pitch absorbed 225% more mass than a smooth tube, while a grooved tube was 175% more. Moreover, modifications to the working pairs are also employed to improve the heat and mass transfer performance. Zhang et al. [20] used various types of tubes and surfactants to investigate their effect on the heat and mass transfer of LiBr solution, the results demonstrate that the surfactant 2-Ethyl-1-hexanol(2-EH) could improve 2.1 and 4.1 times heat and mass transfer performance while the value for 1-Octanol is 3.5 and 1.5, correspondingly. And the tube surface affects less, the floral finned tube has a 2 times higher mass transfer while the heat transfer will not overcome it on the plain tube when the tube number is less than 10. Apart from surfactant, nanofluid could also be employed to enhance the heat and mass transfer of the falling film. Unlike surfactant affects surface tension and the Marangoni effect, the nanofluid will change the thermodynamic properties of the working pairs, especially the thermal conductivity. Nanofluid is a liquid with the suspension of nanoparticles whose diameter is within 1-100 nm, and they are generally not soluble in the liquid. Nanoparticles typically used have much higher thermal conductivity than the substrate liquid, so they have the highest potential to grow in the mixture. The enhancement of the thermal conductivity of nanofluid to the base fluid is generally related to the volume fraction of the nanoparticle. Many authors measured the thermal conductivity of nanofluid as reviewed in Chapter 2.

With the enhanced thermophysical properties, nanofluid could increase the heat and mass transfer coefficient in many applications like the falling film. Gao et al. [21] investigated the effect of CuO nanoparticles in LiBr-H_2O falling film absorption using a numerical model. In this work, they investigated the effect of nanofluid on heat transfer in the falling film compared with an analytical solution. Besides, experimental data were used to validate the results by measuring the liquid interface and bulk temperatures. The falling film temperature distribution could also be obtained. The improvement was more significant at the high inlet temperature of the liquid solution and when the concentration of liquid solution at the inlet was low. Zhang et al. [22] studied the influence of nanofluid with Cu, Al_2O_3, and CNT to the falling film absorption. They found that the small nanoparticle's size and larger mass fraction lead to a better effective absorption ratio, and the absorption rate could increase by 125%.

In this chapter, numerical simulation is carried out and compared with an analytical solution of heat transfer of a smooth laminar vertical falling film. Moreover, the results are also compared with experimental results. The temperature distribution of the vertical falling film is analyzed under different conditions with different liquids, water, EG, and LiBr solutions. In terms of nanofluid, these three liquids are turned into nanofluid with Al_2O_3 particles of 50 nm average diameters. Once the nanofluid is made, experiments are carried out and compared with base fluid. Finally, the effect of nanofluid on an absorption process of LiBr solution is investigated numerically with the same model.

4.2 Numerical modelling and implementation of the vertical falling film problem

In this section, the model used for the simulation of the heat and mass transfer process in falling film absorption is described in detail. A smooth laminar falling film is employed, which is a simplification of the actual falling film flows with a free liquid surface. As

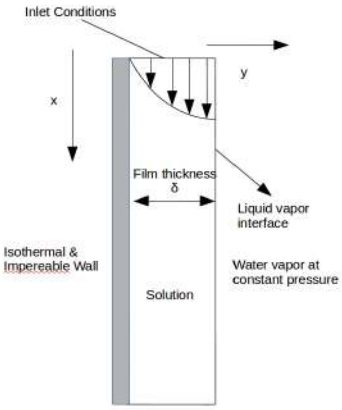

Sketch of a smooth laminar falling film

Figure 4.2

shown in Figure 4.2, liquid with mass flow rate at Γ travels along with a vertical wall driven by gravity. The following assumptions are made:

- The flow is a fully developed smooth laminar flow
- The fluid properties are constant
- Vapor mass transfer effect is taken into account only for absorption processes
- Diffusion thermal effects and diffusion in flow direction are negligible
- Instantaneous phase equilibrium at the interface
- Constant pressure and film thickness throughout the film
- The shear stress at liquid−vapour interface is negligible
- The film thickness δ is assumed constant
- The wall is isothermal and impermeable

With the hypothesis above, the general energy and specie equations could be simplified to Equations 4.1–4.2 as the governing equations of the absorption falling film.

$$u\frac{\partial T}{\partial x} = \kappa\frac{\partial^2 T}{\partial y^2} \tag{4.1}$$

$$u\frac{\partial C}{\partial x} = D\frac{\partial^2 C}{\partial y^2} \tag{4.2}$$

If there is vapour absorption, a thermodynamic equilibrium condition is assumed at the corresponding pressure at the interface as shown in Equation 4.3. In contrast, an adiabatic condition is employed if the process is pure heat transfer, as shown in Equation 4.4.

$$\begin{aligned} -\lambda\frac{\partial T}{\partial y}\bigg|_{y=\delta} &= \rho D\frac{\partial C}{\partial y}Ha\bigg|_{y=\delta} \\ T\bigg|_{x=0} &= T_{\text{in}}, C\bigg|_{x=0} = C_{\text{in}} \\ T\bigg|_{y=0} &= T_{\text{w}}, \frac{\partial C}{\partial x}\bigg|_{y=0} = 0 \end{aligned} \tag{4.3}$$

$$\begin{aligned} -\lambda\frac{\partial T}{\partial y}\bigg|_{y=\delta} &= 0 \\ T\bigg|_{x=0} &= T_{\text{in}}, T\bigg|_{y=0} = T_{\text{w}} \end{aligned} \tag{4.4}$$

For the simulation, the thermodynamic equilibrium is described as Equation 4.3 for comparison with other authors for the analytical solutions. However, to achieve a higher accuracy in the validation of the experimental results, the equation should be modified as 4.5 to take into account the effect of a semipermeable interface (no LiBr absorption), as explained in [23].

$$-\lambda\frac{\partial T}{\partial y}\bigg|_{y=\delta} = \rho D\frac{\partial C}{C\partial y}Ha\bigg|_{y=\delta} \tag{4.5}$$

The inlet velocity is set as fully developed laminar flow velocity, as shown in Equation 4.6

$$u = \bar{u}\left[1-\left(1-\frac{y}{\delta}\right)^2\right] \tag{4.6}$$

where $\bar{u} = \frac{\rho g}{2\mu}\delta^2$, μ, ρ, g represent the dynamic viscosity, liquid density, the gravitational acceleration and the average film thickness, respectively. The average film thickness is $\delta = \left(\frac{3\mu\Gamma}{\rho^2 g}\right)^{\frac{1}{3}}$, where Γ represents the inlet mass flow with dimension $\text{kg}\cdot\text{m}^{-1}\cdot\text{s}^{-1}$.

The dimensionless procedure is the same as [4]. With dimensionless process, Equation 4.1 could be turned into Equation 4.7 −4.9:

$$\left[1-(1-Y)^2\right]\frac{\partial\Theta}{\partial X}=\frac{\partial^2\Theta}{\partial Y^2} \tag{4.7}$$

$$\left[1-(1-Y)^2\right]\frac{\partial\Upsilon}{\partial X}=\frac{1}{Le}\frac{\partial^2\Upsilon}{\partial Y^2} \tag{4.8}$$

$$\left.\frac{\partial\Theta}{\partial Y}\right|_{Y=1}=\frac{1}{\overline{St}\cdot Le}\cdot\left.\frac{\partial\Upsilon}{\partial Y}\right|_{Y=1} \tag{4.9}$$

where $X=\frac{\kappa x}{\bar{u}\delta^2}$, $Y=\frac{y}{\delta}$, $\Theta=\frac{T(x,y)-T_{\text{in}}}{T_{\text{w}}-T_{\text{in}}}$,$\Upsilon=\frac{C(x,y)-C_{\text{in}}}{C_{\text{w}}-C_{\text{in}}}$,$Le$ is Lewis number, $Le=\frac{\kappa}{D}$, $\overline{St}$ is modified Stefan number $\overline{St}=\frac{C_{\text{in}}\cdot(T_{\text{eq}}-T_{\text{in}})}{\Delta h_{\text{abs}}\cdot(C_{\text{eq}}-C_{\text{in}})}$, κ is thermal diffusivity, C_{p} h_{abs} represents the specific heat capacity, and absorption enthalpy.

Besides the analytical solutions, the PDEs of the falling film with or without absorption could be solved numerically. An in-house code based on C++ is made to solve the falling film temperature and concentration distribution in both conditions. The finite volume method is used for the discretization, and hyperbolic mesh and TDMA solver is used to solve the equations. If the absorption is considered, the Secant method is used to solve the boundary condition on the interface.

4.3 Heat transfer in vertical falling film

4.3.1 Numerical simulation model verification and first validation

Analytical solution is proposed in Zhang et al. [6] as Equation 4.10 for the pure heat transfer case has been chosen as reference for model verification.

$$\Lambda=\frac{e^{(-X-\frac{1}{2}Y^2+Y)}-e^{\frac{1}{2}}}{e^{-1}-e^{\frac{1}{2}}} \tag{4.10}$$

Besides, the correlation of the heat transfer coefficient for falling film flow proposed by Seban and Faghri [7] (see equation 4.11) has been implemented in a 1D code to validate the 2D numerical code.

$$\frac{\overline{\alpha}\delta}{\lambda}=0.029\left(\frac{4\Gamma}{\mu}\right)^{0.53}\left(\frac{\nu}{\kappa}\right)^{0.344} \tag{4.11}$$

where $\overline{\alpha}$ is the average heat transfer coefficient, δ is the film thickness, Γ is the mass flow rate, μ is the dynamic viscosity, ν is the kinetic viscosity and κ is the thermal diffusivity.

The energy balance for the liquid film is in Equation 4.12 for each control volume of the 1D discretization.

$$\overline{\alpha} A \Delta T_\mathrm{m} = \Gamma C_\mathrm{p}(T_\mathrm{in} - T_\mathrm{out}) \tag{4.12}$$

Where the logarithmic mean temperature difference $\Delta T_\mathrm{m} = \frac{T_\mathrm{in} - T_\mathrm{out}}{\ln\left(\frac{T_\mathrm{in} - T_\mathrm{w}}{T_\mathrm{out} - T_\mathrm{w}}\right)}$, A is the contact area of the liquid film, and $T_\mathrm{in}, T_\mathrm{out}$ represents the start and end point of the calculating area of the film.

With Equations 4.11 and 4.12, the film bulk temperature distribution along with the tube direction could be obtained.

The numerical and analytical results for the interface temperature of a falling film of water and EG are shown in Figure 4.3, and the bulk temperature distribution is shown in Figure 4.4. The mesh sensitivity analysis was carried out and the final mesh employed is 100*200. The results in Figure 4.3 show that the numerical simulations and the analytical agree well with each other of the prediction with interface temperature distribution of the vertical falling film. Meanwhile, in terms of the bulk temperature as shown in Figure 4.4, the temperature distribution doesn't agree with each other but will finally approach each other when the tube length increase. The identified reasons for the deviation could be: i)different inlet area of the falling film; ii) the empirical correlation provides an average coefficient, while the simulation determines the local heat transfer by considering flow development/distribution aspects.

4.3.2 Experimental results of heat transfer in vertical falling film

The experimental set-up employed here is shown in Figure 7.1. The temperature was measured by multiple infrared temperature sensors. The experimental results are shown in Figure 4.6. The experimental results have an uncertainty of 8.3%, the details are listed in the Appendix A.1. As shown in Figure 4.6, the experimental results of the temperature distribution match the simulation results at a relatively low mass flow rate, and for the EG fluid, the repeatability is higher than water since it is more viscous. In terms of the tube wall temperature, by modifying the mass flow rate of the secondary circuit, the inlet-outlet of coolant temperature difference is within 0.2 °C, hence the isotherm wall is considered accurate. Moreover, to assure the experiment is a pure heat transfer process, if binary mixture is employed in the experiment, the electrical conductivity will also be measured to check the density of the inlet and outlet solution as explained in Chapter 2.

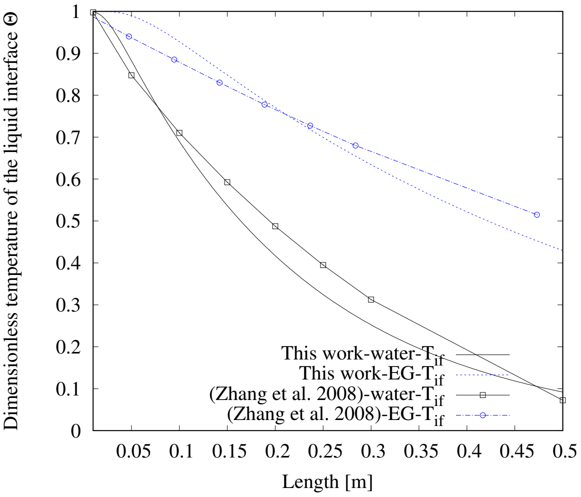

Figure 4.3: Dimensionless temperature (Θ) distribution at the interface from analytical solutions and numerical simulations. The Γ is set as 0.18 for water and 0.10 for EG. The inlet liquid is set as 29°C and the wall is considered isotherm at 25°C.

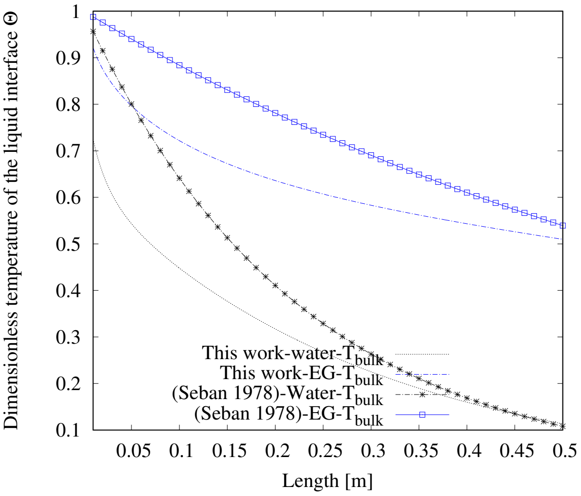

Figure 4.4: Dimensionless temperature (Θ) distribution of the solutions film calculated with correlation from [7] and numerical simulations. The Γ is set as 0.18 for water and 0.10 for EG. The inlet liquid is set as 29°C and the wall is considered isotherm at 25°C.

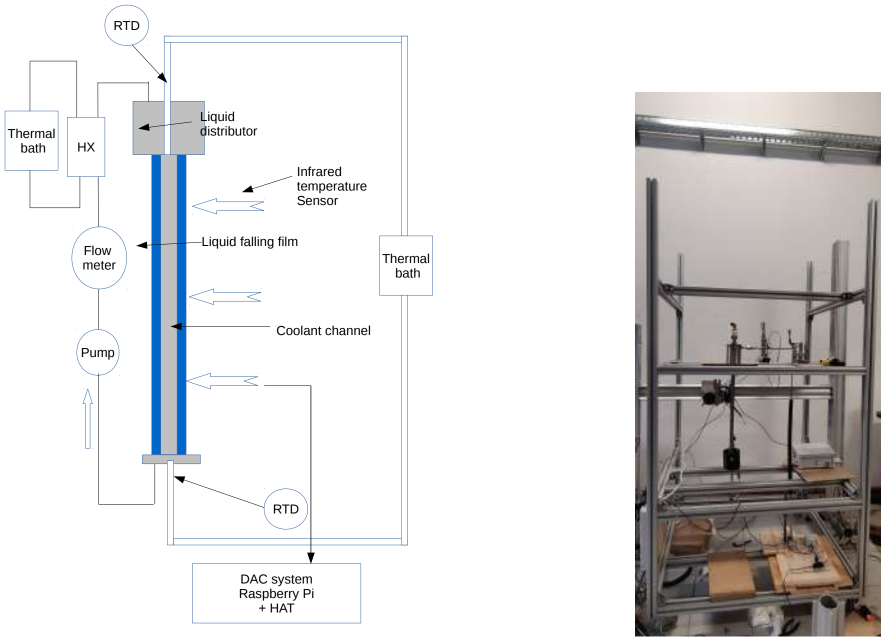

(a) Sketch of the test rig (b) Foto of the experimental setup

Figure 4.5: Vertical falling film temperature measurement experimental setup

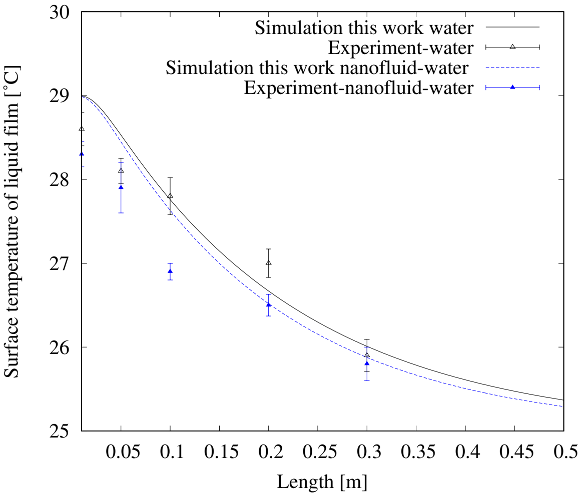

Figure 4.6: Experimental results of interfacial temperatures of liquid falling film (water and water nanofluid) compared with numerical results, the film properties of pure liquid are shown in Table 4.1. The Γ for the water is 0.12 kg·m^{-1}·s^{-1}, and the nanofluid was made with 0.5% Al_2O_3, with 1% of dispersant E414, the properties of nanofluid were reported in Chapter 2.

When the nanofluid is considered, Al_2O_3 of the diameter of 50-80nm was employed to make nanofluid with a two-step method. Also, to stabilize the nanoparticle in the liquid, dispersant (E414) was used as recommended in Wang et al. [24]. After preparation, the nanofluid will be stored for at least one week before experiments to avoid unstable sediment. Considering the other information on the heat transfer problem, the simulation was carried out with the comparison of fluid and nanofluid with 0.5% Al_2O_3. The temperature distribution of the vertical falling film with nanofluid is shown in Figure 4.7. Compared with the results of base fluid as shown in Figure 4.6, the experimental results of the nanofluid don't agree well with the simulation results and the temperature decreases faster than predicted. Several reasons may cause the discrepancy. Firstly, though the properties change caused by nanoparticles are reported many times by other references, there are also discrepancies between authors. Secondly, besides the thermal conductivity, viscosity and specific heat capacity, the surface tension may also change with the nanofluid and as declared before, low surface tension could also strengthen the heat transfer phenomena in the falling film. Besides, the dispersant may also affect all the properties of the fluid and is not considered in the simulation. Since dispersant is necessary for the durability of nanofluid, more work focusing on the thermodynamic properties should be carried out to find a suitable model for the heat transfer in the falling film.

4.3.3 Simulation studies of the heat transfer in the vertical falling film considering nanofluid influence

Considering the other information on the heat transfer problem, the simulation was carried out with the comparison of fluid and nanofluid with 0.5% Al_2O_3. The results in Figure 4.8 show that the temperature profile depends on the fluid type and how the nanofluid has an influence increasing the temperature level.

Figure 4.9 depicts the heat transfer coefficient distribution for the same cases as the temperature profile in terms of the effect of nanofluid. Depending on the properties, though the mass flow rate is at the same level, the Re,Ka number could vary a lot, also the heat transfer coefficient. In Figure 4.9, when the mass flow rate starts from corresponding MWR, the average heat transfer coefficient will decrease and then increase for basefluid and nanofluid. At a certain temperature difference between the isothermal wall and inlet liquid, the outlet temperature of the film against the outlet temperature is shown in Figure 4.10. The outlet temperature has a logarithmic relationship with mass flow rate which indicates the heat transfer coefficient in Figure 4.9. The evolution

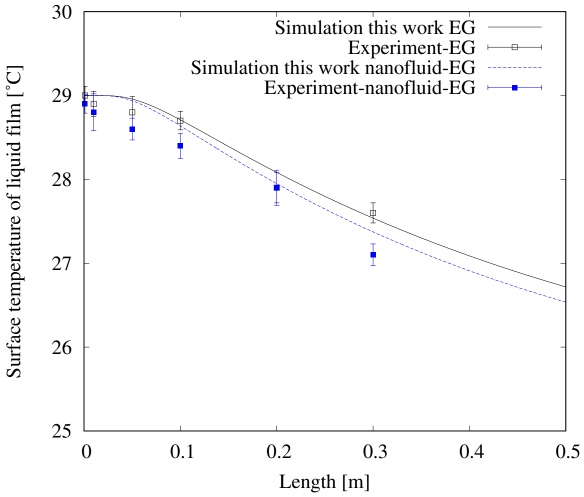

Figure 4.7: Experimental results of interfacial temperatures of nanofluid falling film (EG and EG nanofluid) compared with numerical results, the film properties of pure liquid are shown in Table 4.1. The Γ for EG is 0.1 kg·m^{-1}·s^{-1}. And the nanofluid was made with 0.5% Al_2O_3, with 1% of dispersant E414, the properties of nanofluid were reported in Chapter 2.

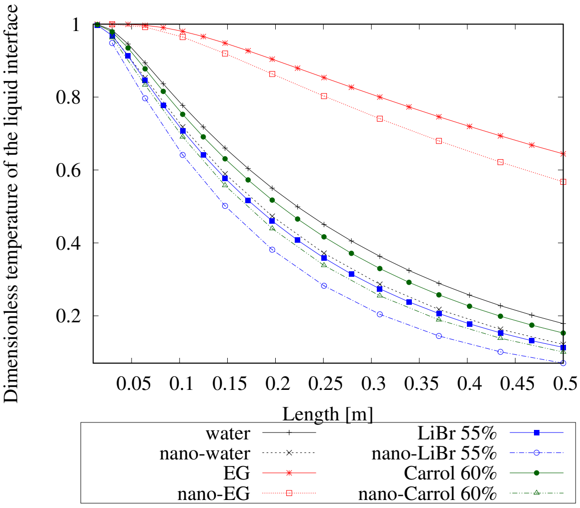

Figure 4.8: Dimensionless temperature (Θ) distribution at the interface from different fluids in numerical simulations. The Γ is set as 0.15 $\mathrm{kg \cdot m^{-1} \cdot s^{-1}}$ for all the fluids. The inlet liquid is set as 29°C and the wall is considered isotherm at 25°C. The nanofluid of the corresponding fluid is set with Al_2O_3 at volume concentration ϕ=1%.

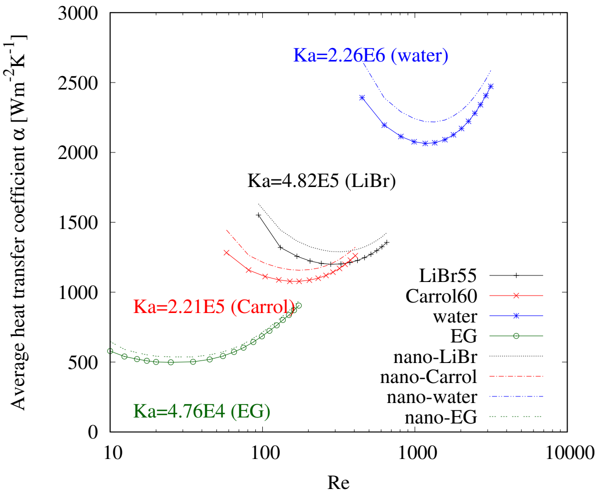

Figure 4.9: Numerical simulation results of heat transfer coefficient of the falling film with various fluids, the mass flowrate starts from the corresponding MWR for each fluid as explained in Chapter 3 to 0.6 kg· $m^{-1}s^{-1}$ The nanofluid of the corresponding fluid is set with Al_2O_3 at volume concentration ϕ=0.5%.

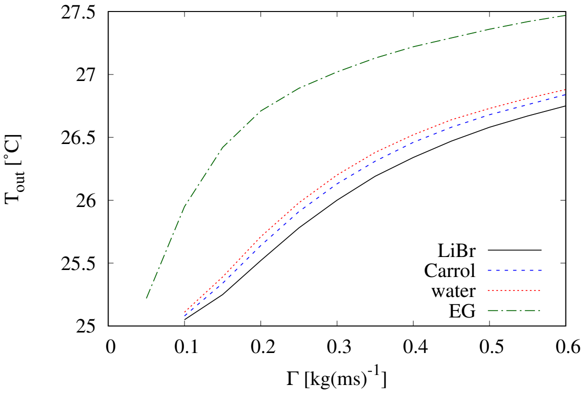

Figure 4.10: Numerical simulation results of outlet film temperature against the mass flow rate. The isothermal wall is at temperature 25 °C and the liquid inlet temperature is 29°.

progress of heat transfer coefficient were also observed experimentally by [25], [11],

4.4 Combined heat and mass transfer in vertical falling film with LiBr-H_2O and Carrol-H_2O

When the mass transfer is considered in the falling film, the system is under vacuum conditions and near the thermodynamic equilibrium pressure. The subcooled solution will enter the low-pressure place and be cooled down by the isothermal wall, with the decrease of the film temperature, the equilibrium concentration will also decrease and has the potential to absorb water vapor to maintain equilibrium at the surface, and the water will be transport from the surface to the bulk. In this section, different working pairs are used here to investigate the absorption performance of the falling film, also considering the influence of nanoparticles.

4.4.1 Model validation

The 2D numerical model is compared with experimental data from [14], [18], [19], [29] and smooth laminar theory as shown in Figure 4.11, 4.12.

The comparison between experimental data and smooth theory simulations between Re and absorption mass results are shown in Figure 4.11. As demonstrated in the figure,

Table 4.1: Thermophysical properties of of test liquids

	Dimension	Water[a]	EG[b]	LiBr solution[c]	Carrol solution[d]
ρ	[kg·m^{-3}]	9.97E2	1.11E3	1.63E3	1.54E3
μ	[m^{2}s^{-1}]	8.9E-4	1.61E-2	4.28E-3	6.88E-3
C_p	[J·kg^{-1}K^{-1}]	4.18E3	2.43E3	1.94E3	2.22E3
T_in	[°C]	29	29	29	29
λ	[W·m^{-1}K^{-1}]	0.62	0.25	0.43	0.51
C_in	[−]	-	-	55%	60%
D	[m^{2}s^{-1}]	-	-	8.11E-9	8.21E-9
Re	[−]	674.2	37.3	140.1	87.2
Le	[−]	-	-	27.3	29.4

---

[a] Water properties are extracted from [26]
[b] EG properties are extracted from [26]
[c] LiBr solution properties are extracted from [27]
[d] Carrol solution properties are extracted from [28]

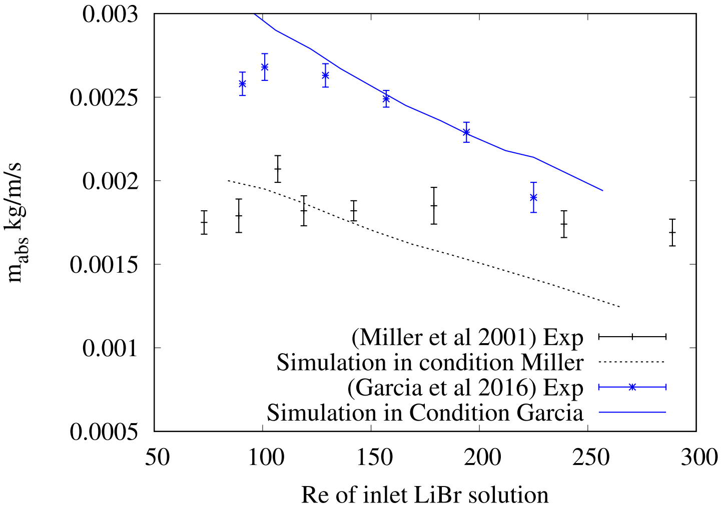

Figure 4.11: Comparison of simulation results from [14], [19] and simulations in this work. Inlet solution conditions in [19], P = 1333 Pa, $C_{\mathrm{LiBr,in}}$=62% L_{tube}=1.5m. In [14], $C_{\mathrm{LiBr,in}}$=60.4% and the rest condition remains the same.

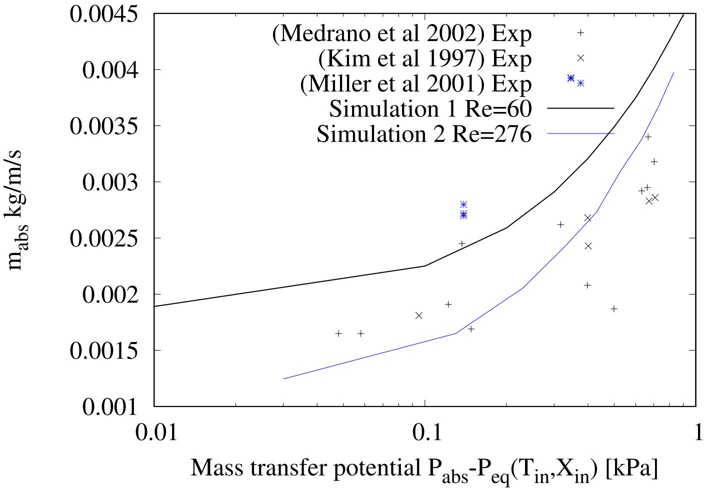

Figure 4.12: Comparison of simulation results from [18], [19], [29] and simulations in this work. Simulation 1 was carried out with similar operation conditions in [29], [18], $C_{\mathrm{LiBr,in}} = 60\%$, $T_{\mathrm{in}} = 44°\mathrm{C}$, $T_{\mathrm{w}} = 35°\mathrm{C}$, and $Re = 60$. In simulation 2, the operation conditions is the same as in Miller et al. [19] where $C_{\mathrm{LiBr,in}} = 62.3\%$, $T_{\mathrm{in}} = 54°\mathrm{C}$, $T_{\mathrm{w}} = 48°\mathrm{C}$ and $Re = 276$.

the absorbed vapor mass rate agrees with the experimental data at Re number range of 80-200, also, the inlet solution are near thermodynamic equilibrium. Besides, the pressure of the absorber will also affect the performance. The mass absorbed at different pressure is shown in Figure 4.12 and the results are compared with experimental results from [18], [19] and [29]. According to the results, the discrepancy between the simulation and the experimental results demonstrate that smooth theory could not predict well the absorption performance as the sub-cooled level increase. In general, the smooth laminar theory of falling film heat and mass transfer problem could describe well in the Re range of $0 < Re < 200$ and near thermodynamic equilibrium conditions. When the Re number is higher, the discrepancy between simulation and experimental results are much higher.

4.4.2 Simulation studies of absorption falling film with nanofluid

In all the cases, the concentration distribution of the bulk film was under MWR conditions. The correlation for the condition was extracted from Morison et al. [30] as shown in Equation 4.13 and validated in Chapter 3 for various conditions.

$$\Gamma = 0.13(1-\cos\theta)^{0.764}\sigma^{0.764}\rho^{0.255}\mu^{-0.018} \tag{4.13}$$

Besides, in Chapter 3, a super hydrophilic coating stainless tube was employed in the MWR test section, and the results show that the Re number could reach as low as 30. The nominal condition for LiBr is set as inlet solution temperature 44.44°C at 60wt%. The pressure is under 935Pa and the wall is set as isotherm. For the Carrol solution, the solution is 67wt% at the same pressure.

a) Simulation results of the normal and super hydrophilic stainless steel surface.

Effectiveness $eff = (T - T_{\text{in}})/(T_{\text{in}} - T_{\text{w}})$ is used to describe the temperature distribution of the liquid along with the falling film. Figure 4.13 shows the temperature effectiveness of two different working pairs on the interface of the falling film. The temperature effectiveness for the two solutions has similar behaviour. The results show that the coating has more effect on the LiBr solution since it has higher thermal conductivity and thinner film thickness. Similarly, the concentration distribution has the same tendency as shown in Figure 4.14 for both working pairs. Since the heat and mass transfer in this process is coupled and thermodynamic equilibrium exits on the interface, the results of the concentration should have the same perspective as temperature.

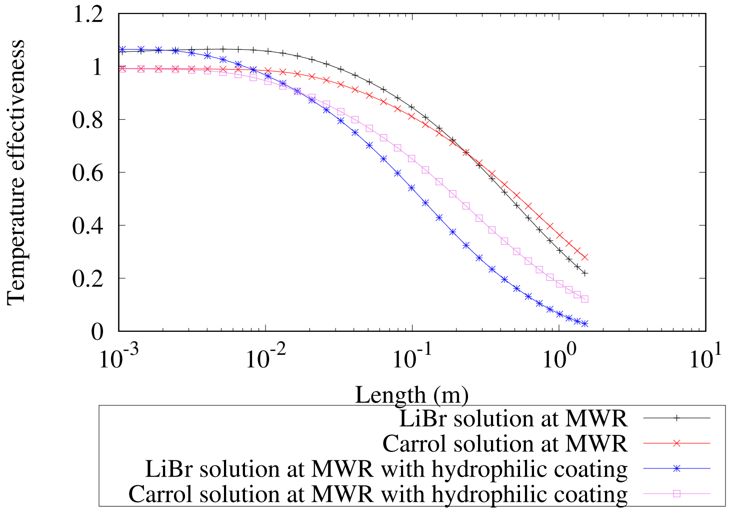

Figure 4.13: Numerical results of interface temperature difference effectiveness distribution of the solution. The nominal condition is 60wt%, T_{in}=44.44°C at 935Pa of both LiBr and Carrol solution, the Γ was calculated according to Equation 4.13 at stainless steel surface and hydrophilic coated stainless steel surface

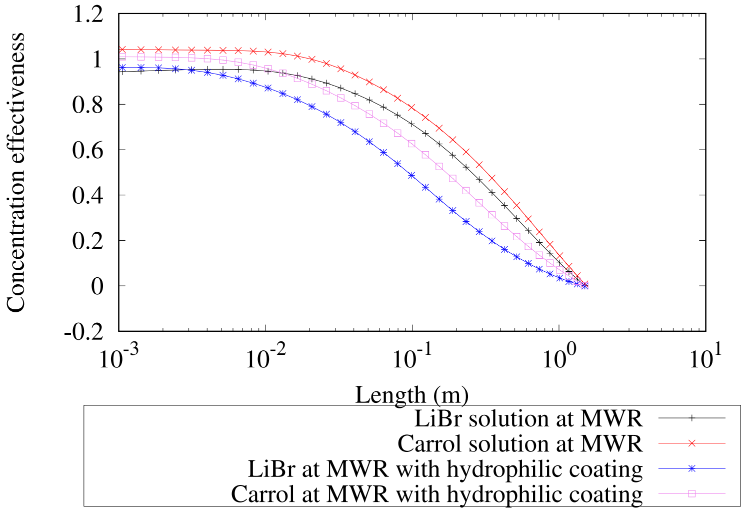

Figure 4.14: Numerical results of interface concentration difference effectiveness distribution of the solution. The nominal condition is 60wt%, T_{in}=44.44°C at 935Pa of both LiBr and Carrol solution, the Γ was calculated according to Equation 4.13 at stainless steel surface and hydrophilic coated stainless steel surface

Table 4.2: Thermophysical properties of of test liquids

		MWR at SS		MWR at SS*	
		LiBr	Carrol	LiBr	Carrol
Re	[-]	65	33	21	10
Γ	$[\mathrm{m \cdot s^{-1}}]$	0.098	0.094	0.029	0.028
$\dot{m}_{\mathrm{abs}}$	$[\mathrm{kg(m \cdot s)^{-1}}]$	1.881E-3	1.428E-3	1.469E-3	1.296E-3
α	$[\mathrm{W(m \cdot K)^{-1}}]$	1170	901	1444	1120
δ	[m]	3.89E-4	4.99E-4	2.66E-4	3.4E-4

For 60% LiBr aqueous solution and 67% Carrol solution, the corresponding Re are 68 and 42, respectively, the Γ is around 0.09 $\mathrm{kg(m \cdot s)^{-1}}$ for both solutions. The LiBr solution has a $\dot{m}_{\mathrm{abs}}$ at 1.96E-3 $\mathrm{kg(m \cdot s)^{-1}}$ and α at 1150 $\mathrm{W(m \cdot K)^{-1}}$, the value for Carrol solution is 1.36E-3 and 851, correspondingly. The information is summarized in Table 4.2

b) Simulation results of modified properties vertical falling film absorption.

As explained in the previous section 4.3, nanofluid could increase the thermal conductivity hence the heat transfer coefficient of the liquid falling film. It is instructive for the modification of the working pairs to quantify each thermodynamic property effect to the heat and mass performance of the vertical falling film, though some properties could be barely changed without affecting other properties. Considering the details of the heat and mass transfer, Figure 4.15,4.16 shows the surface temperature change rate due to the thermodynamic property changes.

As shown in the results, for both working pairs, with the same thermodynamic modification change rate, only thermal conductivity increase has a positive effect on the heat transfer to the falling film, while viscosity and mass diffusivity increase has a negative influence. To quantify this effect of mass diffusivity and viscosity, simulations with property modification have also been carried out, as shown in Figure 4.17. However, increasing D increments the mass transfer rate while a high μ will reduce it.

Considering the nanofluid will barely change other properties except thermal conductivity, if nanofluid is employed in the working pairs, the absorbed mass rate and heat transfer coefficients could be described in Figure 4.18,4.19, for LiBr solution, 4.20 and 4.21 for Carrol solution. The properties of the nanofluid are calculated according to Section 2.5. A similar effect behavior can be observed for both solutions from a qualitative point of view. However, compared with the LiBr solution, at the same $Re = 80$, the Carrol solution has a 20% and 30% lower mass and heat transfer rate.

As shown in Figure 4.18 and 4.20, the mass absorption rate increases with the Re

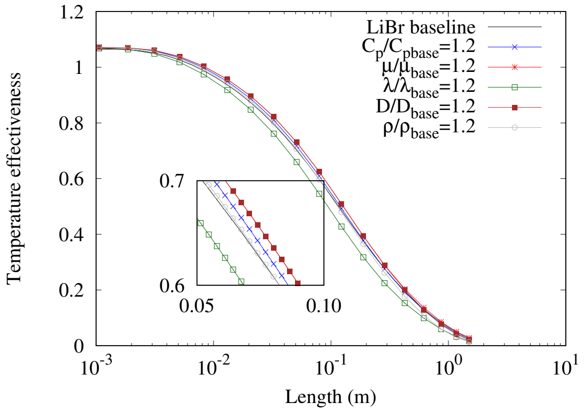

Figure 4.15: Numerical results of surface temperature change rate of different thermaldynamic properties of LiBr solution, whic are $C_{\mathrm{p}}, \mu, \lambda, D, \rho$. The nominal condition is 60wt%, T_{in}=44.44°C at 935Pa, $\Gamma = 0.028\mathrm{kg{\cdot}m^{-1}s^{-1}}$

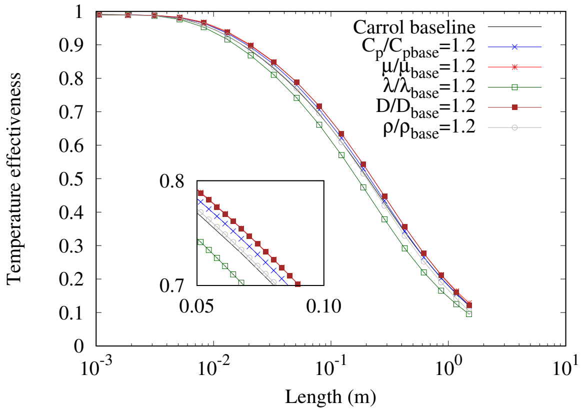

Figure 4.16: Numerical results of surface temperature change rate of different thermaldynamic properties of Carrol solution, whic are $C_{\mathrm{p}}, \mu, \lambda, D, \rho$.. The nominal condition is 60wt%, T_{in}=44.44°C at 935Pa, $\Gamma = 0.028\mathrm{kg{\cdot}m^{-1}s^{-1}}$

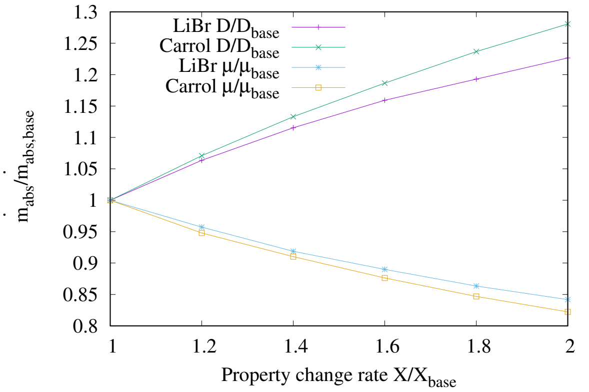

Figure 4.17: Numerical results of mass absorption rate change due to modified thermophysical properties. The nominal condition for LiBr solution is 60wt%, T_{in}=44.44°C at 935Pa, and the nominal condition for Carrol solution is 67wt%, T_{in}=44.44°C at 935Pa

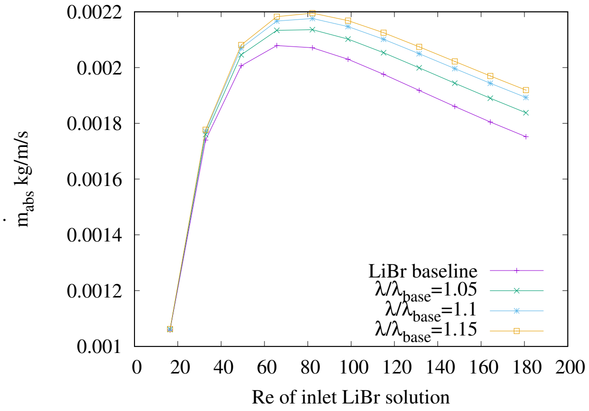

Figure 4.18: Numerical results of mass absorption rate of nanofluid LiBr solution. The nominal condition is 67wt%, T_{in}=44.44°C at 935Pa

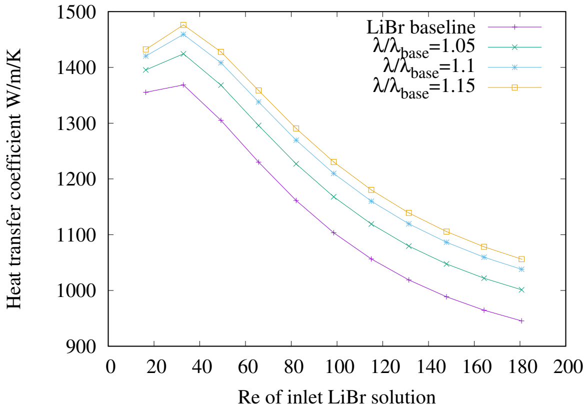

Figure 4.19: Numerical results of heat transfer coefficient of nanofluid LiBr solution. The nominal condition is 60wt%, T_{in}=44.44°C at 935Pa

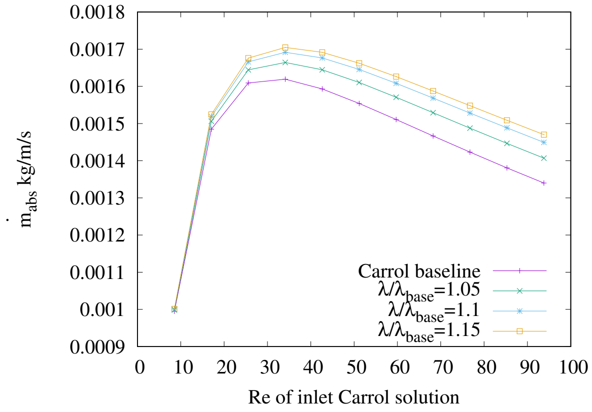

Figure 4.20: Numerical results of mass absorption rate of nanofluid Carrol solution. The nominal condition is 67wt%, T_{in}=44.44°C at 935Pa

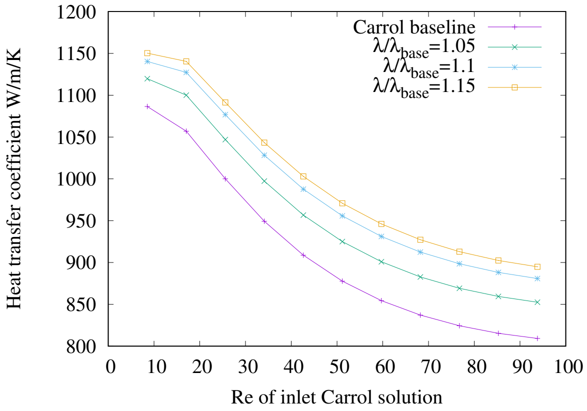

Figure 4.21: Numerical results of heat transfer coefficient of nanofluid LiBr solution. The nominal condition is 67wt%, T_{in}=44.44°C at 935Pa

to the peak and then decrease, for LiBr and Carrol solution the corresponding Re is 70 and 35, which are slightly greater than the MWR. The thermal conductivity could increase the mass transfer rate and has higher effect on higher Re, however, the effect will increase slower as λ/λ_{base} increases. In terms of the heat transfer of the falling film, from Figure 4.19 and 4.21, the heat transfer coefficient will only decrease when the Re increases in the studied Re range.

4.5 Conclusions

In this chapter the heat and mass transfer of the vertical falling film are investigated with simulations and experiments. In the heat transfer part, the analytical results and experimental results agree with the smooth laminar theory of the interfacial temperature distribution at low Re. Meanwhile the simulation doesnot agree with the empirical correlation from other authors due to the correlation is average for the whole film. In general, high Re could lead to high heat transfer coefficient, at the same mass flow rate, the heat transfer coefficient of water could be 3 times higher than EG. When nanofluid is introduced, there are greater discrepancies between the simulation and experimental results. The discrepancies could be driven by the dispersant in the nanofluid and the precision of the prediction of the thermodynamic properties, especially for the surface tension and thermal conductivity. When the combind heat and mass transfer are studied, the smooth laminar theory simulation results agree well with experimental data from other authors at low Re range and near thermodynamic equilibrium conditions. In terms of the thermodynamic properties, λ could increase heat transfer, though high μ,D will reduce heat trasnfer, high D will increase mass transfer while high μ will reduce it. The ideal working pairs should have higher thermal conductivity, higher mass diffusivity and lower viscosity.

NOMENCLATURE

Name	**Description**
A	Area [m^2]
C	Concentration [$-$]
C_p	Specific heat [$\mathrm{J{\cdot}kg^{-1}{\cdot}K^{-1}}$]
D	Mass diffusivity coefficient [$\mathrm{m^2{\cdot}s^{-1}}$]
e	Base of natural logarithms [-]
g	Acceleration of gravity [$\mathrm{m{\cdot}s^{-2}}$]
h	Specific enthalpy [kJ·kg]
Ha	Absorption enthalpy [kJ/kg]
Ka	Kapiza number $\left(\frac{\sigma\rho^3}{\mu^4 g}\right)^{\frac{1}{3}}$
L	Length [m]
Le	Lewis number$\frac{\kappa}{D}$
$\dot{m}$	Mass flow rate [$\mathrm{kg(m{\cdot}s)^{-1}}$]
P	Pressure [Pa]
Re	Reynolds number $\frac{4\Gamma}{\mu}$
$\overline{St}$	Modified Stefan number$\frac{X_\mathrm{in}(T_\mathrm{eq}-T_\mathrm{in})}{\Delta(X_\mathrm{eq}-X_\mathrm{in})}$
T	Temperature [°C]
u	Velocity [$\mathrm{m{\cdot}s^{-1}}$]
$\bar{u}$	Mean velocity [$\mathrm{m{\cdot}s^{-1}}$]
x, y	Coordinates [m]
X, Y	Dimensionless coordinates [$-$]
Greek letter	**Description**
α	Heat transfer coefficient [$\mathrm{Wm^{-2}K^{-1}}$]
$\bar{\alpha}$	Average heat transfer coefficient [$\mathrm{Wm^{-2}K^{-1}}$]
Γ	Mass flow rate per length [$\mathrm{kg(m{\cdot}s)^{-1}}$]
δ	Mean film thickness [m]
Δ	Dimensionless film thickness [-]
ΔT_m	Logarithmic temperature difference [$^\circ$C]
θ	Contact angle [$\circ$]
Θ	Dimensionless temperature [-]
κ	Thermal diffusivity [$\mathrm{m{\cdot}s^{-2}}$]
λ	Thermal conductivity [$\mathrm{Wm^{-1}K^{-1}}$]
μ	Dynamic viscosity [$\mathrm{Pa{\cdot}s^{-1}}$]
ν	Kinetic viscosity [$\mathrm{m^2s^{-1}}$]
ρ	Density [$\mathrm{kg{\cdot}m^{-3}}$]
σ	Surface tension [mN·m]
ϕ	Volumentric concentration [-]
Υ	Dimensionless concentration [-]

Abbreviation	**Description**
2-EH	2-Ethylhexanol
CNT	Carbon nanotubes
EG	Ethylene glycol
MWR	Minimum wetting rate
SS	Stainless steel
SS*	Hydrophilic coated stainless steel
VLE	Vapor-liquid equilibrium
wt	Weight ratio

Subscripts & Superscripts	**Description**
abs	Absorbed
base	Baseline
eq	Thermodynamic equilibrium
if	Interface
in	Inlet
LiBr	LiBr solution
out	Outlet
tube	Tube
w	Wall

References

[1] S. Ishigai, S. Nakanisi, T. Koizumi, Z. Oyabu, Hydrodynamics and Heat Transfer of Vertical Falling Liquid Films, Chemical Pharmaceutical Bulletin 17 (11) (1994) 1460–1462.

[2] Y. Yue, J. Yang, X. Li, Y. Song, Y. Zhang, Z. Zhang, Experimental research on falling film flow and heat transfer characteristics outside the vertical tube, Applied Thermal Engineering 199 (March) (2021) 117592. `doi:10.1016/j.applthermaleng.2021.117592`.

[3] V. E. Nakoryakov, N. I. Grigoryeva, Nonisothermal absorption in thermotransformers, Journal of Engineering Thermophysics 19 (4) (2010) 196–271. `doi:10.1134/S1810232810040028`.

[4] T. Meyer, F. Ziegler, Analytical solution for combined heat and mass transfer in laminar falling film absorption using first type boundary conditions at the interface This paper is dedicated to emer. Prof. Dr.-Ing. Dr.-Ing.h.c. Hans Dieter Baehr., International Journal of Heat and Mass Transfer 73 (2014) 141–151. `doi:10.1016/j.ijheatmasstransfer.2014.01.074`.

[5] M. Turkyilmazoglu, Heat absorption due to falling film with imposed uniform mass fraction at the wall, International Journal of Heat and Mass Transfer 177 (2021) 121585. `doi:10.1016/j.ijheatmasstransfer.2021.121585`.

[6] F. Zhang, D. L. Tang, J. Geng, Z. X. Wang, Z. B. Zhang, Study on the temperature distribution of heated falling liquid films, Physica D: Nonlinear Phenomena 237 (7) (2008) 867–872. `doi:10.1016/j.physd.2007.10.018`.

[7] R. A. Seban, Transport to falling films, in: International Heat Transfer Conference Digital Library, Begel House Inc, 1978.

[8] W. A. Miller, M. Keyhani, The Correlation of Simultaneous Heat and Mass Transfer Experimental Data for Aqueous Lithium Bromide Vertical Falling Film Absorption, Journal of Solar Energy Engineering 123 (1) (2001) 30. `doi:10.1115/1.1349550`.

[9] R. Yang, B. D. Wood, A numerical modeling of an absorption process on a liquid falling film, Solar Energy 48 (3) (1992) 195–198. `doi:10.1016/0038-092X(92)90138-Z`.

[10] R. Yang, J. Derming, Heat and mass transfer on the wavy film absorption process, The canadian Journal of Chemical Engineering 71 (9) (1993) 959–966.

[11] M. L. Yuksel, E. U. Schlunder, Heat and Mass Transfer in Non-isothermal Absorption of Gases in Falling Liquid Films Part I: Experimental Determination of Heat and Mass Transfer Coefficients Wgrrne-und Stoffiibergang bei der nichtisothermen Gasabsorption am Rieselfilm Teil I: Experiment, Chemical Engineering Process 22 (1987) 193–202.

[12] V. Patnaik, A simple model for the design of vertical tube absorbers, ASHRAE Transactions (27-30).

[13] A. P. Lamourelle, O. C. Sandall, Gas adsorption into a turbulent liquid, Chemical Engineering Science 27 (1) (1972) 1035–1043.

[14] E. García-Rivera, J. Castro, J. Farn, A. Oliva, Numerical and experimental investigation of a vertical LiBr falling film absorber considering wave regimes and in presence of mist flow, International Journal of Thermal Sciences 109 (2016) 342–361. `doi:10.1016/j.ijthermalsci.2016.05.029`.

[15] E. García-Rivera, J. Castro, J. Farnós, C. Oliet, Numerical and experimental study of absorption of H 2 O vapor in wavy falling film of LiBr aqueous solution in vertical tubes and in presence of non-absorbables, International Journal of Refrigeration 100 (2019) 184–195. `doi:10.1016/j.ijrefrig.2019.01.022`.

[16] N. Brauner, D. M. Maron, H. Meyerson, Coupled heat condensation and mass absorption with comparable concentrations of absorbate and absorbent, International Journal of Heat and Mass Transfer 32 (10) (1989) 1897–1906. `doi:10.1016/0017-9310(89)90159-2`.

[17] W. A. Miller, The Experimental Analysis of Aqueous Lithium Bromide Vertical Film Absorption, Ph.D. thesis (1998).

[18] M. Medrano, M. Bourouis, A. Coronas, Absorption of water vapour in the falling film of water-lithium bromide inside a vertical tube at air-cooling thermal conditions, International Journal of Thermal Sciences 41 (9) (2002) 891–898. `doi:10.1016/S1290-0729(02)01383-2`.

[19] W. A. Miller, H. Perez-Blanco, Vertical-tube aqueous LiBr falling film absorption using advanced surfaces, Tech. rep. (1993).

[20] H. Zhang, D. Yin, S. You, W. Zheng, S. Wei, Experimental investigation of heat and mass transfer in a LiBr-H2O solution falling film absorber on horizontal tubes: Comprehensive effects of tube types and surfactants, Applied Thermal Engineering 146 (2019) 203–211. `doi:10.1016/j.applthermaleng.2018.09.127`.

[21] H. Gao, F. Mao, Y. Song, J. Hong, Y. Yan, Effect of adding copper oxide nanoparticles on the mass/heat transfer in falling film absorption, Applied Thermal Engineering 181 (August). `doi:10.1016/j.applthermaleng.2020.115937`.

[22] L. Zhang, Z. Fu, Y. Liu, L. Jin, Q. Zhang, W. Hu, Experimental study on enhancement of falling film absorption process by adding various nanoparticles, International Communications in Heat and Mass Transfer 92 (2018) 100–106. `doi:10.1016/j.icheatmasstransfer.2018.02.011`.

[23] R. H. Wassenaar, Simultaneous heat and mass transfer in a horizontal tube absorber: Numerical tools for present and future absorber designs.

[24] G. Wang, P. Dong, Y. Lu, M. Zeng, Q. Zhang, Experimental and theoretical investigation on the surface tension of nano-Lithium Bromide solution, International Communications in Heat and Mass Transfer 123 (March) (2021) 105231. `doi:10.1016/j.icheatmasstransfer.2021.105231`.

[25] F. Blangetti, R. Krebs, E. Schlunder, Condensation in vertical tubes–experimental results and modeling, Chemical Engineering Fundamentals 1 (2) (1982) 20–63.

[26] A.~Kramida, Yu.~Ralchenko, J.~Reader, No Title, NIST Atomic Spectra Database (ver. 5.7.1), [Online]. Available: {\tt{https://physics.nist.gov/asd}} [2015, April 16]. National Institute of Standards and Technology, Gaithersburg, MD. (2019).

[27] L. McNeely, Thermodynamic properties of aqueous solutions of lithium bromide, ASHRAE Transactions 85 (1) (1979) 413–434.

[28] W. Biermann, Proprties of the Carrol system and a machine design for solar-powered, air-cooled, absorption space cooling. Phase I and Phase II. Final report, September 1977-March 1979, Tech. rep., Carrier Corp., Syracuse, NY (USA). Energy Systems Div. (1981).

[29] K. Kim, T. Ameel, B. Wood, Performance evaluations of licl and libr for absorber design applications in the open-cycle absorption refrigeration system (1997) 165–173.

[30] K. R. Morison, Q. A. G. Worth, N. P. O'Dea, Minimum wetting and distribution rates in falling film evaporators, Food and Bioproducts Processing 84 (4 C) (2006) 302–310. `doi:10.1205/fbp06031`.

5

Numerical studies on an air-cooled absorption machine system

ABSTRACT

In this chapter, an air-cooled, single-effect absorption system is evaluated from the point of view of 1st and 2nd thermodynamic principles for two different applications: absorption chiller and heat pump. One of the most widely used working pairs, LiBr-H_2O, is applied in this study due to its high performance in the absorption cycle. Their performance is compared with another working fluid (Carrol). The Carrol solution reduces the crystallization risk for the high concentration solution that enters the absorber. The numerical modelling was implemented on a modular object-oriented simulation platform (NEST platform tool), which allows linking different components. In the simulations performed, the heat source temperature in the system is in the range of 70−90 °C, and the inlet temperature at evaporator secondary circuit at chiller application is fixed in two values, 9°C and 14°C, and for heat pump application in 0°C and -5°C. Moreover, EG is added to the evaporator at heat pump application to prevent the refrigerant water from freezing below zero. The mass concentration studied is in the range of EG 10−40%. The simulation results show the COP of an absorption chiller and heat pump are around 0.7 and 1.6, respectively, and the COP_{EX} values are 0.2−0.6 at chiller application and 0.5−1.5 at heat pump application. Compared to the LiBr system, the Carrol system has about 6.4% higher COP, about 6.3% higher COP_{EX}, and a decrease of about 19% in cooling capacity. For the heat pump application, the heat

source temperature should be lower than 90°C, and EG concentration at the evaporator has been chosen as 30% as an optimal value. According to the operation condition, this EG concentration has been determined to avoid freezing in the evaporator in the studied working range. However, too much EG significantly decreases the pressure in the evaporator and increases the viscosity, and subsequently the maintenance is increased as more vacuum tightness is required. The numerical model for the absorption system was described in previous works [1] and [2], and the energy/exergy analysis was demonstrated in [3].

5.1 Introduction of absorption system simulation

Many authors have studied absorption systems in chiller or heat pump mode with experiments or thermodynamic models on energy and exergy perspectives. Steady-state simulation models were developed by [4, 5] to predict the performance of an absorption refrigeration system using LiBr-H_2O as a working pair. Fu et al. [6] developed a library of elemental dynamic models for absorption refrigeration systems with different working mediums and cycle configurations, which grants the library flexibility and extensibility. Also, dynamic simulations models of a single-effect LiBr-H_2O absorption refrigeration system were developed by [7–9]. Zinet et al. [7] explores the dynamic behavior of the system to basic input parameters change, and Iranmanesh et al. [8] created a new algorithm for calculating the flow rate in a solution circulation and validated the simulation results against a double-effect absorption chiller from startup to shutdown. Xu et al. [9] investigated the thermal mass effects and compared two different control strategies. Matsushima et al. [10] developed a dynamic simulation focused on arbitrary cycle configurations, with a computational time of 1/20 physical time using a destop computer. [11, 12] performed numerical simulations about an absorption LiBr-H_2O heat pump to predict the transient operating characteristics and performance. Evola et al. [13] proposed a model for the dynamic simulation of a solar-assisted single-stage LiBr-H_2O absorption chiller and validated the numerical model with a commercial absorption machine. Castro et al. [1] did the transient model for an air-cooled LiBr-H_2O absorption chiller based on heat and mass transfer empirical correlations. The model was validated with experimental results with a small-capacity (2-3kW) direct air-cooled machine in Castro et al. [14]. The simulation of the absorption machine under steady-state Q_{EVA} = 6kW and a COP of 0.74.

For the absorption system in chiller mode, Aprhornratana et al. [15] provided a second-law thermodynamic analysis for a single-effect absorption refrigerator cycle.

They concluded that the internal irreversibilities at the absorber and generator, which are the highest, could be reduced by increasing the solution heat exchanger effectiveness. Besides, they stated that priority should be given to the evaporator when improving the cycle performance. Talbi et al. [16] did an exergy analysis on a single-effect absorption refrigeration cycle with LiBr-H_2O, in which it was revealed that the absorber has the highest exergy loss (59.06% of total) and explained the importance of an exergy analysis due to the exergy change caused by absorption/desorption process. Kaushik et al. [17] investigated single effect and series flow double effect absorption systems in refrigeration with LiBr-H_2O. In this work, the optimum value of the COP is achieved at 91°C for the single effect system and 150°C for the double effect system. It was observed that the absorber is the main component of exergy loss in both systems, and lowering the absorber temperature may bring down the optimum generator temperature and COP_{EX} (exergetic efficiency)while increasing the COP. Samanta et al. [18] did an optimization analysis of a single-stage LiBr-H_2O absorption system for domestic refrigeration application. The optimum generator temperature corresponding to entropy-based analysis is lower than the value obtained with energy-based modelling. When the evaporator temperature is at 15°C, and condenser temperature at 35°C, optimum generator temperature corresponding to maximum COP is around 72°C while corresponding to minimum entropy generation rate is about 65°C. Bellos et al. [19] compared two different working pairs LiBr-H_2O, and LiCl-H_2O in the absorption cooling system. In their results, when the ambient temperature is 30°C, and evaporator temperature is 10°C, the optimal temperature for the inlet solution at generator was 91°C with a COP 0.836, and a COP_{EX} of 0.387 with working pair LiCl-H_2O, while for LiBr-H_2O the values were 93, 0.796, and 0.36, respectively. Though working pairs LiCl-H_2O have a higher COP and COP_{EX}, there is a higher risk in crystallization, which limits the concentration range, hence the system performance. Gogoi et al. [20] reported that the maximum concentration in the LiCl-H_2O is about 0.5 while for LiBr-H_2O is 0.75. Lake et al. [21] did mathematical modelling of an absorption cooling system with EES software and determined that the absorber, generator, and condenser are the largest contributions to the exergy destruction with 30%, 31%, and 28% percentages, respectively. The exergy efficiency reported was 16% with a COP 0.65.

Izquierdo et al. [22] analyzed a LiBr-H_2O, high-temperature heat pump combined with waste heat recovery. They reported that at generator temperatures of 178−200°C, with a waste heat source at 60°C, obtained a COP of 1.4. It was established that the heat generated from the heat pump was 31% cheaper compared with the mechanical compression heat pump technology in terms of energy cost, and the COP_{EX} was reported as 75% higher. Cheng et al. [23] presented a detailed thermodynamic analysis of absorption heat pumps. The performances values reported for the absorption system studied at heat pump application were a COP of 1.7 and a COP_{EX} of 0.9, while at chiller application, the COP value was 0.7, and for the COP_{EX} 0.3.

There are also studies with chiller and heat pump modes in the same system. Lee et al. [24] analyzed a LiBr-H_2O absorption system for cooling and heating applications based on the first and second laws of thermodynamics. It was reported that, in chiller application, low chilled water temperatures lead to lower COP and higher COP_{EX}. In heat pump application, on the other hand, if a high source temperature is applied, this will lead to higher COP and COP_{EX} and a higher risk of crystallization. Sencan et al. [25] also analyzed a LiBr-H_2O absorption system for cooling and heating applications based on first and second laws of thermodynamics. It was demonstrated that in the range 65°C−120°C, when the heat source temperature increases, the COP will increase and level out, while the COP_{EX} will decrease in both heating and cooling applications. In the cooling application, the COP will increase along with the chilled water temperature though the COP_{EX} will decrease. Meanwhile, both COP and COP_{EX} will increase for the heating application with the chilled water temperature.

Besides, several works with the Carrol-H_2O pair were carried out in terms of 1^{st} thermodynamic principle. Rivera et al. [26], Romero et al. [27], Ibarra-Bahena et al. [28] analyzed both points of view, experimental development, and numerical modelling of a heat transformer with Carrol-H_2O as working pair. These analyses show that the working pair Carrol-H_2O has better performance in heat transformers. On the other hand, Kerme et al. [29] analyzed the LiBr absorption refrigeration system integrated with a flat plate solar collector. The results show that the collector and generator are the principal sources of irreversibility, and cooling capacity increases with heat source temperature while COP_{EX} reduces. Palacio-Bereche et al. [30] presented a methodology for the exergy analysis with chemical exergy calculation according to activity coefficients and other parameters in a LiBr absorption system at refrigeration application. Considering chemical exergy, in the single-effect absorption refrigeration system with a cooling tower, the exergy destruction rate at components are 52%,18%,10%,13%,6% at the generator, absorber, condenser, evaporator, and solution heat exchanger, respectively.

Freezing phenomena at the evaporator may also limit the application of the heat pump with an absorption system using H_2O as a refrigerant. Many strategies have been used to overcome this issue. For heat pump application, reported in [31], [22], [23], [24], [25], the evaporator was driven by solar-heated water, waste heat, or geothermal water, etc. On the other hand, [32] presents a study using LiBr as brine in the evaporator to achieve subzero temperatures.

In this chapter, the dynamic model NEST is used for the simulation. The numerical results are also compared with experimental data from Evola et al. [13], which shows a good agreement. An air-cooled absorption machine is under analysis based on the first and second laws of thermodynamics in both chiller and heat pump applications. In terms of the heat pump applications, EG was introduced to the evaporator to avoid the freezing problem. Steady state and dynamic simulations are carried out to study the system performance under various conditions.

5.1.1 Absorption system description

The sketch of the single effect absorption system is shown in Figure 5.1, a solution pump circuits the solution side, points 5, 6, 7, and 8. The pressure drop at the solution heat exchanger is used as an expansion valve to separate low and high pressure in the absorber and generator. The generator is driven by hot water (point 11), and its temperature varies in the range of 70−90°C. The absorber and condenser are air-cooled through a ventilator. In the evaporator, the chilled H_2O/EG solution enters at point 15 at a fixed temperature (9−14°C as chiller, and -5−0°C as a heat pump). Regarding the refrigerant side, 1 is superheated water vapour that leaves the generator, 2 is saturated liquid water that leaves the condenser, 3 is the liquid water that enters the evaporator, and 4 is the water vapour that leaves the evaporator at the corresponding temperature.

To specify the application of the absorption system, Figure 5.2 shows the two applications studied for the absorption system: a) heat pump and b) absorption chiller. The absorption machine is air-cooled, with a vertical arrangement of the components according to patent application in [33], as shown in the picture. The fan circulates the air and passes through the absorber and condenser. In the heat pump application the absorption machine will work inside the building. The evaporator secondary circuit will take heat from the outdoor temperature. The heat will be rejected from the absorber and condenser as output to heat the building. The outside temperature is fixed to 0 and -5°C, while the building temperature is set to 15 and 20°C. A temperature of 15°C is be usual for a farm, and 20°C is typical for a residential building. In the chiller application, the ambient for the machine is the outside condition. In this case, the secondary circuit of the evaporator will take heat from the building to the ambient as cooling output. The outdoor temperature is set to 20−35°C, and chilled water input temperature is set to 9 and 14°C.

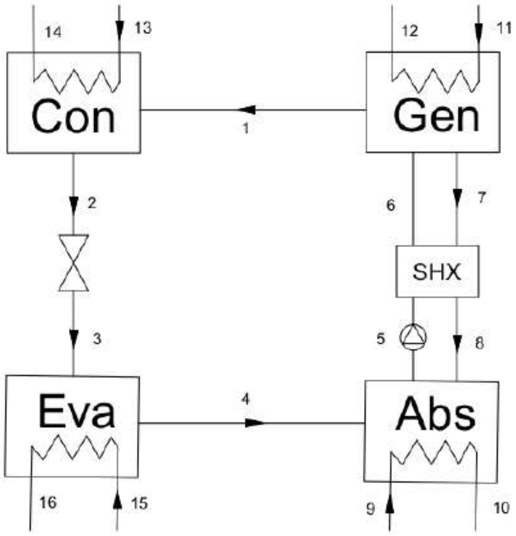

Figure 5.1: Sketch of Thermodynamic cycle

5.1.2 Assumptions for the theoretical cycle

The following assumptions have been made in the development of numerical modelling :

(i) The analysis is made under steady-state conditions.

(ii) The components in the system are considered well insulated.

(iii) Pressure changes in the components are considered negligible except for valves and pumps.

(iv) Crystallization is not directly imposed in the simulation. The results are compared to the crystallization curve to assess the cycle.

(v) The vapour temperature is the same as the outlet temperature of the corresponding liquid.

(vi) The entropy for both working pairs at 50%, 0°C, 1 atm is set to 0 $\text{kJ}\cdot(\text{kg}\cdot\text{K})^{-1}$, and the T_{AMB} at each operation condition is the reference point.

(vii) The secondary cycle is operated under atmospheric environment.

(viii) The partial pressure of EG is neglected.

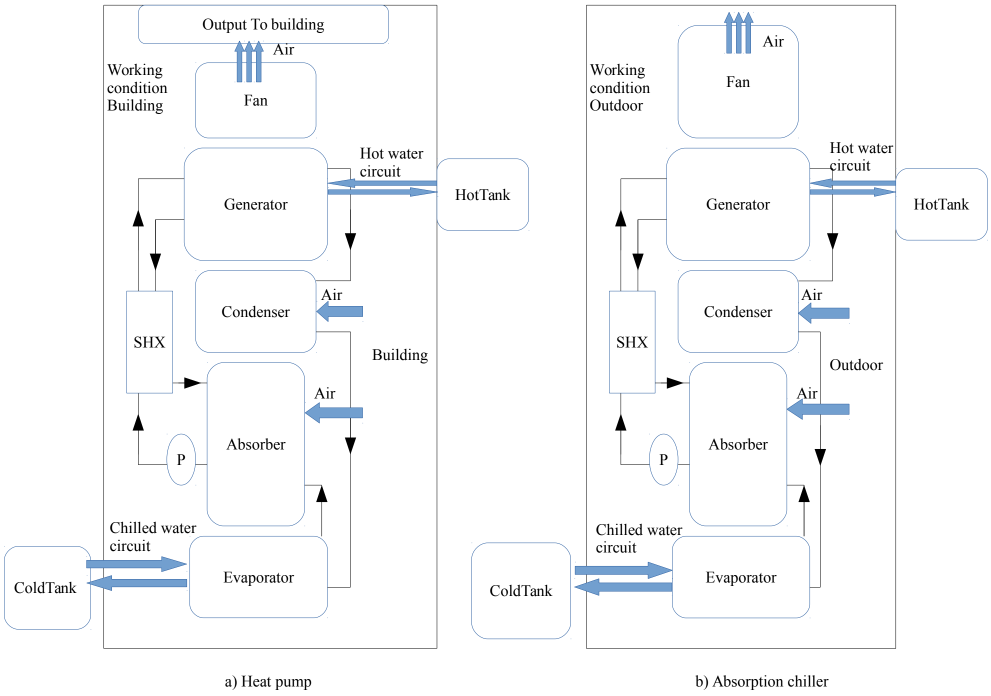

Figure 5.2: Different applications of absorption system

5.1.3 Numerical implementation

The detailed information of the equations solved for the whole system is explained in the previous work of [1]. The model is based on heat, mass, and momentum balances in each system' component, calculating heat and mass transfer coefficients by embedding available empirical information. This system of equations was implemented in an in-house C++ numerical platform(NEST). The governing equations for the absorber are showed as below:

Equation 5.1 is mass balance in the liquid solution phase, Equation 5.2 is LiBr balance, Equation 5.3 is state equation of the vapour(ideal gas is assumed), Equation 5.4 is volume balance in the absorber, Equation 5.5 is energy balance, Equation 5.6 is the discharge process, Equation 5.7 is vapour mass transfer rate:

$$\dot{m}_{\mathrm{s,in}} - \dot{m}_{\mathrm{s,out}} + \dot{m}_{\mathrm{v,abs}} = \frac{dM_{\mathrm{s}}}{dt} \tag{5.1}$$

$$\dot{m}_{\mathrm{s,in}} C_{\mathrm{s,in}} - \dot{m}_{\mathrm{s,out}} C_{\mathrm{s,out}} = M_{\mathrm{s}} \frac{dC_{\mathrm{s}}}{dt} + C_{\mathrm{s}} \frac{dM_{\mathrm{s}}}{dt} \tag{5.2}$$

$$M_{\mathrm{v}} R_{\mathrm{v}} T_{\mathrm{ABS}} = p_{\mathrm{ABS}} V_{\mathrm{v}} \tag{5.3}$$

$$V_{\mathrm{v}} = V_{\mathrm{ABS}} - M_{\mathrm{s}}/\rho_{\mathrm{s}} \tag{5.4}$$

$$\begin{aligned} Q_{\mathrm{pri,ABS}} - Q_{\mathrm{loss,ABS}} = \dot{m}_{\mathrm{s,out}} h_{\mathrm{s,out}} - \dot{m}_{\mathrm{s,in}} h_{\mathrm{s,in}} - \\ \dot{m}_{\mathrm{v,abs}} h_{\mathrm{v}} + M_{\mathrm{s}} (C_{\mathrm{p}})_{\mathrm{s}} \frac{dT_{\mathrm{s}}}{dt} + v_{\mathrm{s}} \frac{dM_{\mathrm{s}}}{dt} \end{aligned} \tag{5.5}$$

$$\dot{m}_{\mathrm{s,out}} = C_d S \sqrt{\frac{2\rho_s \left[\rho_s g (H+z)\right]}{\xi}} \tag{5.6}$$

$$\dot{m}_{\mathrm{v,abs}} = \beta_{\mathrm{ABS}} \rho_{\mathrm{s}} A \frac{1}{2} \Big((C_{\mathrm{in,if}} - C_{\mathrm{in,b}}) - (C_{\mathrm{out,if}} - C_{\mathrm{out,b}}) \Big) \tag{5.7}$$

5.1.4 Exergy analysis modelling

For each component, the result of exergy destruction could be expressed as

$$E_{\mathrm{D,m}} = \sum_{\mathrm{in}} \dot{m}_{\mathrm{in}} e_{\mathrm{in}} - \sum_{\mathrm{out}} \dot{m}_{\mathrm{out}} e_{\mathrm{out}} + \sum Q \left(1 - \frac{T_{\mathrm{AMB}}}{T_{\mathrm{in}}} \right) - W \tag{5.8}$$

$E_{\mathrm{D,m}}$ is the exergy destruction in the component, $\dot{m}_{\mathrm{i}}$ and e_{i} are the inlet mass flow and corresponding exergy, respectively, and m_{out}, e_{out} are the same variables at the outlet. The third term represents the exergy destruction due to heat transfer between the component and the ambient. As mentioned before, heat loss is neglected. Hence this term will be 0.

For the whole system we have

$$E_{\mathrm{D,tot}} = \sum_m E_{\mathrm{D,m}} \tag{5.9}$$

In the absorption chiller aplication, the COP and COP_{EX} are calculated as below:

$$COP = \frac{Q_{\mathrm{EVA}}}{Q_{\mathrm{GEN}}} \tag{5.10}$$

$$COP_{\mathrm{EX}} = \frac{Q_{\mathrm{EVA}}\left(1 - \frac{T_{\mathrm{AMB}}}{T_{\mathrm{cold}}}\right)}{Q_{\mathrm{GEN}}\left(1 - \frac{T_0}{T_{\mathrm{hot}}}\right)} \tag{5.11}$$

In the heat pump application we have the following expressions:

$$COP = \frac{Q_{\mathrm{ABS}} + Q_{\mathrm{CON}}}{Q_{\mathrm{GEN}}} \tag{5.12}$$

$$COP_{\mathrm{EX}} = \frac{Q_{\mathrm{ABS}}\left(1 - \frac{T_{\mathrm{AMB}}}{T_{\mathrm{cold}}}\right) + Q_{\mathrm{CON}}\left(1 - \frac{T_{\mathrm{AMB}}}{T_{\mathrm{cold}}}\right)}{Q_{\mathrm{GEN}}\left(1 - \frac{T_{\mathrm{AMB}}}{T_{\mathrm{hot}}}\right)} \tag{5.13}$$

5.2 Comparison between LiBr-H_2O and Carrol-H_2O systems for chiller mode

The NEST platform is being used to model the behavior of a system with fixed physical components but variable working fluids, and the simulation results may be different depending on the properties of the working fluid being used.

5.2.1 Nominal conditions

The resutls of the nominal condition in chiller mode are demonstrated in Table 5.1, where the heat source temperature is T_{11}=88°C, the evaporator secondary inlet temperature is T_{15}=14°C and ambient temperature is T_{AMB}=35°C. As the cycle is a single effect and air-cooled, the concentration difference is relatively small compared to typical water-cooled systems. This fact is due to the reduced capacity of the air-cooled absorber, which is compensated with higher solution mass flows (similar to results obtained in the experiment reported at in Castro et al. [34]). The results demonstrate that the working temperature for LiBr and Carrol solutions are quite similar. However, the main difference is the superheated vapour from the generator: the temperature and mass flow rate of the vapour in the LiBr system are higher than the Carrol system due to the solution thermodynamic properties.

Calculate from the results of the Table 5.2, the *COP* of the LiBr, Carrol system is 0.735, 0.782, respectively, and at the nominal conditions, the LiBr system has a higher cooling capacity, while the Carrol system has a higher *COP*. The exergy destruction most occurs in the generator and absorber, and also in this latter component, there is almost all chemical exergy destruction. On the other hand, the physical exergy destruction is sometimes below zero because the physical exergy of the water vapour from the evaporator at low temperatures also has negative values. The chemical exergy depends only on the concentration of different species. Moreover, the chemical exergy destruction in the absorber is regenerated in the generator. In Table 5.2, the results $E_{D,\mathrm{phy}}$ represents the physical exergy destruction rate at each component, and $E_{D,\mathrm{tot}}$ represents the total exergy destruction rate, and $\eta_{ED,m}$ shows that the exergy loss percentage in the LiBr system for generator, absorber, evaporator, and condenser, which are 14%, 52.8%, 9.9%, 16.1%, respectively. In the Carrol system, the combined exergy loss in the generator and absorber is considered due to the difficulty of quantifying the correct activity coefficient, which is very sensitive to estimating chemical exergy in a multicomponent solution system. In this case, the combined exergy loss represents 59.98% of the total.

In Table 5.3, α_{int} and α_{ext} represent the heat transfer conductance in the primary and secondary side, respectively, and β is the mass transfer coefficient. As commented above, these coefficients are calculated with empirical correlations, see in Castro et al. [1]. Also, the model is validated by experimental data from an own-designed and commissioned small capacity absorption chiller in Castro et al. [34]. When the two working pairs are compared, the results in Table 5.3 illustrate that the coefficient α will reduce 20−30% in the generator, absorber, and evaporator, for the case of the Carrol system, compared to the LiBr system. Meanwhile, in the absorber the coefficient β will also drop significantly, to almost 50%. The significant drop in the heat and mass transfer coefficients may be caused by the increase of the viscosity of the solution. From Table 5.4 we could conclude that at the same operation condition, the Carrol solution

Table 5.1: Thermodynamic state of different points of two systems at chiller mode

Point	Working fluid	T [°C]	C [wt%]	$\dot{m}$ [$\mathrm{kg\cdot s^{-1}}$]	h [$\mathrm{kJ\cdot kg^{-1}}$]	s [$\mathrm{kJ\cdot(kg\cdot K)^{-1}}$]	e_{phy} [$\mathrm{kJ{\cdot}kg^{-1}}$]	e_{ch} [$\mathrm{kJ{\cdot}kg^{-1}}$]
1	LiBr	84.46	×	0.00243	2641.0	8.45	46.3	50
	Carrol	84.53	×	0.00185	2651.4	8.52	59.5	50
2	LiBr	41.29	×	0.00243	172.0	0.59	1.348	50
	Carrol	39.78	×	0.00185	166.1	0.57	1.611	50
3	LiBr	9.94	×	0.00243	172.0	0.62	-7.9	50
	Carrol	10.91	×	0.00185	166.1	0.59	-5.78	50
4	LiBr	8.15	×	0.00243	2520.0	8.9	-213.7	50
	Carrol	9.52	×	0.00185	2521.6	8.88	-204.9	50
5	LiBr	39.79	57.4	0.0973	102.8	0.24	0.3	521
	Carrol	39.72	65.0	0.106	92.9	0.28	-0.4	2919
6	LiBr	78.29	57.4	0.0973	179.9	0.47	6.9	521
	Carrol	79.88	65.0	0.106	172.2	0.53	2.5	2919
7	LiBr	84.46	58.9	0.0949	197.3	0.49	8.4	542
	Carrol	84.53	66.1	0.104	184.0	0.54	3.9	2959
8	LiBr	44.14	58.9	0.0949	118.2	0.26	0.3	542
	Carrol	42.94	66.1	0.104	102.8	0.30	-0.4	2959
9	LiBr	35	×	1.86	308.4	1.7	0	0
	Carrol	35	×	1.86	308.4	1.73	0	0
10	LiBr	38.91	×	1.86	312.3	1.74	0.02	0
	Carrol	37.95	×	1.86	311.3	1.74	0.01	0
11	LiBr	88	×	0.48	368.6	1.17	66.8	50
	Carrol	88	×	0.48	368.6	1.17	66.8	50
12	LiBr	84.17	×	0.48	352.5	1.13	64.5	50
	Carrol	85.09	×	0.48	356.4	1.14	15.0	50
13	LiBr	35	×	1.06	308.4	1.73	0	0
	Carrol	35	×	1.06	308.4	1.73	0	0
14	LiBr	38.58	×	1.06	312.0	1.74	0.02	0
	Carrol	37.73	×	1.06	311.1	1.74	0.01	0
15	LiBr	14	×	0.334	58.8	0.21	3.2	50
	Carrol	14	×	0.334	58.8	0.21	3.2	50
16	LiBr	9.94	×	0.334	41.8	0.15	4.5	50
	Carrol	10.91	×	0.334	45.8	0.16	4.2	50

Table 5.2: Thermodynamic state of components of two systems in chiller mode

		Q[kW]	W[kW]	$E_{\mathrm{D,phy}}$[kW]	$E_{\mathrm{D,tot}}$[kW]	η_{ED}[%]
Generator	LiBr	7.73	0.089	0.86	0.18	14.01
	Carrol	5.88	0.089	0.72	1.82	59.98*
Absorber	LiBr	7.73	0.240	-0.013	0.67	52.80
	Carrol	5.53	0.240	-0.043	-1.14	
evaporator	LiBr	5.68	0.039	0.13	0.13	9.93
	Carrol	4.60	0.039	0.094	0.094	8.22
Condenser	LiBr	6.04	0.110	0.20	0.20	16.07
	Carrol	4.33	0.113	0.21	0.21	18.40
SHX	LiBr	–	–	0.091	0.091	7.20
	Carrol	–	–	0.15	0.15	13.40

*The number represents the percentage combined in generator and absorber

Table 5.3: Heat and mass transfer parameters of components of two systems in chiller mode

		GEN	ABS	CON	EVA
α_{int} [W·K^{-1}]	LiBr	2822	2720	43696	4622
	Carrol	2100	1831	47724	3081
α_{ext} [W·K^{-1}]	LiBr	32346	5287	3234	14068
	Carrol	32346	5287	3234	14068
β [m·s^{-1}]	LiBr	0.0014	5.38E-5	-	-
	Carrol	0.0013	2.82E-5	-	-
Pressure [Pa]	LiBr	7615	1197	7615	1197
	Carrol	7024	1268	7024	1268

has a much higher viscosity when is compared with the LiBr solution, hence, reduce the heat and mass transfer significantly. On the other hand, COP_{EX} in LiBr is 0.366, while in Carrol system is 0.389.

5.2.2 Results varying external conditions(steady-state)

The heat source temperature effect is the most discussed aspect in the absorption system, as it is reported in [35], [19], [18], [29]. They reported that COP is increasing, achieving a maximum value, decreasing finally along with the heat source temperature. On the other hand, the COP_{EX} will only decrease. In this work the T_{11} range is 70−90°C, where the COP will decrease slightly along with the T_{11} range and COP_{EX} will decrease rapidly. Figures 5.3,5.4 show the numerical results of COP, COP_{EX}, cooling capacity

Table 5.4: Dynamic viscosity of LiBr and Carrol solution at similar working conditions

T_{11}[°C]	LiBr			Carrol		
	T_8[°C]	C_8 [wt%]	μ[Pa·s^{-1}]	T_8[°C]	C_8 [wt%]	μ[Pa·s^{-1}]
70	33.3	56.2	4.2E-3	32.7	64.5	1.1E-2
85	36.9	61.1	5.7E-3	37.1	69.3	1.7E-2

Q_{EVA} and exergy destroyed rate $E_{\mathrm{D,tot}}$ for the absorption system with different working pairs against the heat source temperature at various ambient/evaporator temperatures. Results illustrate again that the Carrol system has a higher COP and COP_{EX} while the cooling capacity is smaller when compared with the LiBr system. High ambient temperatures generally lead to a higher COP_{EX} and a lower COP since the ambient temperature will not affect the generator performance much but will limit the heat rejection to the air from the condenser and absorber. This effect in the Carrol system is lower when compared with the LiBr system. In the Carrol system, the increment of cooling capacity decreases along with the heat source temperature, while in the LiBr system, it grows proportionally with the heat source. This effect happens because the Carrol solution has a higher viscosity than the LiBr solution, as shown in Table 5.4, which will decrease the heat and mass transfer coefficients, hence the total cooling capacity. Low chilled water temperature will increase the COP_{EX} while the COP will slightly decrease. In Table 5.4, the T_8 represents the absorber inlet solution temperature. The results varying the concentration demonstrate that the viscosity of Carrol solution in the absorber is not only higher and also increases faster when compared to LiBr solution.

Figure 5.5 shows the crystallization risk vs. the heat source temperature T_{11} for all the cases studied, in the results, $C_{8,\mathrm{MAX}} = f(T_8)$ where $C_8, T_8, C_{8,\mathrm{MAX}}$ are the absorber inlet solution concentration, temperature, max concentration without crystallization at corresponding temperature, respectively. Thus, when the rate exceeds 1.0 means the solution encounter crystallization risk. This position correspond at the absorber inlet (where crystallization usually first happens). We could observe from the results that the machine is performed in the studied range without crystallization risk. In general, the minimum concentration of the cycle is limited by environmental conditions; at higher chilled water temperatures, the risk of crystallization increases as the concentration differences between absorber inlet and concentration limit is higher. This issue is associated with higher cooling capacities for higher chilled water temperatures. In addition, at higher heat source temperatures, the risk of crystallization is also increased as the working concentrations if the rest of the conditions remain unchanged. Hence, the lower chilled water temperature could help avoid crystallization in the same situation, while a high heat source temperature will increase the risk. In terms of the T_{AMB}, it leads to low COP and working capacity since higher T_{AMB} reduces the air-cooled capacity for the system. Meanwhile the COP_{EX} increases with the T_{AMB} since high T_{AMB} leads to lower $E_{\mathrm{D,tot}}$. In general conclusion, in the same operation conditions, the Carrol system has a lower crystallization risk when compared with the LiBr system, which means the operating range for the Carrol system is more extended. Moreover, all the tests are simulated without heat and mass transfer enhancement methods. Adding surfactants may increase the heat and mass transfer capability, thus improving the system capacity and indirectly increasing the working operation range.

5.2.3 Dynamic simulation of two working pairs at chiller mode

In the previous work, [1], the results with LiBr solution show 13 hours of transient test campaign, including start-up and shutdown. In this section, a similar test campaign procedure is reproduced for the working pairs LiBr-H_2O and Carrol-H_2O, and the results are shown in Figure 5.6. The simulation is carried out employing PID-controlled auxiliary vessels, and the controller parameters were calculated according to Ziegler et al. [36]. Fixed temperatures in the generator secondary circuit are set as 75, 80, 85, 90, and 95°C. Each temperature will last two hours, and a warm-up for 2 hours, a shutdown of 1 hour, so the test campaign will be 13 hours in total. The results demonstrate the evolution of COP, cooling capacity, operation conditions, and crystallization risk against time. The results show that at chiller mode, the Carrol solution has a smaller cooling capacity, a slightly higher COP, and a lower crystallization risk when compared with the LiBr solution. The cooling capacity increases with heat source temperature and decreases while T_{AMB} increases for the two working pairs. The temperatures evolution of the secondary circuit is also demonstrated in the results. The simulations are carried out in two different T_{AMB}, 30°C and 35°C. Moreover, as EG will be added to avoid the freezing problem in the heat pump mode, simulations of chiller mode with EG in the evaporator may also be interesting since this could avoid changing the liquid in the evaporator. A simulation at chiller mode with 10wt% EG added in the evaporator at T_{AMB}=35°C is carried out, as showed in Figure 5.6. The results show the addition of EG significantly decreases COP and cooling capacity since the EG solution has a much higher viscosity, subsequently in a smaller heat and mass transfer in the evaporator.

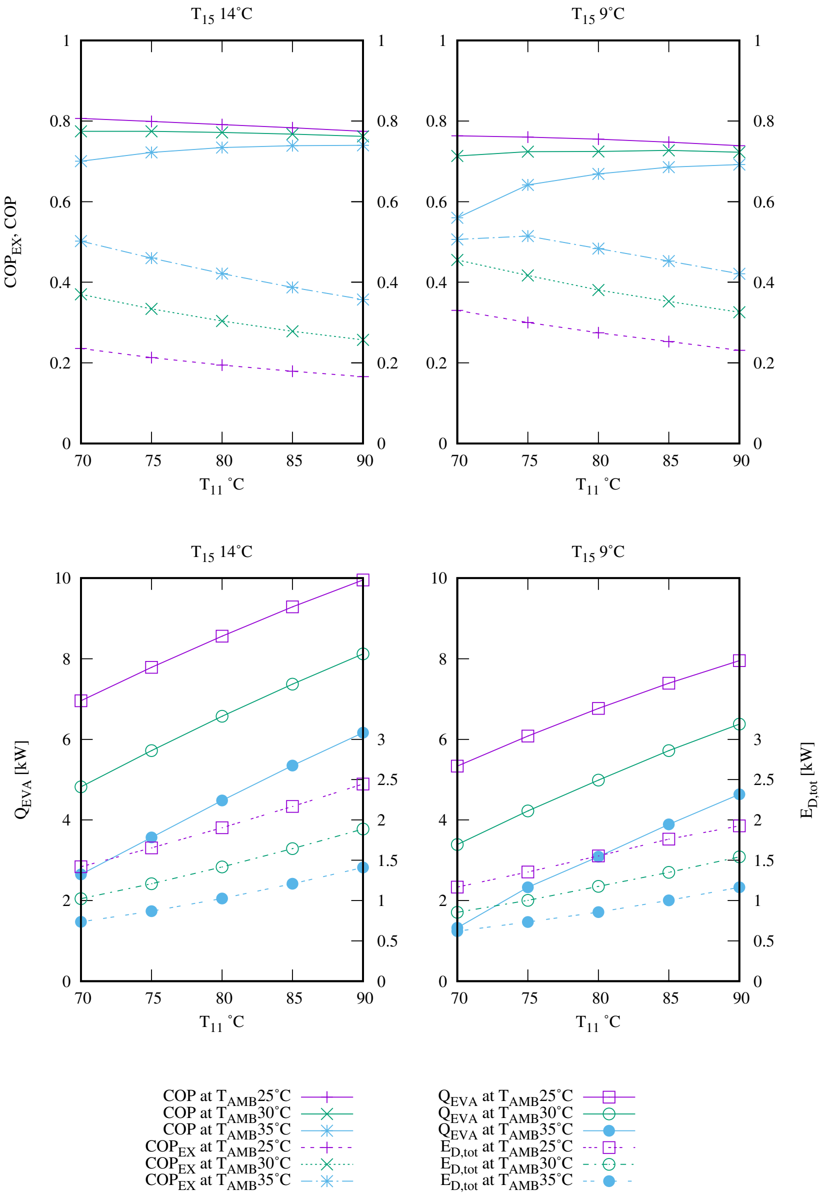

Figure 5.3: LiBr system performance (COP,COP_{EX}), cooling capacity (Q_{EVA}), and exergy destruction rate ($E_{\mathrm{D,tot}}$) against heat source temperature (T_{11}) at different ambient temperature (T_{AMB}) and different evaporator secondary inlet temperature (T_{15})

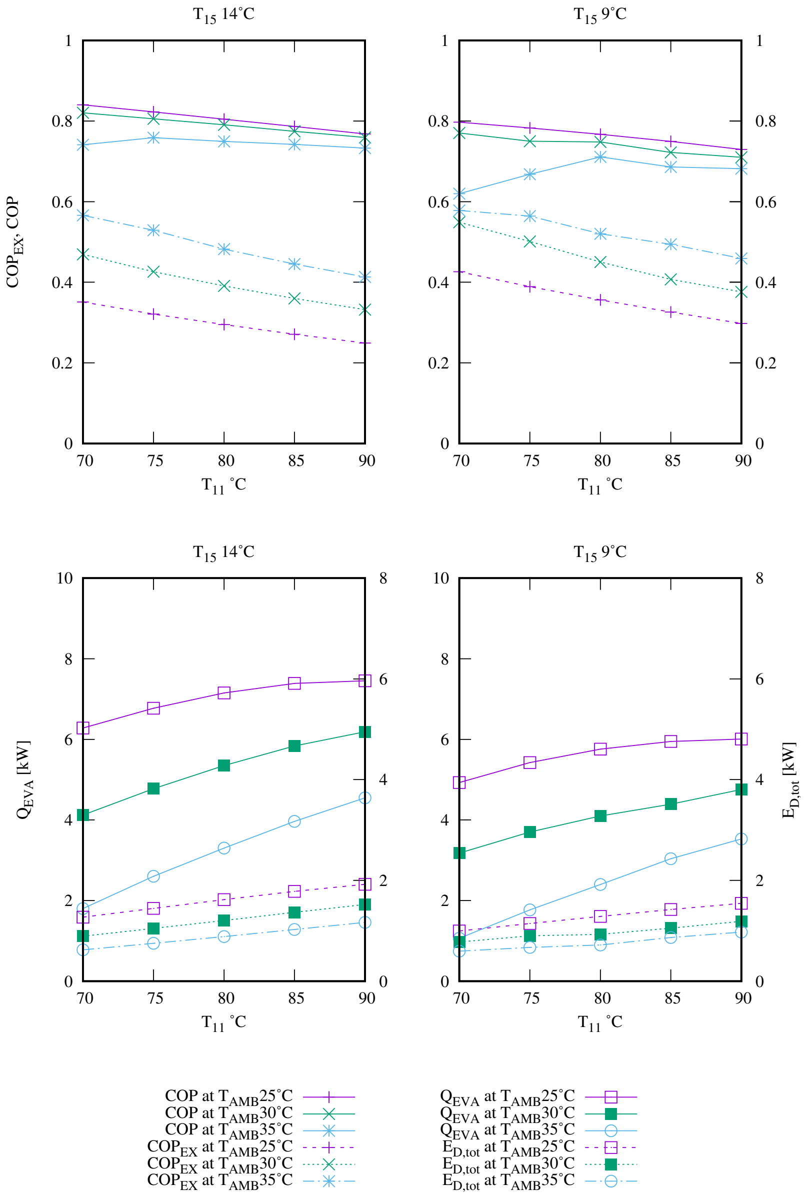

Figure 5.4: Carrol system performance (COP,COP_{EX}), cooling capacity (Q_{EVA}), and exergy destruction rate ($E_{\mathrm{D,tot}}$) against heat source temperature (T_{11}) at different (T_{AMB}) and evaporator secondary inlet temperature (T_{15})

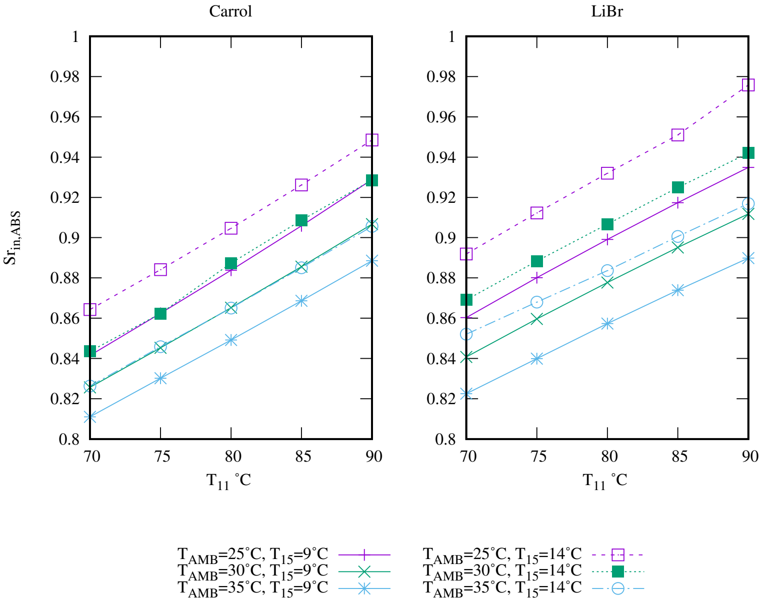

.

Figure 5.5: Solution saturation rate of LiBr, Carrol system in chiller mode at absorber inlet against heat source temperature T_{11}, and the saturation rate is $C_8/C_{8,\mathrm{MAX}}$

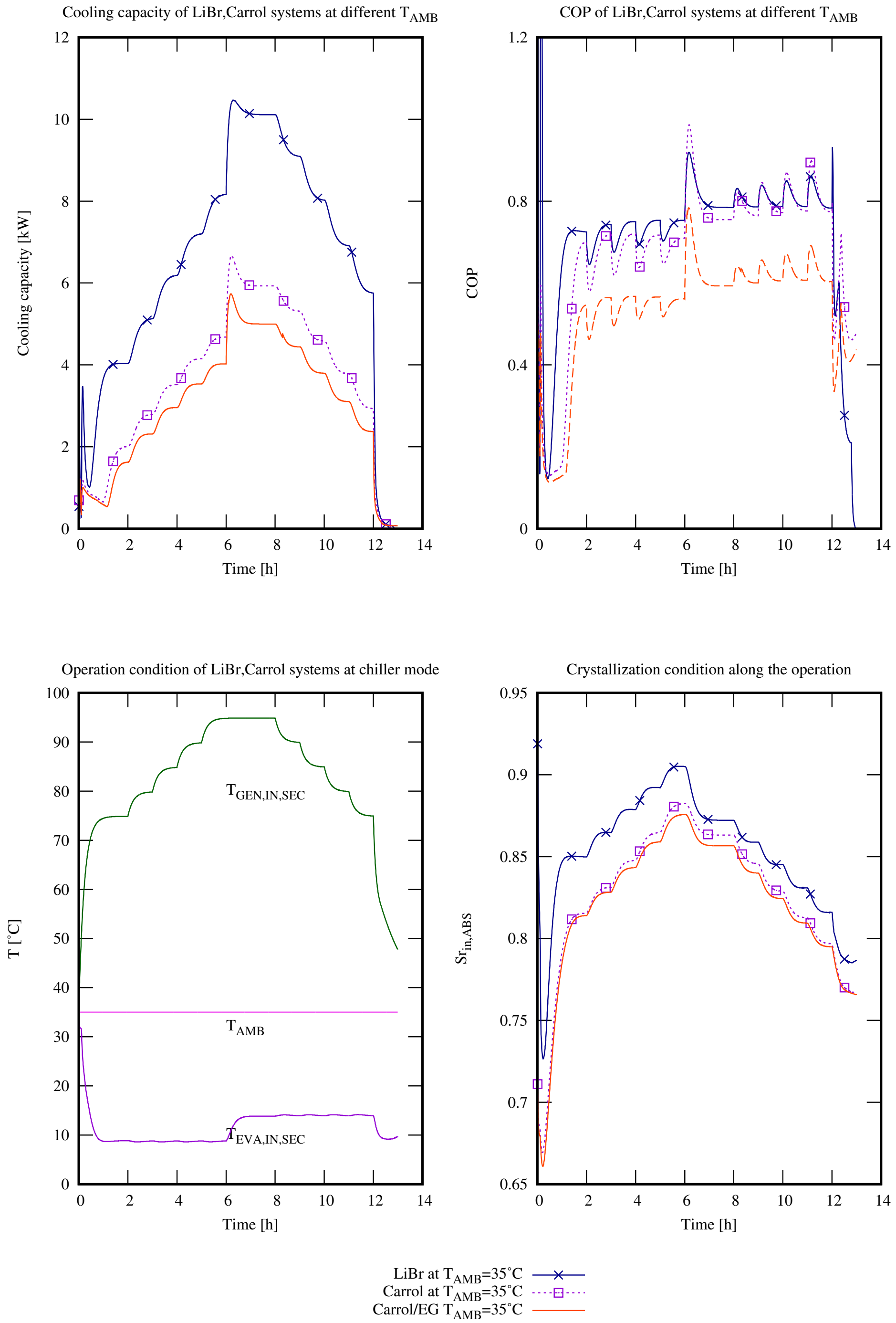

Figure 5.6: Absorption system dynamic numerical results at chiller application with two wroking pairs LiBr-H_2O and Carrol-H_2O. Evolution of COP and capacity respect transient external conditions: generator secondary circuit inlet temperature ($T_{\mathrm{GEN,IN,SEC}}$), ambient temperature (T_{AMB}), and saturation rate of absorber inlet solution concentration (C)

5.3 Results with Carrol-EG/H_2O system in heat pump mode

When the absorption system works in heat pump application as a warm air source to the building, the evaporator secondary circuit is at outdoor temperature, thus needing EG to avoid freezing in winter. In this section, this temperature (T_{15}) is chosen as 0 and-5°C. Herold [37] comments that the crystallization risk for LiBr-H_2O systems will increase when the absorber is air-cooled. Moreover, the working limit for the LiBr-H_2O system as the heat pump is around 5°C at outdoor temperature. In such conditions, this system cannot be operated as a heat pump. To overcome crystallization and freezing problems, Carrol-H_2O is used as the working pair in heat pump application, and EG is also introduced into the evaporator primary and secondary circuits.

5.3.1 Nominal conditions

Tables 5.5, 5.6, 5.7 show the simulation results of heat pump application at nominal condition with EG mass concentration 30% in the evaporator primary and secondary, where T_{11}=80°C, and T_{15}=-5°C. Table 5.5 shows the working parameters for each point at the system, Table 5.6 shows the working conditions for each component, and Table 5.7 demonstrates the heat and mass transfer coefficient at each component and the operated pressure. The mean temperature inside the evaporator is around -10°C, and the freezing point of the EG solution is at -14°C. The COP is 1.6, COP_{EX} is 0.8, and the $E_{\mathrm{D,tot}}$ of the condenser percentage increases when compared to the absorption chiller application with the Carrol system due to the temperature decrease of superheated water vapour from the generator at point 1. Moreover, the proportion of $E_{\mathrm{D,tot}}$ in generator and absorber decreases from 60% to 47%. When Tables 5.7 is compared to Table 5.3, the results show that in the heat pump condition, the heat transfer parameters are lower than in the chiller absorption application. The pressure in both generator and evaporator in the Carrol-EG/H_2O system is significantly lower than in the absorption chiller condition due to the presence of ethylene glycol in the evaporator primary, which makes the vacuum level of the equipment more demanding in the heat pump application.

Table 5.5: Thermodynamic state of points of Carrol-EG/H_2O system in heat pump mode

	T [°C]	C [wt%]	$\dot{m}$ $[\mathrm{kg \cdot s^{-1}}]$	h $[\mathrm{kJ \cdot kg^{-1}}]$	s $[\mathrm{kJ \cdot (kg \cdot K)^{-1}}]$	e_{phy} $[\mathrm{kJ \cdot kg^{-1}}]$	e_{ch} $[\mathrm{kJ \cdot kg^{-1}}]$
1	71.85	×	0.0034	2630.2	8.71	80.595	50
2	28.61	×	0.0034	120.0	0.42	-0.35	50
3	-9.90	×	0.0034	120.0	0.44	-3.2	50
4	-10.84	×	0.0034	2499.4	9.41	-256.9	50
5	34.74	65.9	0.11	86.1	0.24	-0.5	2919
6	67.41	65.9	0.11	149.9	0.45	3.4	2919
7	71.85	68.0	0.10	164.9	0.46	5.6	2959
8	37.21	68.0	0.10	98.8	0.25	0.07	2959
9	20.00	×	1.86	293.3	1.68	0	0
10	24.04	×	1.86	297.4	1.69	0.03	0
11	80.00	×	0.48	335.0	1.08	72.2	50
12	75.03	×	0.48	314.2	1.02	68.8	50
13	20.00	×	1.06	293.3	1.68	0	0
14	25.04	×	1.06	298.4	1.70	0.04	0
15	-5.00	×	0.33	-18.2	0.38	5.7	50
16	-9.90	×	0.33	-36.5	0.31	8.1	50

Table 5.6: Thermodynamic state of component of Carrol-EG/H_2O system

	Q[kW]	W[kW]	$E_{\mathrm{D,phy}}$[kW]	$E_{\mathrm{D,tot}}$[kW]	η_{ED}[%]
Generator	10	0.089	1.24	3.3	45.6
Absorber	7.6	0.22	-0.55	-2.6	
Evaporator	6.1	0.026	0.25	0.2	16
Condenser	8.5	0.11	0.43	0.4	28.2
SHX	–	–	0.16	0.2	10.2

Q represents heat transfer rate

W is the electricity consumption rate

$E_{\mathrm{D,phy}}$ is physical exergy destruction rate

$E_{\mathrm{D,tot}}$ is the total exergy destruction rate

η_{ED} is the exergeric efficiency

Table 5.7: Heat and mass transfer parameters of components of Carrol-EG/H_2O system

	GEN	ABS	CON	EVA
α_{int} $[\mathrm{W \cdot K^{-1}}]$	1851	1480	34479	6536
α_{ext} $[\mathrm{W \cdot K^{-1}}]$	31756	5206	3234	14969
β $[\mathrm{m \cdot s^{-1}}]$	1.3E-3	2.11E-5	-	-
Pressure [Pa]	3856	233	3856	232

α_{int} is the primarty circuit heat transfer coefficient

α_{ext} is the secondary circuit heat transfer coefficient

β is the mass transfer coefficient

5.3.2 Results varying external conditions(steady-state)

Figure 5.7 shows that the COP of the heat pump is around 1.6 and barely affected by other parameters like ambient temperature, evaporator secondary inlet temperature, and ethylene glycol concentration in the evaporator but the COP decreases slightly with the heat source temperature. Meanwhile, COP_{EX} is more sensitive to the parameters mentioned above, which decreases along with the heat source temperature, ambient temperature, and evaporator secondary inlet temperature. Figure 5.8 shows the numerical results of the heat rejected from the condenser, absorber, and the exergy destruction of the machine, which illustrates that the total energy output $\{Q_{\mathrm{CON}}+Q_{\mathrm{ABS}}\}$ will increase along with the heat source temperature and then decrease. It could be concluded that there will be an optimal heat source temperature at a precise operation condition, which grants higher energy output. For example, when the T_{15} is 0°C at T_{AMB} = 15° C, the optimum heat source temperature is near 70°C, and if T_{AMB} = 20°C and T_{15} is 0°C, the optimum heat source temperature will be 80°C. This optimum value is due to opposite effects: on the one hand, increasing generator temperatures favours higher capacities, as the temperature differences in the heat exchanger also increase; on the other hand, increasing generator temperatures also increase concentrations, and, by consequence, viscosity values also increase (see Table 5.4), affecting heat and mass transfer coefficients negatively. Higher ambient temperatures or lower temperature Carrol solution may lead to a slightly higher optimum operating temperature. Moreover, the $E_{\mathrm{D,tot}}$ maximum value generally takes place behind the optimum temperature. The higher concentration of EG in the evaporator will also lead to lower exergy destruction and higher heat capacity. Though EG in the evaporator primary circuit will affect the thermodynamic properties, with a significant decrease of the equilibrium pressure in the evaporator, it is compensated by relatively high absorption capability in the absorber for the decreased working temperatures at heat pump conditions. For example, when the T_{15} is 0°C, T_{11} is 80°C, the ambient temperature is (T_{10}) 20°C (indoor environment), so the machine has a evaporation/absorption rate at 3.16E-3 g·s^{-1}, 3.06E-3 g·s^{-1}, for EG concentration at 10%,40%, respectively. We could obtain from the numerical results the optimal operation heat source temperature. However, both crystallization and freezing limits have to be taken into consideration in the system. As shown in Figure 5.9, the risk of crystallization is low but could occur when the T_{11} exceeds 90°C. Therefore, the optimum heat source temperature could be applied without crystallization problems.

As a general recommendation, the safe temperature of the heat source should be lower than 90°C in an absorption heat pump system when T_{15}=0°C. Besides, the solution

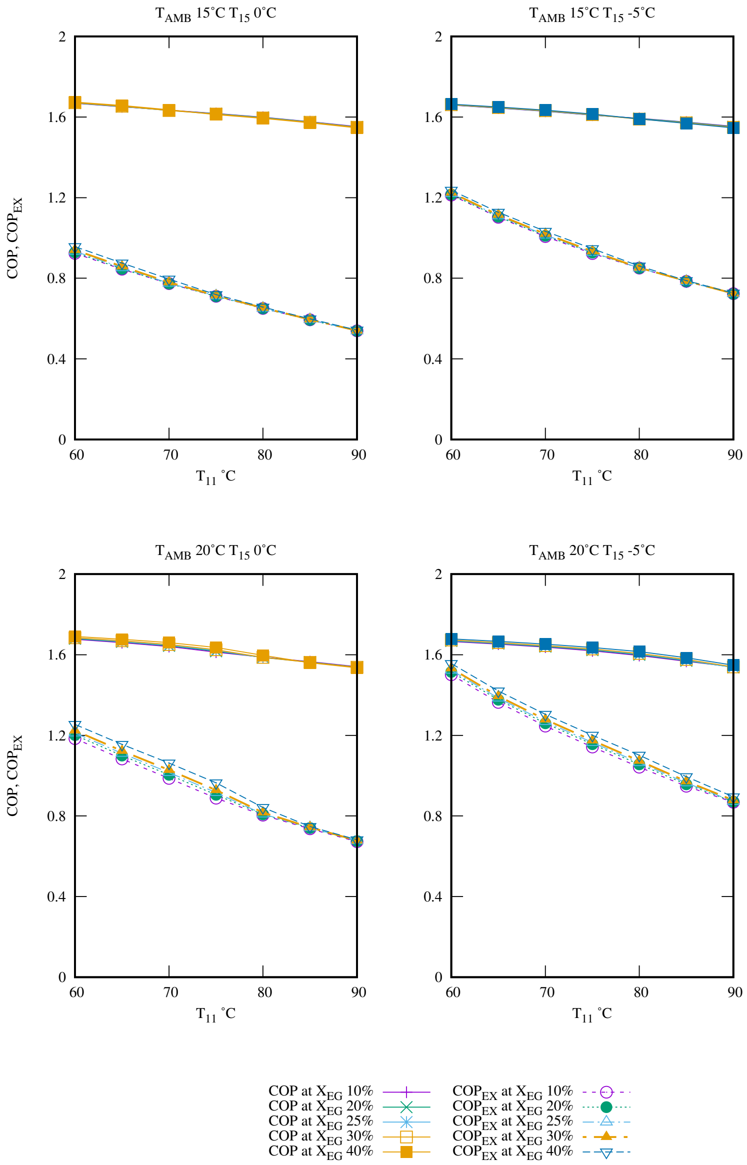

Figure 5.7: Numerical results of COP,COP_{EX} in Carrol-EG/H_2O system against heat source temperature T_{11} at different ambient temperature (T_{AMB}), evaporator secondary inlet temperature (T_{15}) and EG mass concentration in evaporator (C_{EG})

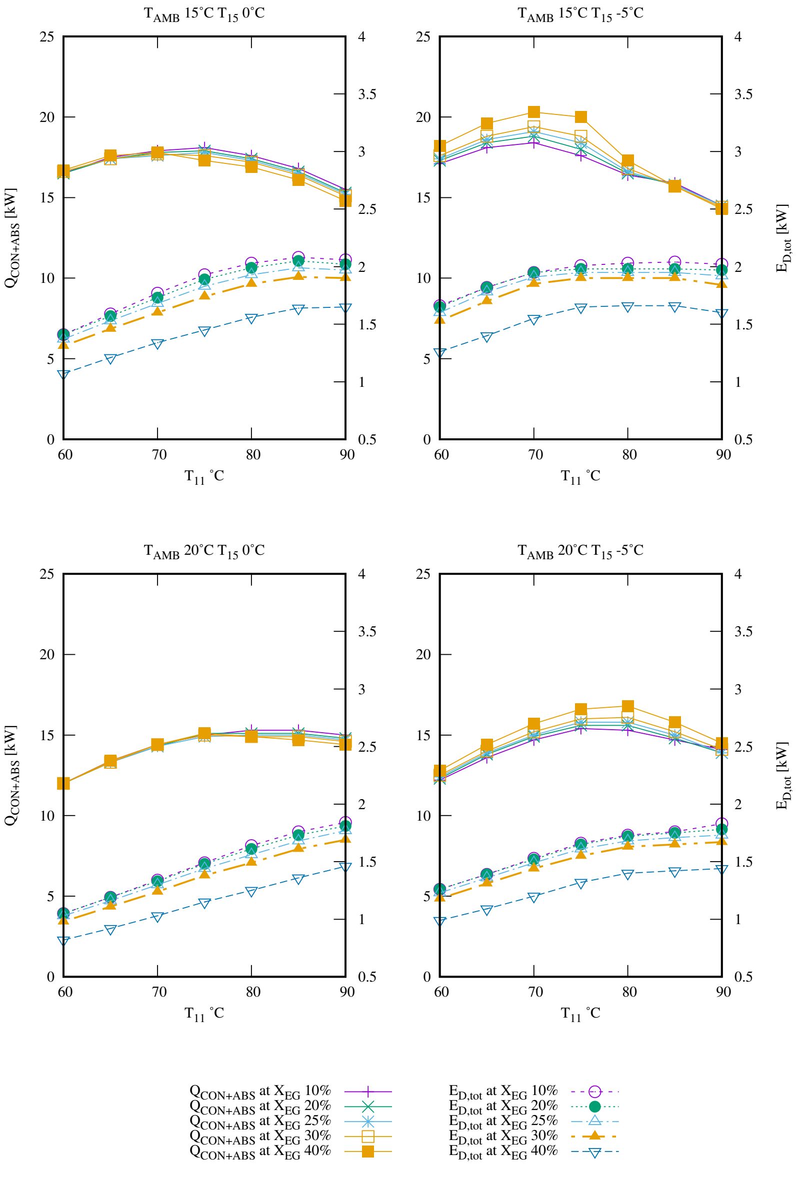

Figure 5.8: Numerical result of heat capacity ($Q_{\mathrm{ABS+CON}}$), exergy destruction rate ($E_{\mathrm{D,tot}}$) in Carrol-EG/H_2O system against heat source temperature T_{11} at different ambient temperature (T_{AMB}), evaporator secondary inlet temperature (T_{15}) and EG mass concentration in evaporator (C_{EG})

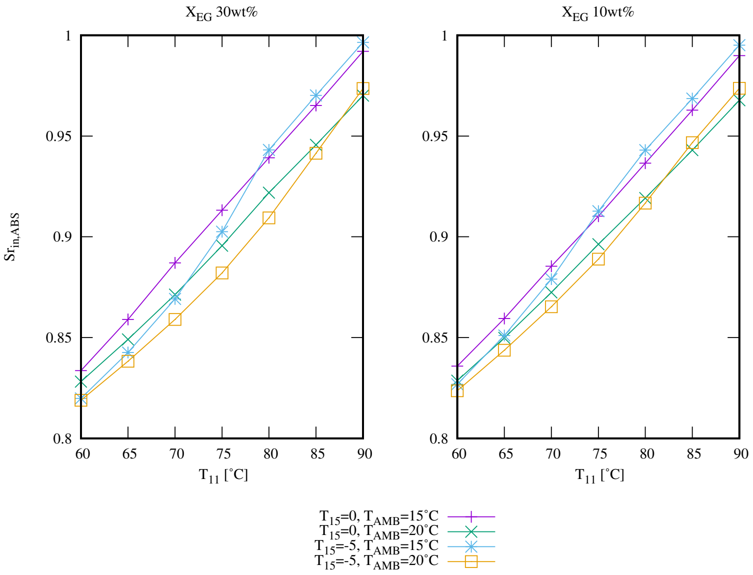

Figure 5.9: Solution saturation rate of Carrol-EG/H_2O system in heat pump mode at absorber inlet against heat source temperature T_{11}, and the saturation rate is $C_8/C_{8,\mathrm{MAX}}$.

in the evaporator may encounter the freezing problem at low pressure, as shown in Figure 5.10, T_{15} will significantly decrease the evaporator temperature. When T_{15} is 0°C, the evaporator temperature will be around -5°C, where a 20% of ethylene glycol could avoid the freezing problem, and if T_{15} is -5°C, the evaporator temperature will decrease to around -10°C, where a 30% EG solution should be used to avoid freezing, The bold solid curve represents the freezing line of the liquid and the points below the curve means the liquid will face a freezing problem. Figure 5.7,5.8 present that the EG concentration will not affect the system performance or the crystallization risk much and will improve the COP_{EX}. This aspect is due to the small difference of the U_{int}. However, it is not recommended to use higher concentrations of EG solution. One important reason is that low pressure in the evaporator will make the vacuum limit more sensitive, resulting in more expensive equipment and higher maintenance cost. The other reason is that a high EG concentration may reduce total mass and heat transfer in the evaporator due to its high viscosity.

5.3.3 Dynamic simulation of Carrol-H_2O working pair at heat pump mode

For heat pump mode, similar test campaigns are carried out with the working pair Carrol-H_2O, adding EG to the evaporator to avoid the freezing problem. Figure 5.11 shows the numerical results of the test campaign, and in this test, the evaporator secondary circuit is considered to operate under ambient conditions, so the evaporator secondary circuit inlet temperature is around ambient temperature. The indoor temperature is set as 20°C, the T_{AMB} = 0°C, and -5°C is the typical limit winter temperature for Barcelona and Madrid, respectively. The results demonstrate that at a lower chilled water inlet, at the heat pump mode, both COP and heating capacity decrease, and the crystallization risk increases. As the heat capacity of the absorption heat pump is the sum of heat rejected from the condenser and absorber (Q_{CON}+Q_{ABS}), the evolution along with time is not very sensitive to the heat source temperature. However, the absorption pump has an optimum performance at 75-80°C in term of COP and heating capacity.

5.4 Conclusions

The numerical results of an absorption system in the cooling and heating application are shown in this chapter at variable external conditions. In the chiller mode, the Carrol system has around 6−10% higher COP and 5% higher COP_{EX} than the LiBr system at

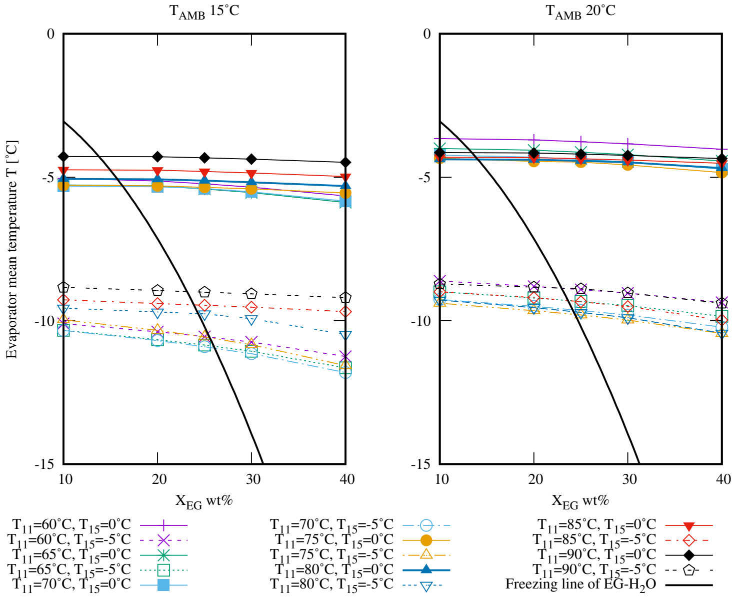

.

Figure 5.10: Freezing line of Carrol-EG/H_2O system and mean liquid temperature in the evaporator which is extracted from the code at different ambient temperature (T_{AMB}), evaporator secondary inlet temperature (T_{15}) and EG mass concentration in evaporator (C_{EG}).

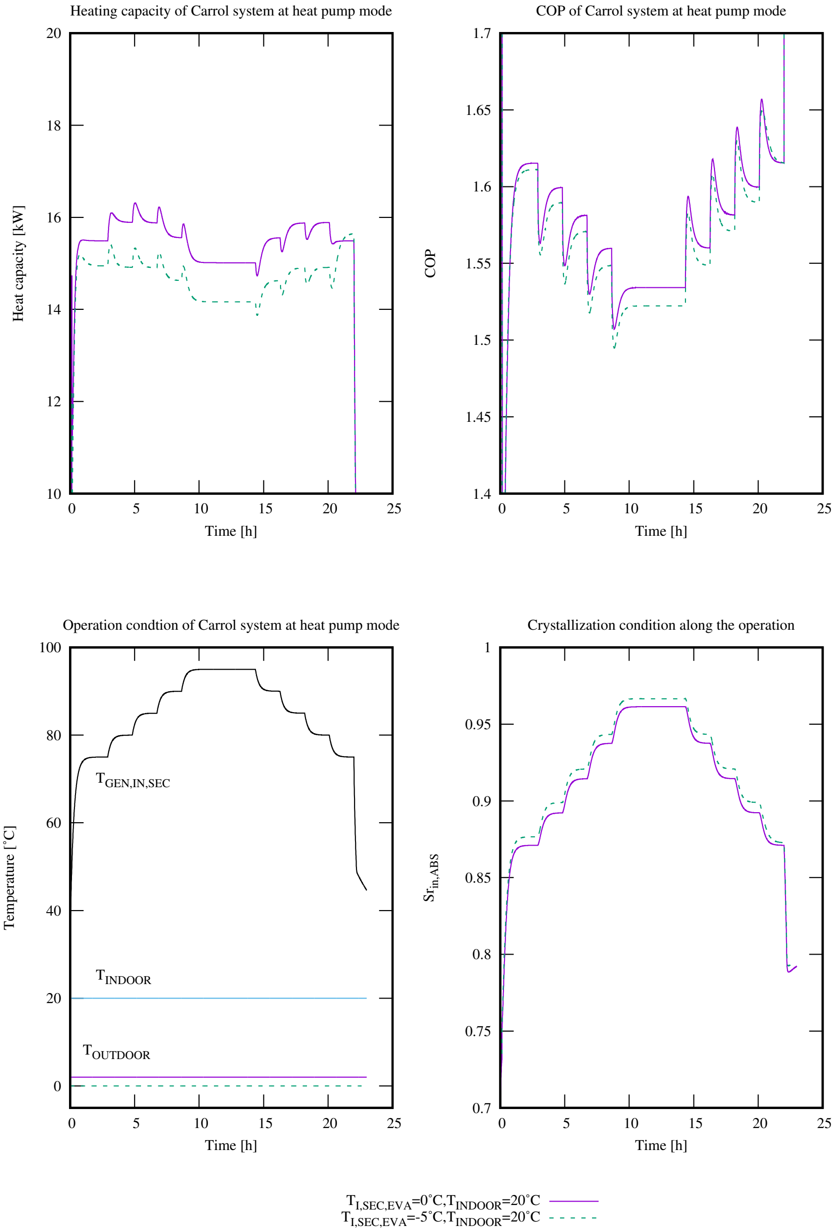

Figure 5.11: Absorption system dynamic numerical results at heat pump application with two wroking pairs LiBr-H_2O and Carrol-H_2O. Evolution of COP and capacity respect transient external conditions: generator secondary circuit inlet temperature ($T_{\mathrm{GEN,IN,SEC}}$), ambient temperature (T_{AMB}), and saturation rate of absorber inlet solution concentration (C))

the same condition, while the total cooling capacity is only 80% of LiBr system. Although lower crystallization risk means that the Carrol-H_2O system could be operated into an extended working range, the improvement is limited by the decrease of heat and mass transfer coefficients compared with the LiBr-H_2O system. On the other hand, when EG is introduced in the Carrol system, the air-sourced heat pump application could overcome the freezing limit in the evaporator. High heat source temperatures will not always lead to a higher heat capacity in the studied operating range: the heat capacity will increase, reach a maximum value, and decrease along with the heat source temperature at a certain operating condition. Meanwhile, both COP and COP_{EX} will decrease. Hence it can be stated that an optimal heat source temperature at the absorption heat pump could lead to optmize the energy costs. When T_{AMB} = 20°C, an optimum heat source temperature will be around 75-80°C, and the recommended EG mass concentration is 30%, the system heat capacity is around 15kW at a COP 1.5, COP_{EX} 1.0 and $E_{\mathrm{D,tot}}$ 2.75kW.

Nomenclature

Name	**Description**
C	Concentration [-]
$C\mathrm{p}$	Specific heat capacity $[\mathrm{J}\cdot(\mathrm{kg}\cdot\mathrm{K})^{-1}]$
C_d	Discharge coefficient [-]
COP	Coefficient of performance [-]
D	Mass diffusivity $[\mathrm{m}^2\cdot\mathrm{s}^{-1}]$
e	Specific exergy $[\mathrm{J}\cdot\mathrm{kg}^{-1}]$
E	Exergy destruction rate $[\mathrm{kJ}\cdot\mathrm{kg}^{-1}]$
h	Specific enthalpy $[\mathrm{J}\cdot\mathrm{kg}^{-1}]$
H	Height [m]
$\dot{m}$	Mass flux $[\mathrm{kg}\cdot\mathrm{s}^{-1}]$
M	Mass [kg]
P	Pressure [Pa]
Q	Heat flux [W]
R	Gas constant $[\mathrm{J}\cdot(\mathrm{kg}\cdot\mathrm{K})^{-1}]$
Re	Reynolds number $[4\Gamma/\mu]$
s	Specific entropy $[\mathrm{J}\cdot(\mathrm{kg}\cdot\mathrm{K})^{-1}]$
S	Cross section $[\mathrm{m}^2]$
Sr	Saturation rate [-]
t	Time [s]
T	Temperature [°C]
V	Volume $[\mathrm{m}^{-3}]$
W	Pump work [W]
z	Liquid height [m]
Greek letter	**Description**
α	Heat transfer coefficient $[\mathrm{Wm}^{-2}\mathrm{K}^{-1}]$
β	Mass transfer coefficient $[\mathrm{kg}\cdot\mathrm{s}^{-1}]$
γ	Activity coefficient [-]
Γ	Mass flow rate per length $[\mathrm{kg}(\mathrm{m}\cdot\mathrm{s})^{-1}]$
δ	Mean film thickness [m]
Δ	Dimensionless film thickness [-]
ΔT_m	Logarithmic temperature difference [°C]
η	Efficiency [%]
θ	Contact angle [$\circ$]
κ	Thermal diffusivity $[\mathrm{m}\cdot\mathrm{s}^{-2}]$
λ	Thermal conductivity $[\mathrm{Wm}^{-1}\mathrm{K}^{-1}]$
Λ	Dimentionless temperature [-]
μ	Dynamic viscosity $[\mathrm{Pa}\cdot\mathrm{s}^{-1}]$
ν	Kinetic viscosity $[\mathrm{m}^2\mathrm{s}^{-1}]$

Greek letter	**Description**
ξ	Pressure loss coefficient [-]
ρ	Density [kg·m^{-3}]
σ	Surface tension [mN·m]
υ	Specific internal energy [J·kg^{-1}]
Υ	Dimensionless concentration [-]
ϕ	Volumentric concentration [-]
φ	Molar fraction [-]
Abbreviation	**Description**
EG	Ethylene glycol
MWR	Minimum wetting rate
VLE	Vapor-liquid equilibrium
wt	Weight ratio
Subscripts & Superscripts	**Description**
0	Reference point
abs	Absorbed
ABS	Absorber
AMB	Ambient
b	Bulk
ch	Chemical
cold	Cold source
CON	Condenser
dis	Chemical dissolvation
D	Destruction
ext	External side of the component
ED	Exergy destruction
EVA	Evaporator
EX	Exergy
GEN	Generator
hot	Heat source
if	Interface
in	Inlet
int	Internal side of the component
loss	Energy loss

Subscripts & Superscripts	**Description**
m	Component
nd	Second
out	Outlet
phy	Physical
pri	Primary
s	Solution
sec	Secondary stream
st	First
std	Standard chemical
SHX	Solution heat exchanger
SYS	System
tot	Total
v	Vapour

References

[1] J. Castro, J. Farnós, G. Papakokkinos, J. Zheng, C. Oliet, Transient model for the development of an air-cooled LiBr-H2O absorption chiller based on heat and mass transfer empirical correlations, International Journal of Refrigeration 120 (2020) 406–419. `doi:10.1016/j.ijrefrig.2020.08.030`.

[2] J. Zheng, J. Castro, C. Oliet, Dynamic simulations of an absorption system with different working pairs at chiller and heat pump application, in: Purdue Congress, 2021, pp. 1–10.

[3] J. Zheng, J. Castro, A. Oliva, C. Oliet, Energy and exergy analysis of an absorption system with working pairs LiBr-H2O and Carrol-H2O at applications of cooling and heating, International Journal of Refrigeration 132 (September) (2021) 156–171. `doi:10.1016/j.ijrefrig.2021.09.011`.

[4] K. A. Joudi, A. H. Lafta, Simulation of a simple absorption refrigeration system, Energy Conversion and Management 42 (13) (2001) 1575–1605. `doi:10.1016/S0196-8904(00)00155-2`.

[5] G. A. Florides, S. A. Kalogirou, S. A. Tassou, L. C. Wrobel, Design and construction of a LiBr-water absorption machine, Energy Conversion and Management 44 (15) (2003) 2483–2508. `doi:10.1016/S0196-8904(03)00006-2`.

[6] D. G. Fu, G. Poncia, Z. Lu, Implementation of an object-oriented dynamic modeling library for absorption refrigeration systems, Applied Thermal Engineering 26 (2-3) (2006) 217–225. `doi:10.1016/j.applthermaleng.2005.05.008`.

[7] M. Zinet, R. Rulliere, P. Haberschill, A numerical model for the dynamic simulation of a recirculation single-effect absorption chiller, Energy Conversion and Management 62 (2012) 51–63. `doi:10.1016/j.enconman.2012.04.007`.

[8] A. Iranmanesh, M. A. Mehrabian, Dynamic simulation of a single-effect LiBr-H2O absorption refrigeration cycle considering the effects of thermal masses, Energy and Buildings 60 (2013) 47–59. `doi:10.1016/j.enbuild.2012.12.015`.

[9] Y. jie. Xu, S. jie. Zhang, Y. han. Xiao, Y. jie Xu, S. jie Zhang, Y. han Xiao, Modeling the dynamic simulation and control of a single effect LiBr–H2O absorption chiller, Applied Thermal Engineering 107 (2016) 1183–1191. `doi:10.1016/j.applthermaleng.2016.06.043`.

[10] H. Matsushima, T. Fujii, T. Komatsu, A. Nishiguchi, Dynamic simulation program with object-oriented formulation for absorption chillers (modelling, verification, and application to triple-effect absorption chiller), International Journal of Refrigeration 33 (2) (2010) 259–268. `doi:10.1016/j.ijrefrig.2009.07.003`.

[11] S. Jeong, B. H. Kang, S. W. Karng, Dynamic simulation of an absorption heat pump for recovering low grade waste heat, Applied Thermal Engineering 18 (1-2) (1998) 1–12. `doi:10.1016/s1359-4311(97)00040-9`.

[12] P. Kohlenbach, F. Ziegler, A dynamic simulation model for transient absorption chiller performance. Part II: Numerical results and experimental verification, International Journal of Refrigeration 31 (2) (2008) 226–233. `doi:10.1016/j.ijrefrig.2007.06.010`.

[13] G. Evola, N. Le Pierrès, F. Boudehenn, P. Papillon, Proposal and validation of a model for the dynamic simulation of a solar-assisted single-stage LiBr/water absorption chiller, International Journal of Refrigeration 36 (3) (2013) 1015–1028. `doi:10.1016/j.ijrefrig.2012.10.013`.

[14] J. Castro, A. Oliva, C. D. Perez-Segarra, C. Oliet, Modelling of the heat exchangers of a small capacity, hot water driven, air-cooled H2O-LiBr absorption cooling machine, International Journal of Refrigeration 31 (1) (2008) 75–86. `doi:10.1016/j.ijrefrig.2007.05.019`.

[15] S. Aprhornratana, I. W. Eames, Thermodynamic analysis of absorption refrigeration cycles using the second law of thermodynamics method, International Journal of Refrigeration 18 (4) (1995) 244–252. `doi:10.1016/0140-7007(95)00007-X`.

[16] M. M. Talbi, B. Agnew, Exergy analysis: An absorption refrigerator using lithium bromide and water as the working fluids, Applied Thermal Engineering 20 (7) (2000) 619–630. `doi:10.1016/S1359-4311(99)00052-6`.

[17] S. C. Kaushik, A. Arora, Energy and exergy analysis of single effect and series flow double effect water-lithium bromide absorption refrigeration systems, International Journal of Refrigeration 32 (6) (2009) 1247–1258. `doi:10.1016/j.ijrefrig.2009.01.017`.

[18] S. Samanta, D. N. Basu, Energy and Entropy-Based Optimization of a Single-Stage Water-Lithium Bromide Absorption Refrigeration System, Heat Transfer Engineering 37 (2) (2016) 232–241. `doi:10.1080/01457632.2015.1044420`.

[19] E. Bellos, C. Tzivanidis, K. A. Antonopoulos, Exergetic and energetic comparison of LiCl-H2O and LiBr-H2O working pairs in a solar absorption cooling system, Energy Conversion and Management 123 (2016) 453–461. `doi:10.1016/j.enconman.2016.06.068`.

[20] T. K. Gogoi, D. Konwar, Exergy analysis of a H2O-LiCl absorption refrigeration system with operating temperatures estimated through inverse analysis, Energy Conversion and Management 110 (2016) 436–447. `doi:10.1016/j.enconman.2015.12.037`.

[21] A. Lake, B. Rezaie, S. Beyerlein, Use of exergy analysis to quantify the effect of lithium bromide concentration in an absorption chiller, Entropy 19 (4). `doi:10.3390/e19040156`.

[22] M. Izquierdo, S. Aroca, Lithium bromide hightemperature absorption heat pump: Coefficient of performance and exergetic efficiency, International Journal of Energy Research 14 (3) (1990) 281–291. `doi:10.1002/er.4440140304`.

[23] C. heng, Y. hih, Exergy and energy analyses of absorption heat pumps, International Journal of Energy Research 12 (2) (1988) 189–203. `doi:10.1002/er.4440120202`.

[24] S. F. Lee, S. A. Sherif, Thermodynamic analysis of a lithium bromide/water absorption system for cooling and heating applications, International Journal of Energy Research 25 (11) (2001) 1019–1031. `doi:10.1002/er.738`.

[25] A. Şencan, K. A. Yakut, S. A. Kalogirou, Exergy analysis of lithium bromide/water absorption systems, Renewable Energy 30 (5) (2005) 645–657. `doi:10.1016/j.renene.2004.07.006`.

[26] W. Rivera, R. J. Romero, M. J. Cardoso, J. Aguillón, R. Best, Theoretical and experimental comparison of the performance of a single-stage heat transformer operating with water/lithium bromide and water/Carrol ™, International Journal of Energy Research 26 (8) (2002) 747–762. `doi:10.1002/er.813`.

[27] R. J. Romero, A. R. Martínez, S. Silva, J. Cerezo, W. Rivera, Comparison of double stage heat transformer with double absorption heat transformer operating with Carrol - Water for industrial waste heat recovery, Chemical Engineering Transactions 25 (2011) 129–134. `doi:10.3303/CET1125022`.

[28] J. Ibarra-Bahena, R. J. Romero, J. Cerezo, C. V. Valdez-Morales, Y. R. Galindo-Luna, L. Velazquez-Avelar, Experimental assessment of an absorption heat transformer prototype at different temperature levels into generator and into evaporator operating with water/Carrol mixture, Experimental Thermal and Fluid Science 60 (2015) 275–283. `doi:10.1016/j.expthermflusci.2014.09.013`.

[29] E. D. Kerme, A. Chafidz, O. P. Agboola, J. Orfi, A. H. Fakeeha, A. S. Al-Fatesh, Energetic and exergetic analysis of solar-powered lithium bromide-water absorption cooling system, Journal of Cleaner Production 151 (2017) 60–73. `doi:10.1016/j.jclepro.2017.03.060`.

[30] R. Palacios-Bereche, R. Gonzales, S. A. Nebra, Exergy calculation of lithium bromide-water solution and its application in the exergetic evaluation of absorption refrigeration systems LiBr-H2O, International Journal of Energy Research 36 (2) (2012) 166–181. `doi:10.1002/er.1790`.

[31] W. J. Koehler, W. E. Ibele, Availability simulation of a lithium bromide absorption heat pump, Heat Recovery Systems & ClIP 8 (2) (1988) 157–171.

[32] K. I. Stepanov, D. G. Mukhin, S. V. Alekseenko, O. V. Volkova, Experimental study of negative temperatures in lithium-bromide absorption refrigerating machines, Thermophysics and Aeromechanics 22 (4) (2015) 481–489. `doi:10.1134/S0869864315040095`.

[33] A. Oliva, C. D. Pérez-Segarra, J. Rigola, J. Castro, I. Rodríguez, O. Lehmkuhl, X. Trias, C. R., R. Alba, M. Ordoño, J. Farnós, Machine for air-cooled absorption, uS Patent 10,527,324 (2020).

[34] J. Castro, A. Oliva, C. D. Pérez-Segarra, J. Cadafalch, Evaluation of a small capacity, hot water driven, air-cooled H2O-LiBr absorption machine, HVAC and R Research 13 (1) (2007) 59–75. `doi:10.1080/10789669.2007.10390944`.

[35] T. Avanessian, M. Ameri, Energy, exergy, and economic analysis of single and double effect LiBr-H2O absorption chillers, Energy and Buildings 73 (2014) 26–36. `doi:10.1016/j.enbuild.2014.01.013`.

[36] J. Ziegler, N. Nichols, Optimum settings for PID controllers, Transactions of ASME 64 (1942) 759–768.

[37] K. E. Herold, R. Radermacher, S. A. Klein, Absorption chillers and heat pumps, CRC press, 2016.

6

Numerical studies of the heat & mass transfer enhancement influence on absorption machine's performance

ABSTRACT

In this chapter, an air-cooled, single-effect solar-driven absorption system is evaluated considering the thermal characteristics enhancement. The enhancements affect the working pairs and components' properties like surface tension, contact angle, minimum wetting rate (MWR), and thermal conductivity. Surfactants are employed to strengthen the Marangoni effect, hydrophilic treatment is used on the absorber to improve wettability, nanofluids of working pairs are made to increase thermal conductivity, and mechanical vibration is also considered to enhance mass transfer. The data of the properties are extracted from previous sections or other references in terms of the enhancement characteristics. According to simulations the thermal conductivity could increase from 5 to 20% with nanoparticle enhancement. This improvement lead to increase the working capacity of the absorption system by around 5% for the same operating condition. On the other hand, with the enhancement of surfactants, the working capacity could increase by around 10%, and finally, applying vibrations to the absorber, the improvement is around 5%. In general, in a limited range of current thermodynamic enhancement methods, all the enhancements attribute a higher working capacity, slightly higher COP, and COP_{ex}, while the exergy destruction almost

remains the same since the energy input will barely change. The dynamic simulation of the absorption system in heating and cooling application was reported in [1], the steady-state simulation was reported in [2], and the performance enhancement was reported in [3].

6.1 Introduction of enhancements to absorption system simulation

There are several methods to enhance the performance of the absorption system actuating of the heat and mass transfer, such as: i) strengthening the Marangoni effect in the vertical falling film by adding surfactants to the working pairs; ii) using specific treatment materials inside the components to acquire better wettability or larger liquid-solid contact area; iii) changing working pairs to binary nanofluid with nanoparticles to increase the thermal conductivity; iv) applying multiphysical fields to the falling film process to enhance the heat and mass transfer performance, such as mechanical vibration. Cheng et al. [4] used 1−Octanol, 2−EH to increase the heat and mass transfer coefficients in a vertical falling film absorption with working pairs $LiBr-H_2O$ experimentally and proposed an empirical equation to describe the relationship of surfactant and heat transfer. Besides, Sun et al. [5] did an experimental study on vertical vapour absorption into LiBr solution with and without additive with 90ppm of 2−EH and found that the mass transfer coefficient could increase around two times. Also, Zhang et al. [6] did an experimental investigation of a horizontal falling film with different types of tubes and surfactants and found that the surfactant 2−EH is superior to 1−Octanol in terms of heat and mass transfer enhancement. Also, the surfactants have a more significant effect than tube surface geometry in heat and mass transfer. The surfactant has an optimum mass fraction range of 80−160ppm, and this value may increase with the solution flow rate. Miller and Perez-Blanco [7] used advanced surface tubes in a vertical falling film, obtaining better performance in heat transfer with an improvement in the range of 175−300% respect tubes with smooth surface. Kim et al. [8] used the hydrophilic surface treatment outside copper tubes in a horizontal falling film and found that the heat transfer coefficient in evaporation improved 2−3 times. In terms of the nanofluid, Gao et al. [9] used software COMSOL to establish the model of falling film absorption considering the thermodynamic properties enhancement with nanofluids. The results confirm the existence of an optimum film flow rate, and after adding copper oxide nanoparticles, both mass transfer rate and coefficient are increased. In terms of the absorber material or structure, Since additives will only stand in a small quantity in the working pairs, the other properties like density, viscosity, mass diffusivity, and specific heat capacity will not significantly change. Unlike surfactants, nanoparticles are solid particles with a diameter of 10−100nm, and the particles are generally not soluble in the working pairs. If a stable suspension of nanoparticles is achieved, the fluid pairs absorbent-refrigerant are converted to nanofluid . The nanoparticles typically have a much larger thermal conductivity and will eventually increase the thermal conductivity of the working fluids. Kang et al. [10] used LiBr−H_2O solution with nanoparticles of Fe and Carbon nanotubes (CNT) in a falling film and found that the vapour absorption rates of the nanofluids are 1.29−2.2 and 1.35−2.5 times higher than that for the base fluid for 0.01% and 0.1wt%, respectively. Also, Wang et al. [11] used LiBr−H_2O nanofluid with CuO nanoparticles with 0.05% and 0.1vol% at flow rate 1.0L·min^{-1} and found the mass transfer coefficient increased by 1.28 and 1.41 times, respectively. Moreover, Tsuda et al. [12] conducted an experimental study on the effect of vibration on falling film, which showed that vibration can enhance heat and mass transfer. However, the optimal frequency, wavelength, and other characteristics of the mechanical vibration vary according to the Reynolds number (Re), making the phenomenon quite complex. The study observed that different optimum frequencies and displacements are required for different Re numbers. Based on the experimental results, at Re = 300, with a mechanical vibration amplitude of 1 mm, the optimum vibration frequency was around 60 Hz, which increased the absorbed mass flux by 100%.

In Chapter 4, the simulations demonstrated that heat transfer coefficient of nanofluid of Al_2O_3 ($\phi = 0.5\%$) with H_2O, LiBr solution, Carrol solution increased 10-20%. And for the absorption falling film with LiBr-H_2O or Carrol-H_2O, the heat transfer coefficient or the mass transfer rate have also increased around 10%-15% with the same nanofluid.

In the present chapter, an air-cooled absorption machine is under analysis based on the first and second laws of thermodynamics in both chiller and heat pump applications, using the in-house object-oriented numerical platform NEST [13]. The simulation system was described in Chapter 5 and the assumptions remain the same. The heat source temperature varies in the range of 70−90°C, and the chilled water temperature has been set in two values, 9°C and 14°C for the chiller application. In the chiller application, two working pairs, LiBr-H_2O and Carrol-H_2O, are simulated taking into account superhydrophilic treatment to the absorber, surfactants, and nanofluid.

6.2 Results of the performance enhancement

6.2.1 Effect of surfactants

Surfactants could help enhance the Marangoni effect in the vertical falling film process, increasing the heat and mass transfer coefficients enhancement. The enhancement factor was extracted from Zhang et al. [6], and it was calculated with Equation 6.1. All these enhancements have been implemented in the cycle simulation. The detailed information for the surface tension with surfactant was reported in Chapter 2.

$$K = n_0 Re^{n_1} \left[\left(\frac{\mathrm{d}\sigma}{\mathrm{d}C_\mathrm{b}} \right)_\mathrm{i} \right]^{n_2} \left[\frac{f_1 C_\mathrm{A} (\sigma_0 - \sigma_\mathrm{c})}{(1+f_1 C_\mathrm{A})^2} \right]_3^{n} \left(\frac{f_1}{1+f_1 C_\mathrm{A}} \right)^{n_4} \left(\frac{f_1 f_2^{0.5}}{1+f_1 C_\mathrm{A}} \right)^{n_5} \tag{6.1}$$

Where the K represents the enhancement factor for Nu number, is defined as $K = (Nu - Nu_0)/Nu_0$, C_b represents the bulk concentration of the additive in aqueous solution, C_g represents the relative mass concentrations of additive in the gas side, C_b represents the bulk concentration of water in aqueous solution, σ_0 is the surface tension without additive, and σ_c is the critical surface tension with additive. The $n_0, n_1, n_2, n_3, n_4, n_5$ are correlated with experimental results, $n_0 = 5.1$, $n_1 = -1.03$, $n_2 = 1.7$, $n_3 = 2.7$, $n_4 = -3.8$, $n_5 = 1.9$. and other parameters of surface tension are listed in Table 6.1. Simulation results considering the enhancement due to surfactants are shown in table 6.2. In this table, several variables are represented: i) the concentration of the mass fraction of surfactant in the working pairs; ii) C_8, the concentration at the absorber inlet; iii) T_8, the solution temperature; iv) U_int, the internal heat transfer coefficient; v) β, the mass transfer coefficient in the absorber; vi) Q_output, the cooling capacity of the evaporator; vii) $E_\mathrm{D,sys}$, the exergy destruction rate for the absorption system. The working capacity of LiBr and Carrol could increase by 3.2 – 7.8% and 4.8 – 13.1%, respectively. The working pair Carrol$-H_2O$ is more sensitive to the enhancement, and all the cases will not significantly change the COP, COP_EX, and $E_\mathrm{D,sys}$.

Table 6.1: Parameters of surface tension in Cheng et al. [4]

Additive	f_1	f_2 [s^{-1}]	$\sigma_0 - \sigma_c$[$\mathrm{mN \cdot m^{-1}}$]	$\frac{\mathrm{d}\sigma_e}{\mathrm{d}C_\mathrm{w}}$[$\mathrm{mN \cdot m^{-1}}$]
1-octanol	8.0E4	1.3E-5	69.4	0.45
2-EH 5	8.3E4	0.67E-5	59.4	0.80

Table 6.2: Thermophysical charteristics of absorption system with and without surfactants

Additive	Reference	Concentration [ppm]	C_8 [-]	T_8 [°C]	COP [-]	COP_{ex} [-]	U_{int} $[\text{W}(\text{m}^2 \cdot K)^{-1}]$	β $[\text{g}(\text{m}^2 \cdot s)^{-1}]$	Q_{output} [kW]	$E_{\text{D,sys}}$ kW
LiBr Morison2006	-	0	0.582	43.57	0.747	0.448	749	5.93E-5	6.49	1.37
LiBr with 2EH	[4]	100	0.563	38.80	0.749	0.466	1510	5.92E-5	6.69	1.39
LiBr with 2EH	[5]	100	0.564	39.3	0.751	0.466	757	1.21E-4	6.66	1.39
LiBr with 2EH	[6]	150	0.560	38.9	0.757	0.475	1531	3.67E-4	6.99	1.41
Carrol Morison2006	-	0	0.634	39.2	0.774	0.462	554	2.78E-5	5.34	1.14
Carrol with PMC	[4]	1000	0.631	38.4	0.775	0.466	1125	3.16E-5	5.59	1.16
Carrol with PMC	[5]	1000	0.630	39.4	0.779	0.469	571	6.54E-5	5.64	1.17
Carrol with PMC	[6]	1500	0.623	38.8	0.757	0.475	1174	2.05E-4	6.04	1.20

6.2.2 Surface treatment

The model from Morison et al. [14] for wettability is considered in the NEST model. According to the correlation in [14], as shown in Equation 6.2, the wettability is mainly affected by the contact angle, surface tension, density, and viscosity. Moreover, it is possible to improve the wettability through a hydrophilic coating method mentioned in Ye et al. [15]. Superhydrophilic coating to the material could reduce the contact angle to 0.2 rad or lower, resulting in a dominant correlation role. Compared with other criteria like Mikielewicz and Moszynski [16], the model from [14] could predict wettability for a low contact angle condition, as shown in Equation 6.2.

$$\Gamma = 0.13(1-\cos\theta)^{0.764}\sigma^{0.764}\rho^{0.255}\mu^{-0.018} \tag{6.2}$$

When the hydrophilic surface treatment is applied to the absorber, the coating could significantly increase the contacting area and the wettability. In the wetting theory of Mikielewicz and Moszynski [16], the rupture into rivulets is assumed to occur when both the contimuous film and the rivulets carry the same mass flow and total energy, hence the wetting are could be calculated. Meanwhile, for an annular film, a dry-patch model was developed by Morison et al. [14], and the model was validated in the Chapter 3. For the same volumetric flow rate at 5.76E-6 $\text{m}^3 \cdot \text{s}^{-1}$, with the model from [14], the Q_{EVA} increased from 4.0 to 4.8 kW compared with the model from [16], and COP increased from 0.74 to 0.76 and COP_{EX} from 0.45 to 0.51 using Carrol-H_2O as wokring pairs.

The minimum wetting rate (MWR) could be reduced to 0.02 $\text{kg}(\text{m} \cdot \text{s})^{-1}$, which could guarantee the total wettability and could also reduce the working pairs load to the machine. For the proposed design of the absorption machine from Castro et al. [13], the loaded working pairs could be reduced from 10 L to 5 L for both working pairs when maintaining the same working capacity and similar COP, COP_{EX}.

6.2.3 Effect of nanoparticles

The thermophysical properties of the working fluid pairs, such as density, viscosity, and thermal conductivity, will change with the presence of nanoparticles. However, the effect on the density and viscosity is neglectable because the volume fraction of the nanofluid is generally a tiny amount. Here the enhancement ratio of thermal conductivity is considered the main variable $\lambda_{\text{nano}}/\lambda_0$. Some experimental data of enhancement ratio is shown in Table 6.3.

Table 6.3: Results of nanofluid

Ref	Nano particle	Liquid	Volume fraction [%]	λ_{np}W[(m·K)$^{-1}$]	$\frac{\lambda_{\text{nano}}}{\lambda_0}$
[17]	Al_2O_3	EG	6	40	1.24
[17]	CuO	Water	6	76	2.0
[18]	Cu	Water	0.3	400	1.75

The temperature and concentration distribution were demonstrated in Chapter 4. Also, the heat coefficient of the whole falling film is shown in Figure 6.1. In the result, the increase of λ could accelerate the temperature decrease along with the falling film length, which could contribute to the design of a compact absorption system. And the higher the thermal conductivity the solution has, the higher the heat transfer coefficient it will obtain. In Figure 6.1, the results show that the thermal conductivity enhancement has a stronger effect on the Carrol solution than on the LiBr solution in film heat transfer coeffcient. On the other hand, when the assessment of enhancement of thermal conductivity is carried out with NEST for system simulation using an empirical correlation that uses only the parameters of the whole domain of the absorber, the results are shown in Figure 6.1. With the empirical correlation, the heat transfer coefficient in the absorber has the same tendency as the heat transfer coefficient of the falling film simulation, and the two working pairs have similar behaviour. However, from a quantitative point of view, it can be observed that the enhancement ratio calculated through the falling film numerical model is smaller than the NEST empirical model. In contrast, the pressure, mass flow, and wall temperature are all fixed in the falling film model. The heat transfer coefficient represents the heat transfer capacity alongside the film length, where the temperature and concentration vary from the inlet to equilibrium. As shown in Figure 4.19 in Chapter 4, the temperature decreases faster with a higher thermal conductivity; thus, the enhancement will mainly affect the initial region in the falling film. Consequently, the heat transfer coefficient enhancement in the falling film

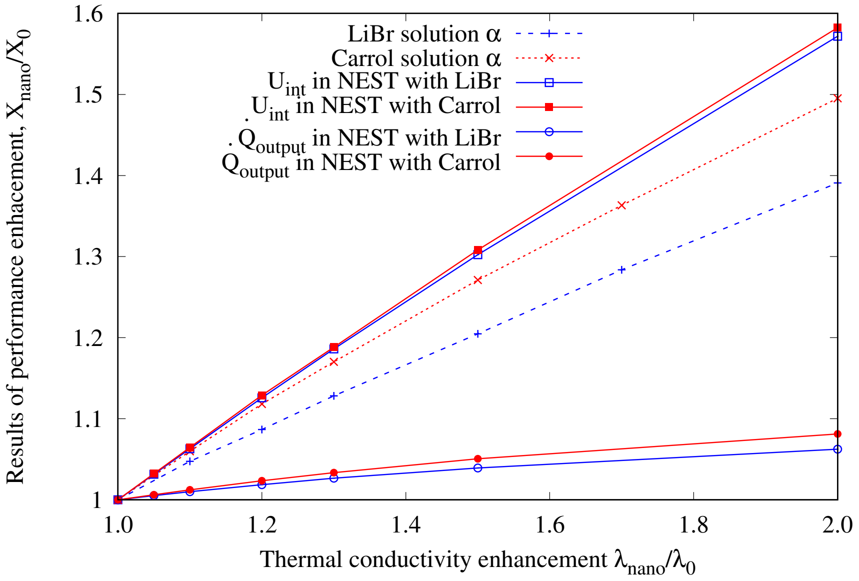

Figure 6.1: Results of performance enhancement of thermal conductivity, the X represents the parameter enhanced X_{nano} is the enhanced factor, and X_0 is the original value. In which α is the heat transfer coefficient for the falling film, $\alpha = \frac{Q}{\Delta TL}$, U_{int} is the heat transfer coefficient in the absorber, and Q_{output} is the output energy in the system, in absorption chiller Q_{output} equal to evaporator working capacity.

simulation is lower than for the prediction of NEST based on empirical correlations. As shown in Figure 6.1, when the thermal conductivity increases by 20%, the LiBr and Carrol solution heat transfer coefficient increases by 10% and 9%, meanwhile the value in the NEST increases 10.5% for both solutions.

6.2.4 Effect of vibration

A vibrating screen is employed in Tsuda et al. [12] to enhance the vertical falling film absorption. The results in the literature of absorbed mass flux optimization with amplitude at 0.2 mm at different frequencies are shown in Table 6.4. In the literature [12], the liquid solution falling film pass above a vibrating screen and the mass flux due to the absorption will change according to the vibration frequency and Re number of the inlet solution. The results in the Table 6.4 demonstrated the enhancement of vibration to mass transfer at different Re and frecuencies. A parameter for mass transfer coefficient was introduced to NEST to complement the enhancement factor of vibration according to the results. For example, if the $Re = 100$ at the absorber inlet, the vapour mass transfer coefficient will be 1.131 times higher.

Table 6.4: Results of enhancement of vibration extracted from Tsuda et al. [12]

Re	Frequency [Hz]	Mass flux absorbed before and after vibration $[\mathrm{kg}(\mathrm{hr}\cdot\mathrm{m}^2)^{-1}]$	$\frac{\dot{m}_{\mathrm{abs,vibration}}}{\dot{m}_{\mathrm{abs,0}}}$
20	40	3.68 – 5.34	1.45
40	40	4.13 – 7.41	1.794
60	40	5.27 – 7.15	1.113
80	60	5.92 – 6.59	1.188
100	100	6.48 – 7.33	1.131
200	60	5.42 – 5.77	1.065
300	100	4.74 – 6.06	1.278

6.3 Enhancement combined advantages and disadvantages

Multiple enhancement strategies for the heat and mass transfer absorption processes could be applied to a small-capacity absorption system. Meanwhile, all the enhancements have disadvantages considering operation conditions, varying thermophysical parameters, and final cost. The advantages are mainly the improved heat and mass transfer, leading to higher performance. And in terms of the disadvantages, different methods may introduce various weaknesses to the absorption system. The ideal results are listed in Table 6.5, in which the enhancement ratio is extracted with the simulation results explained in the previous chapters. The surfactants need replenishment in the solution circle from time to time. Also, there are difficulties in determining the concentration of the surfactants in the system. For the nanofluid, the nanoparticles suspended in the solution may not be stable for an extended period. Moreover, the particles' sediment may cause other problems, such as damage to the pump. Besides, if the vibration is applied to an absorption system, it may introduce leak risk in the long term since the system works under a high vacuum. Also, for the vibration introduced to the absorption system, in this work, the enhancement is only considered for the absorption process in the absorber. If the vibration is introduced to the whole system, its enhancement effect on pool boiling, and the horizontal falling film should also be considered to acquire a more realistic working condition. Besides, according to the results in the Table 6.5, the enhancement was only considered in the absorber hence the final output work does not improve significantly as the heat and mass transfer coefficient in the absorber. In general, enhancement could significantly improve the working performance of the absorption system and the reliability should be taken into consideration.

Table 6.5: Thermophysical characteristics of absorption system with ideal enhancements

Enhancement	$\frac{U_{\mathrm{int}}}{U_0}$		$\frac{Q_{\mathrm{output}}}{Q_0}$		Disadvantages
	LiBr	Carrol	LiBr	Carrol	
Surfactant	204%	212%	108%	113%	Need replenishment for surfactant
Nanofluid	130%	130%	104%	106%	Nanoparticles may precipitate and form sediment
Vibration	130%	140%	103%	104%	Vibration distribution not uniform and may introduce leak risk to the absorption system

6.4 Conclusion

Several modified parameters are introduced in numerical simulations to investigate the performance enhancement of an absorption system in a different way. The first parameter investigated is wettability in the absorber, which is critical to the total performance of the absorption machine. If a hydrophilic coating is introduced, the wettability can be increased from 0.44 to 1.0, therefore the working capacity of LiBr and Carrol could increase 10%, and 20%, respectively. Adding surfactants to the working pairs could reduce surface tension and strengthen the Marangoni effect, improving the heat and mass transfer effect. With surfactant 2−EH in the system under the same operating condition, the working capacity could increase by 3.2 – 7.8%, 4.8 – 13.1% for LiBr and Carrol working pairs, respectively. Meanwhile the COP, COP_{EX}, ED_{sys} stays at the same level. In a similar way to surfactants, the nanofluid could also change the thermophysical properties of working pairs by increasing thermal conductivity. The pressence of nanofluid will improve the heat transfer coefficient of the absorber by 30% for both working pairs, and the working capacity will increase by around 5%. Besides, the vibration could also help to improve the working performance and has a similar effect to nanofluid. Also, all these enhancements could be applied to the same system simultaneously. The simulation may not predict the final performance since the enhancements may interfere with each other somehow. Experimental works are necessary in the future to consolidate the multiple enhancements in the same system.

Nomenclature

Name	**Description**
C	Concentration
COP	Coefficient of performance [-]
E	Exergy destruction rate [kJ·kg^{-1}]
f_1, f_2	Coefficients for additivesEquation 6.1 [-]
K	Enhanced ratio of Nu [-]
L	Length
$n_0, n_1, n_2, n_3, n_4, n_5$	Coefficients Equation 6.1
Nu	Nusselt number$\alpha \cdot L/\lambda$
Q	Heat flux [kW]
Re	Reynolds number$4\Gamma/\mu$
T	Temperature [°C]
U	Heat transfer coefficient [W·K^{-1}]
X	Variable [-]
Greek letter	**Description**
α	Heat transfer coefficient [Wm^{-2}K^{-1}]
β	Mass transfer coefficient [kg·s^{-1}]
Γ	Mass flow rate per length [kg(m·s)$^{-1}$]
η	Efficiency [%]
θ	Contact angle [$\circ$]
λ	Thermal conductivity [Wm^{-1}K^{-1}]
μ	Dynamic viscosity [Pa·s^{-1}]
ν	Kinetic viscosity [m^{2}s^{-1}]
ρ	Density [kg·m^{-3}]
σ	Surface tension [mN·m]
ϕ	Volumentric concentration [-]
Abbreviation	**Description**
2-EH	2-Ethylhexanol
CNT	Carbon nanotubes
EG	Ethylene glycol
MWR	Minimum wetting rate
PMC	Phenylmethylcarbinol, 1−Phenylethanol
VLE	Vapor-liquid equilibrium
wt	Weight ratio

Subscripts & Superscripts	**Description**
0	Reference point
A	Additive
AMB	Ambient
EX	Exergy
abs	Absorbed
b	Bulk
c	Critical
g	Gas phase
int	Interior
nano	Nanofluid
np	Nanoparticle
output	Output
sys	System
vibration	Mechanical vibration
w	Water

References

[1] J. Zheng, J. Castro, C. Oliet, Dynamic simulations of an absorption system with different working pairs at chiller and heat pump application, in: Purdue Congress, 2021, pp. 1–10.

[2] J. Zheng, J. Castro, A. Oliva, C. Oliet, Energy and exergy analysis of an absorption system with working pairs LiBr-H2O and Carrol-H2O at applications of cooling and heating, International Journal of Refrigeration 132 (September) (2021) 156–171. `doi:10.1016/j.ijrefrig.2021.09.011`.

[3] J. Zheng, J. Castro, G. Papakokkinos, A. Oliva, Sensitivity study to an absorption system performance considering heat and mass transfer enhancements, in: Purdue Congress, 2022.

[4] W. L. Cheng, K. Houda, Z. S. Chen, A. Akisawa, P. Hu, T. Kashiwagi, Heat transfer enhancement by additive in vertical falling film absorption of H2O/LiBr, Applied Thermal Engineering 24 (2-3) (2004) 281–298. `doi:10.1016/j.applthermaleng.2003.08.013`.

[5] F. Lin, S. Jian, Z. Shigang, Experimental study on vertical vapor absorption into LiBr solution with and without additive, Applied Thermal Engineering 31 (14-15) (2011) 2850–2854. `doi:10.1016/j.applthermaleng.2011.05.010`.

[6] H. Zhang, D. Yin, S. You, W. Zheng, S. Wei, Experimental investigation of heat and mass transfer in a LiBr-H2O solution falling film absorber on horizontal tubes: Comprehensive effects of tube types and surfactants, Applied Thermal Engineering 146 (2019) 203–211. `doi:10.1016/j.applthermaleng.2018.09.127`.

[7] W. A. Miller, H. Perez-Blanco, Vertical-tube aqueous LiBr falling film absorption using advanced surfaces, Tech. rep. (1993).

[8] H. Y. Kim, B. H. Kang, Effects of hydrophilic surface treatment on evaporation heat transfer at the outside wall of horizontal tubes, Applied Thermal Engineering 23 (4) (2003) 449–458. `doi:10.1016/S1359-4311(02)00211-9`.

[9] H. Gao, F. Mao, Y. Song, J. Hong, Y. Yan, Effect of adding copper oxide nanoparticles on the mass/heat transfer in falling film absorption, Applied Thermal Engineering 181 (August). `doi:10.1016/j.applthermaleng.2020.115937`.

[10] Y. T. Kang, H. J. Kim, K. I. Lee, Heat and mass transfer enhancement of binary nanofluids for H2O/LiBr falling film absorption process, International Journal of Refrigeration 31 (5) (2008) 850–856. `doi:10.1016/j.ijrefrig.2007.10.008`.

[11] G. Wang, Q. Zhang, M. Zeng, R. Xu, G. Xie, W. Chu, Investigation on mass transfer characteristics of the falling film absorption of LiBr aqueous solution added with nanoparticles, International Journal of Refrigeration 89 (2018) 149–158. `doi:10.1016/j.ijrefrig.2018.01.017`.

[12] H. Tsuda, H. Perez-Blanco, An experimental study of a vibrating screen as means of absorption enhancement, International Journal of Heat and Mass Transfer 44 (21) (2001) 4087–4094. `doi:10.1016/S0017-9310(01)00038-2`.

[13] J. Castro, J. Farnós, G. Papakokkinos, J. Zheng, C. Oliet, Transient model for the development of an air-cooled LiBr-H2O absorption chiller based on heat and mass transfer empirical correlations, International Journal of Refrigeration 120 (2020) 406–419. `doi:10.1016/j.ijrefrig.2020.08.030`.

[14] K. R. Morison, Q. A. G. Worth, N. P. O'Dea, Minimum wetting and distribution rates in falling film evaporators, Food and Bioproducts Processing 84 (4 C) (2006) 302–310. `doi:10.1205/fbp06031`.

[15] L. Ye, Y. Zhang, C. Song, Y. Li, B. Jiang, A simple sol-gel method to prepare superhydrophilic silica coatings, Materials Letters 188 (2017) 316–318. `doi:10.1016/j.matlet.2016.09.043`.

[16] J. Mikielewicz, J. R. Moszynski, Minimum Thickness of a Liquid Film Flowing Vertically Down a Solid Surface, International Journal of Heat and Mass Transfer 19 (7) (1976) 771–776. `doi:10.1016/0017-9310(76)90130-7`.

[17] M. I. Pryazhnikov, A. V. Minakov, V. Y. Rudyak, D. V. Guzei, Thermal conductivity measurements of nanofluids, International Journal of Heat and Mass Transfer 104 (2017) 1275–1282. `doi:10.1016/j.ijheatmasstransfer.2016.09.080`.

[18] S. Jana, A. Salehi-Khojin, W. H. Zhong, Enhancement of fluid thermal conductivity by the addition of single and hybrid nano-additives, Thermochimica Acta 462 (1-2) (2007) 45–55. `doi:10.1016/j.tca.2007.06.009`.

7

FPC development and integration of the air-cooled absorption machine in a solar thermal driven system

ABSTRACT

The heat source of the absorption system in this thesis is hot water in range of 75-95°C. As shown in Chapter 4 solar heated water could be an ideal option to drive the absorption system. As a renewable energy source, solar heated water could significantly reduce the electricity/gas cost of the climatization system. In this chapter, a new proposal for a high-performance flat plate solar thermal collector (FPC) based on Transparent Insulation Materials (TIM) combining silica aerogel contained in insulation containers with plastic honeycomb is evaluated and compared with similar state-of-the-art technologies. Thus, the proposed FPC shows better performance than a basic plastic honeycomb collector at high $T_{\text{in}} - T_{\text{AMB}}/G > 0.06$ while potentially protecting the honeycomb layer from reaching high temperatures. The performance data is also compared with a previous version of the FPC with combined TIM of plastic honeycomb with silica aerogel to demonstrate that the performance has been improved with a new construction strategy. Then a solar-assisted heating/cooling system, with high-efficiency solar collectors based on TIM, a storage tank, and the absorption machine, is evaluated employing system simulations. Several simulations in each case are performed with meteorologic data of Barcelona and Madrid in summer and winter for a case study heat source consisting of

30 m^2 solar collectors and an auxiliary heater. The fraction of solar energy in the heat source varies depending on the total radiation in the area, which could reach 0.65 on a sunny summer day as an absorption chiller or less than 0.1 on a cloudy winter day as an absorption heat pump. The high-performance FPC was reported in previous works about solar collectors and dynamic simulation of absorption systems in [1], [2], and the integration simulation of solar-assisted absorption system was reported in [3].

7.1 Development of a high-performance flat plate solar collector

7.1.1 Literature review of solar collector prototypes

Solar thermal collectors operated under low to medium temperatures have different technologies in the current market. Besides FPC, stationary compound parabolic collectors (CPC), evacuated tubes collectors (ETC), Fresnel lens collectors (FLC), small parabolic trough collectors (PTC), and cylindrical trough collectors (CTC) are other technological alternatives widely investigated, according to Tian et al. [4]. Also, Sharma et al. [5] demonstrated that a solar-heated system could be employed in various applications depending on the temperature and working fluid. Many authors. Sokhansefat et al. [6] used TRNSYS16 software for a thermo-economic analysis of two different solar hot water systems with FPC, ETC in cold winter Iran. Their results showed that the ETC system is 41% better than the FPC systems, so applying ETC in cold climates is recommended.

Osorio et al. [7] used Transparent Insulation Materials (TIM) in the FPCs, PTCs, and CR, then the results presented that TIM could dramatically increase the thermal efficiency at high absorber temperatures. According to Osorio's results, for the FPCs, when the extinction coefficient of TIM $\omega = 8m^{-1}$ and the absorber temperature $T_{abs} > 103°C$, the FPCs with TIM have higher efficiency than the conventional ones and if $\omega = 1m^{-1}$, the value of T_{abs} could be reduced to 55°C. High-performance honeycomb flat plate solar collector (FPC) using honeycomb plastic TIM has been established as a commercial market solution (an example of that is TIGI collector [8]. This technology achieves a good tradeoff between high efficiency in the high-temperature range ((Ti-Ta)/G>0.08)) with a reasonable cost compared to evacuated tube collectors. Beikircher et al. [9] presented that optimized mounting insulation with 30mm layer of symmetric film insulation of 10μm thick Al-foil should yield the same results as mineral wool with 50 mm insulation thickness. Besides, the film does not store moisture and could avoid fogging and corrosion.

Zhou et al. [10] also studied FPCs with TIM using numerical methods, and the results show that if the transmittance of TIM is below 80%, the collector with TIM has no advantages. Ammar et al. [11] used transparent insulation material parallel slats (TIM-PS) to prevent air convection in a flat plate solar air collector for industrial agriculture drying. To protect TIM from the high temperature of the absorber, in [12], an overheating protecting ventilation channel based on shape memory alloy is used in the FPC, which can ventilate the FPC and prevent the TIM from igniting. Wu et al. [13] introduced aerogel to the PV/T collector and found that the heat loss of the PV/T at 70°C could be reduced up to 75% and the thermal efficiency increased by 46%. The coefficient generally has a linear relationship with solar radiation and ambient temperature.

Silica aerogel can be introduced into the solar collector cover due to its high transmittance and low thermal conductivity, which also has an ultra-low density to decrease thermal losses. The current study intends to validate a new proposal of a collector with a compound TIM cover of plastic honeycomb and a silica aerogel layer contained using insulation containers that are implemented using polyurethane. The high-performance FPC has been tested on summer days. The design aims to reduce the thermal loss in the relatively high-temperature T_{abs}>90°C. Additionally, it is compared with previous versions of plastic honeycomb TIM from Kizildag et al. [12] and silica aerogel TIM layer collectors. In this chapter, manufacturing details of the new FPC collector are also provided.

7.1.2 Mathematical modelling of the solar collector system

For the solar collector field, a fast calculation model is employed, i. e. steady-state efficiency curve for coomputing the instantaneous efficiency (η) applied to the incoming solar energy (see Equation 7.1). In this way, an estimated value of the collector outlet is calculated as follows:

$$T_{\mathrm{out}} = T_{\mathrm{in}} + \eta G A / (\dot{m}_{\mathrm{abs}} C_{\mathrm{p}}) \tag{7.1}$$

Where the performance of the collector is calculated from the steady-state efficiency curve:

$$\eta = a_0 - a_1 \frac{(T_{\mathrm{in}} - T_{\mathrm{AMB}})}{G} - a_2 \frac{(T_{\mathrm{in}} - T_{\mathrm{AMB}})^2}{G} \tag{7.2}$$

For the storage tanks, an overall energy balance is performed. Therefore, it is assumed a complete mixing of the liquid, i. e. no stratification effects are taken into account:

$$M_{\text{tank,f}} C_{\text{p}} \frac{\partial T}{\partial t} = \dot{m}_{\text{tank,in}} c_{\text{p}} (T_{\text{tank,in}} - T_{\text{tank,f}}) + \dot{m}_{\text{tank,out}} C_{\text{p}} (T_{\text{tank,out}} - T_{\text{tank,f}}) \\ -(UA)_{\text{tank}} (T_{\text{tank}} - T_{\text{AMB}}) + Q_{\text{load}} \qquad (7.3)$$

It is assumed that the outlet tank temperatures are the same as the average temperature inside this device. In Equation (7.3), for the hot tank case, Q_{aux} is the auxiliary heat that depends on the tank temperature according to the proposed control. For the chilled water tank case, the Q_{aux} value is fixed to zero. Variables $\dot{m}_{\text{ch}}$ and $T_{\text{in,ch}}$ refer to the mass flow and inlet temperature of the entrance from the chiller, respectively. They came from the secondary stream of the evaporator for the cold tank case, and for the hot tank case, they came from the secondary stream of the generator. Variables $\dot{m}_{\text{ot}}$ and $T_{\text{in,ot}}$ refer to the inlet mass flow and temperature of the other entrance different from the chiller: from the collector for the hot tank case, from the cooling load for the chilled water tank. The cooling load Q_{load} is modelled using an additional energy source, using profiles extracted from Ziegler et al. [14]. Therefore, Q_{load} is a variable that varies hourly.

For performing the simulations, a modular object-oriented simulation platform is used (NEST) [15], which allows the linking between the different components (solar collectors, pump, valves, heat exchangers, etc.) of a determined system, enabling high flexibility in the configurations. In this numerical platform, each component is considered an object that can be either an empirical-based model (e. g., heat exchangers, storage tanks) or a more detailed CFD calculation if necessary. The solar assited absorption system is operated on the NEST platform in previous work [1], [2], [3].

7.1.3 Previous versions of solar collector

In the CTTC group, several developments of high-performance FPC with plastic honeycomb TIM are reported in [16], [12], [17], [18]. The solar collectors are shown in Figure 7.1a, and its sketch is represented in Figure 7.1b. In these collectors, the plastic TIM is glued to the cover glass, and there is an air gap between TIM and the absorber as overheating protection. Behind the absorber, the air channel activated through a memory alloy spring system is also employed as overheating protection. And the rest part is insulation. Figure 7.2 represents the experimental test system of the solar

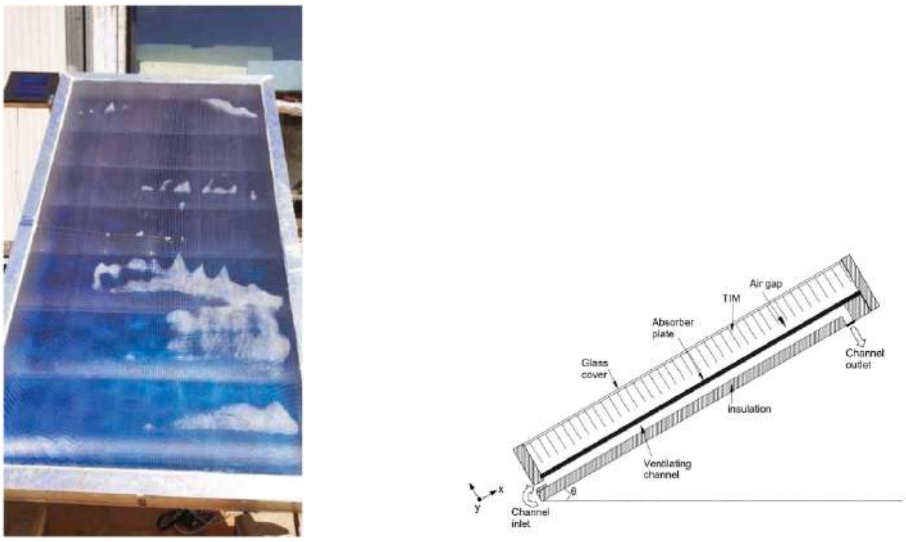

(a) Photo of FPC with TIM (b) Sketch of the FPC

Figure 7.1: FPC with TIM developed by Kizildag et al. [12]

collectors. As shown in the picture, the solar collector is connected to the system: first, the heat carrier fluid flow passes through the electrical heater. Then the fluid passes through to a storage tank, and finally, it circulates through the collector. The electric heater is set as an auxiliary heater to regulate the inlet temperature, which is essential to achieve a steady state of the collector (the efficiency curve is only valid under a steady-state period).

7.1.4 Development of a high-performance flat plate solar collector

The flat plate solar collector with TIM in this work is addressed as a further development of the collector proposed at Kizildag et al. [12]. The main difference is an extra insulation layer of silica aerogel, as shown in Figure 7.3. The ventilation channel is set behind the absorber since there will be only a small air gap inside the collector. The plastic TIM is made of cellulose triacetate, which has an outgassing temperature of 120-160°C. This phenomenon produces yellowing and embrittlement at temperatures above 100 °C [12]. The silica aerogel was introduced to the solar collector to avoid air convection between the absorber and TIM. The plastic TIM material was cellulose triacetate of

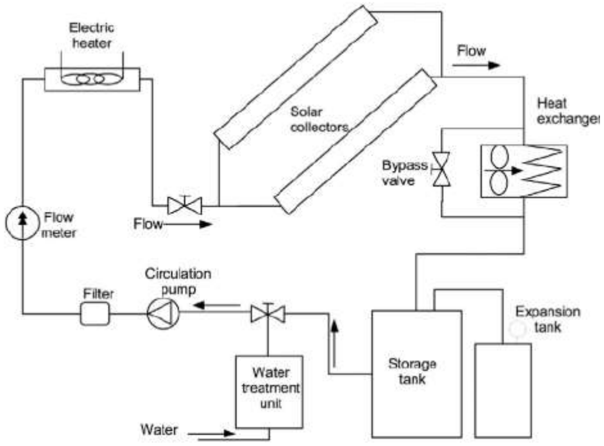

Figure 7.2: Solar collector test system in Kizildag et al. [12] and this work

dimension 2020*1070*75/80 mm, the 75 mm cut with two precise cuts for gluing to glass or absorber. The use of TIM material improves air convection and reduces the glass cover temperature of the collector.

A preliminary version of the FPC with combined TIM of plastic and silica aerogel was built in [19], while inside the inclined collector, the aerogel above the absorber fell with time passes as shown in Figure 7.4. Besides, the overheating problem of the plastic TIM contains risks when the water circuit stops. An example of a burnt solar collector with TIM due to overheating conditions is shown in Figure 7.5. The burnt part indicates that without a water circuit (overheating conditions), the temperature of the air inside the collector has reached more than 120 °C.

The aerogel used here has a thermal conductivity of 0.01 $W{\cdot}m^{-1}K^{-1}$ at ambient temperature, with a density of 0.1 g/cm^3. First, the absorber was fixed above the back insulation, and then the silica aerogel was tiled above the absorber, with a thickness of 2cm. Since the aerogel is in the shape of particles and the collector is inclined, an auxiliary structure should be placed to fix the aerogel layer. Seven polyurethane bars were attached above the absorber with the same thickness as the aerogel. Then, another tempered glass (same as the cover) is placed on top of the aerogel and bars. As the TIM material is glued to the external cover glass, it can be fixed together with the support structure. The cover should not be placed directly above the inner glass since the absorber may deform with some curvature. Therefore, a small gap(<1cm) between

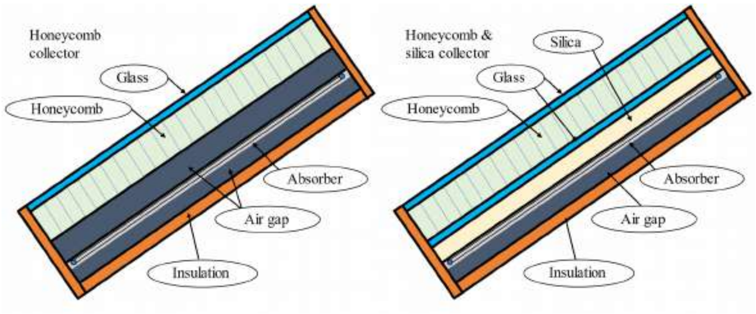

Figure 7.3: Solar collector sketch compared of first version(without fixing aerogel) in [12](left) and in this work (right)

Figure 7.4: Solar collector first version with TIM and aerogel

Figure 7.5: A burnt solar collector with TIM inside

the first layer of glass and TIM should always be considered. Finally, the collector should be well insulated.

The details of the current version of FPC is shown in Table 7.1. And the efficiency curvature of the final collector is shown in a previous work [20].

7.1.5 Experimental results of the solar collector

The test rig of the solar collector is shown in Figure 7.2. The experimental results of the previous solar thermal collectors depicted in Figure 7.1a and the new proposal shown in Figure 7.6 can be seen in Figure 7.7, the empirical correlations are listed as below.
i) TIGI collector [8] $\eta = 0.756 - 4.305\frac{T_{\mathrm{in}}-T_{\mathrm{AMB}}}{G} - 0.009\frac{(T_{\mathrm{in}}-T_{\mathrm{AMB}})^2}{G}$
ii) Kessentini et al. [18] $\eta = 0.713 - 2.648\frac{T_{\mathrm{in}}-T_{\mathrm{AMB}}}{G} - 0.0161\frac{(T_{\mathrm{in}}-T_{\mathrm{AMB}})^2}{G}$
iii) Kizildag et al. [12] $\eta = 0.698 - 0.985\frac{T_{\mathrm{in}}-T_{\mathrm{AMB}}}{G} - 0.025\frac{(T_{\mathrm{in}}-T_{\mathrm{AMB}})^2}{G}$
iv) This work old version $\eta = 0.596 - 0.816\frac{T_{\mathrm{in}}-T_{\mathrm{AMB}}}{G} - 0.0157\frac{(T_{\mathrm{in}}-T_{\mathrm{AMB}})^2}{G}$
v) This work new version $\eta = 0.7075 - 2.192\frac{T_{\mathrm{in}}-T_{\mathrm{AMB}}}{G}$
The compound TIM of plastic honeycomb with a silica aerogel layer without containers

Table 7.1: Main data of the solar collectors tested

General Data		
Parameter	Data	Units
Length	2.065	[m]
Width	1.16	[m]
Thickness	0.131	[m]
Aperture area	2.24	[m^2]
Absorber		
Material	Aluminium sheet and tubes	[-]
Tube arrangement	Parallel	[-]
Number of tubes	9	[-]
Area	2.00	[m^2]
Area(With polyurethane barriers)	1.728	[m^2]
Plate thickness	0.0005	[m]
Tube spacing	0.132	[m]
Carrier tubes diameter	0.022	[m]
Riser tubes diameter	0.008	[m]
Solar absorptivity	0.95	[-]
Infrared emissivity	0.05	[-]
Cover		
Gross area	2.01	[m^2]
Glass thickness	0.004	[m]
Glass material	Tempered low iron	[-]
Glass transmissivity	0.96	[-]
Glass absorptivity	0.02	[-]
Glass reflectivity	0.02	[-]
TIM material	Cellulose triacetate	[-]
TIM thickness	0.075	[m]
TIM cell width	0.009	[m]
TIM wall fraction	1.1	[%]
TIM transmittance	0.99	[%]
Air gap thickness	0.01	[m]
Aerogel-silica		
Thermal conductivity	0.013	[W(m·K)$^{-1}$]
Transmittance(Visible)	0.98	[-]
Thickness	0.02	[m]
Reflectivity(Visible)	0.004	[-]
Reflectivity(Infrared)	0.05	[-]
Insulation		
Material	Polyurethane	[-]
Thickness	0.060	[m]
Thermal conductivity	0.022-0.028	[W(m·K)$^{-1}$]
Maximum temperature	150	[°C]
Ventilation channel		
Height	0.030	[m]
Surface emissivity	0.95	[-]

Figure 7.6: Solar collector with fixed aerogel in the test

(the previous version) has worse performance in the comparison with the version without silica aerogel [12] since the reduction of the optical efficiency, due to the use of glasses of 0.92 transmittance instead of 0.96. The proposed collector, represented in Figure 7.6, overcome the honeycomb collector when $(T_{\mathrm{in}} - T_{\mathrm{AMB}})/G > 0.06$. This important finding demonstrates the applicability of the silica aerogel to obtain high-efficiency collectors and that the technical difficulties could be overcome using containers to maintain silica distribution and shape. The curve is flattened due to the silica effect on the heat losses. Additionally, the improved distribution of the silica played a vital role in the results, as will be discussed in the following section.

7.1.6 Summary and discussion of the solar collector experimental results

The first version of silica aerogel with honeycomb FPC presented silica positioning issues consequence of manufacturing the FPC without considering the movement of the silica aerogel granulates inside the collector as explained in Section 7.1.4. For manufacturing the new version of the collector, it was prioritized to improve the distribution of granular silica aerogel. First, some containers located strategically were implemented. Second,

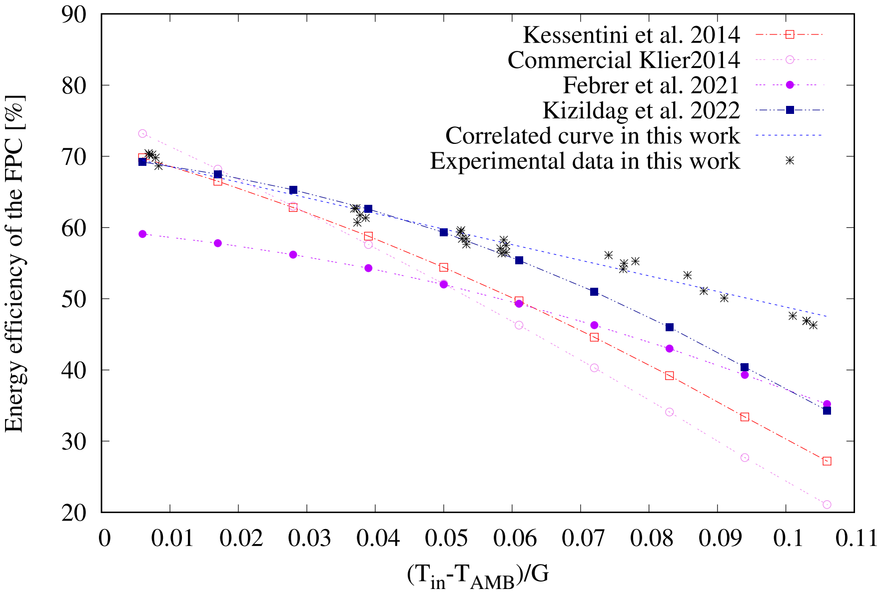

Figure 7.7: Efficiency curve of solar collectors

the absorber was more rigid to assure the distribution of the silica aerogel granulates' uniform distribution on the absorber surface. Previous designs without containers struggled in properly contain the silica on the top side of the collector. Thus, the heat losses in the hottest part of the FPC were high. The higher the stability of the silica inside the collector and the less air contained inside, the better the efficiency is achieved. If the performance of the two versions of combined silica aerogel/plastic honeycomb TIM FPC is compared, cannot be neglected the relevant effect of using high transmittance glass in the present collector (0.96) compared to the one in the previous version (0.92). An important aspect for improving the following versions of the new collector is the optimization of the effective area, as the polyurethane bars that contain the silica aerogel occupy part of the FPC area (now about 15%).

7.2 Simulations of the solar-assisted absorption system

The dynamic simulations were performed with the corresponding climate data, temperature, and radiation with solar collectors and storage tanks. Typical data in Barcelona and Madrid were introduced in both summer and winter for short and long-term simulation periods, i. e., eight hours and 1-2 months, respectively. Different switching temperatures were taken for the differential controller of the solar collectors. The hot tank is also assisted with an auxiliary heater to make up the heat when the hot water enters the generator, especially on cloudy days and at night.

7.2.1 Solar assisted absorption system description

Figure 7.8 shows the solar-assisted absorption system in this work, which consists of an absorption system and hot/cold storage tank, and flat solar collectors. The hot tank is connected to the generator and solar collector(energetic curve extracted from [12]), and an auxiliary heater is integrated inside. A differential controller is applied to the heater to maintain the generator's secondary circuit temperature in a required range.

Figure 5.2 shows the two modes of the absorption system: a) heat pump and b) absorption chiller. The absorption machine is air-cooled, with a vertical arrangement of the components, as shown in the picture. The air, driven by the fan, passes through the absorber and condenser. In the heat pump mode, the absorption machine works inside the building, the evaporator secondary circuit will take heat from the cold tank circuit, which is operated at ambient temperature, and there will be heat rejected from the absorber and condenser as output to heat the building. In the chiller mode,

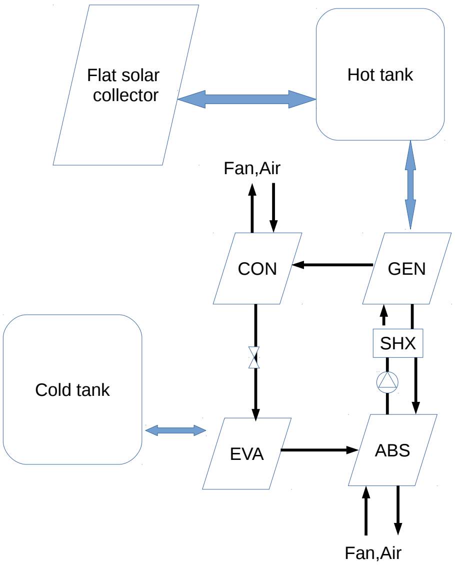

Figure 7.8: System of solar-assisted absorption system

the ambient for the machine is the outside condition, and the chilled water in the evaporator secondary circuit will be sent to the cold tank as cooling output. The ambient temperature is either set as a fixed value or provided by meteorological data extracted from Barcelona or Madrid. The temperature inside the building is fixed to 20°C. The cold tank temperature is set as 14°C in the chiller mode, and in the heat pump mode, it is set to ambient temperature. Inside the absorption system, working fluid pairs LiBr-H_2O and Carrol-H_2O are used to compare the chiller mode, while in the heat pump mode, EG is introduced to the evaporator to avoid the freezing problem, and only Carrol absorbent is used. The mass concentration of EG in the evaporator in heat pump mode is set to 10% and 30% according to the lowest temperature in Barcelona, and Madrid, respectively.

7.2.2 Simulations of 5 days of integrated solar-assisted absorption system

The simulations of the absorption system lasting five days, are carried out to investigate the dynamic performance for a long-term period. In the simulations, the solar collectors are connected to the absorption system, so a differential controller is applied to activate their pump. Moreover, in both modes (chiller and heat pump), the heat source temperature range will be 75-90°C. Therefore, the auxiliary heater will be activated when the hot water tank temperature is lower than 75°C. Hence, several parameters are used to describe the system's performance. COP_{Th} is the thermal COP of the machine, which means the proportion of cooling capacity generated from the heat energy consumed, as shown in (Equation 7.4):

$$COP_{\mathrm{Th}} = \overline{Q}/\overline{Q}_{\mathrm{GEN}} \tag{7.4}$$

Where $\overline{Q}$ is the corresponding capacity, in chiller mode equal to $\overline{Q}_{\mathrm{EVA}}$, while in heat pump mode equal to $(\overline{Q}_{\mathrm{CON}} + \overline{Q}_{\mathrm{ABS}})$.

COP_{El} represents the working capacity generated compared with the auxiliary electricity consumption, as shown in (Equation 7.5):

$$COP_{\mathrm{El}} = \overline{Q}/(\overline{E}_{\mathrm{aux}}) \tag{7.5}$$

Where $\overline{E}_{\mathrm{aux}}$ represents the electricity consumption of pumps and fans.

f_{solar} represents the fraction of solar energy in the total energy consumed in the absorption system, as shown in (Equation 7.6):

$$f_{\mathrm{solar}} = \overline{E}_{\mathrm{col}}/(\overline{E}_{\mathrm{heat}} + \overline{E}_{\mathrm{col}} + \overline{E}_{\mathrm{aux}}) \tag{7.6}$$

Where $\overline{E}_{\text{col}}$ is the energy provided by the solar collectors.
COP_{sys} means the total system performance combined absorption system and solar collector, as shown in (Equation 7.7):

$$COP_{\text{sys}} = \overline{Q}/(\overline{E}_{\text{heat}} + \overline{E}_{\text{aux}} + \overline{E}_{\text{col}}) * \overline{E}_{\text{col}}/\overline{E}_{\text{rad}} \tag{7.7}$$

where $\overline{Q}/(\overline{E}_{\text{heat}} + \overline{E}_{\text{aux}} + \overline{E}_{\text{col}})$ represents the energy efficiency of the absorption system and $\overline{E}_{\text{col}}/\overline{E}_{\text{rad}}$ represents the energy efficiency of the solar collector. Table 7.2 shows the numerical results of the absorption system with working pairs Carrol-H_2O of 5 days in summer and winter. $\overline{T}_{\text{AMB}}$ is the average outdoor temperature. This data is extracted from meteorological data from Barcelona and Madrid. From the results it could be concluded that if the solar-assisted absorption system worked non-stop 5 days in summer the solar energy could provide more than half energy consumed. Meanwhile in winter, this value is significantly lower due to the climate condition, in a sunny day, the solar energy could still provide nearly half percent of the consumption.

Using the information provided by Table 7.2, the reduction of CO_2 emissions could be calculated. In 2019, Spain emitted 198 g CO_2 per kWh for electricity generation according to IEA Spain 2021 [21]. Considering a climatization system with a cooling capacity of 4kW with an electrical vapour compression system with COP of 3, in a week, the electricity consumption is 224 kWh, and the corresponding CO_2 emission is 44.3 kg CO_2. If the absorption system is employed in the same case when the f_{solar} is near 1.0 and COP_{El} is 15, more than 75% CO_2 emission will be deducted. And when the $f_{\text{solar}} = 0.8$, and the rest heat is from a domestic gas boiler, electrical heater, or heat pump with CO_2 emission at 67.5, 103, and 29.0 kg/GJ^{-1} respectively, according to Alvarez et al. [22]. The corresponding CO_2 deduction compared with the electrical vapour compression refrigeration system will be 3.5%,44%, and 3% for hot water from a gas boiler, electrical heater, and heat pump, respectively.

7.2.3 Conclusions of the integrated solar-driven absorption system

Simulations for the absorption system at different working modes with two working pairs are presented in this section. The results show that the working pair Carrol-H_2O has a lower cooling capacity, a lower crystallization risk, and a similar *COP* when compared with LiBr solution at chiller mode. According to the simulations in the heat pump mode using the working pair Carrol-H_2O, the heating capacity will not be affected much by the heat source temperature, and *COP* decreases along with the heat source

Table 7.2: Numerical results of dynamic simulations of absorption system at both modes with working pair Carrol-H_2O

	Time	$\overline{T}_{\text{AMB}}$ [°C]	$\overline{Q}$[kW]	COP_{Th}	f_{solar}	COP_{sys}	COP_{El}
Madrid Chiller Mode	Day 1	25.5	3.9	0.74	0.42	0.25	14.7
	Day 2	26.5	3.2	0.77	0.43	0.24	13.9
	Day 3	21.3	4.1	0.80	0.65	0.27	17.9
	Day 4	20.3	4.4	0.81	0.66	0.28	19.3
	Day 5	25.1	3.6	0.78	0.65	0.24	15.3
Barcelona Chiller mode	Day 1	23.2	4.2	0.76	0.62	0.26	17.3
	Day 2	22.8	4.3	0.80	0.63	0.27	18.1
	Day 3	24.1	4.2	0.80	0.56	0.28	17.1
	Day 4	25.1	3.9	0.78	0.62	0.26	16.2
	Day 5	25.1	4.0	0.78	0.62	0.26	16.2
Madrid heat pump Mode	Day 1	3.1	14.1	1.60	0.45	1.02	37.9
	Day 2	0.0	14.7	1.61	0.52	1.17	37.7
	Day 3	0.6	15.3	1.60	0.05	0.40	33.4
	Day 4	5.2	16.2	1.61	0.13	0.73	35.0
	Day 5	6.9	15.3	1.62	0.39	1.08	38.0
Barcelona heat pump Mode	Day 1	13.9	19.9	1.65	0.002	0.03	43.1
	Day 2	13.1	19.6	1.65	0.07	0.47	42.3
	Day 3	12.3	19.2	1.65	0.07	0.41	41.6
	Day 4	10.9	18.6	1.64	0.06	0.33	40.3
	Day 5	10.4	18.4	1.64	0.02	0.20	39.9

temperature. Also, lower evaporator secondary inlet temperature leads to lower COP, lower heat capacity, and higher crystallization risk. On the other hand, the long period tests of the complete solar heating system with meteorologic data from Madrid and Barcelona demonstrate that on a sunny day, the solar fraction reaches values of 40-65% and the average COP_{TH} at chiller mode is 0.73-0.81, at heat pump mode is 1.6.

Nomenclature

Name	**Description**
a_0,a_1,a_2	Correlated coefficients Equation 7.2 [-]
A	Area [m^2]
COP	Coefficient of performance [-]
COP_{EX}	Exergetic coefficient [-]
C_{p}	Specific heat capacity [J(kg·K)$^{-1}$]
$\overline{E}$	Average energy comsumption rate [kW]
f	Fraction [-]
G	Solar irradiance on FPC [W·m^{-2}]
$\dot{m}_{\mathrm{abs}}$	Mass flow rate inside the solar collector [kg·s^{-1}]
$\dot{m}_{\mathrm{tank,in}}$	Mass flow rate at inlet of the tank [kg·s^{-1}]
$\dot{m}_{\mathrm{tank,out}}$	Mass flow rate at outlet of the tank [kg·s^{-1}]
M	Mass [kg]
Q	Heat flux [kW]
$\overline{Q}$	Averrage working capacity [kW]
t	Time [s]
T	Temperature [°C]
$\overline{T}$	Average temperature [°C]
U	Heat conductance [W·K^{-1}]
X	Solute weight concentration [-]
x,y,z	Coordinates [m]
Greek letter	**Description**
α	Heat transfer coefficient [Wm^{-2}K^{-1}]
β	Mass transfer coefficient [kg·s^{-1}]
Γ	Mass flow rate per length [kg(m·s)$^{-1}$]
η	Efficiency of the solar collector [%]
θ	Contact angle [$\circ$]
λ	Thermal conductivity [Wm^{-1}K^{-1}]
μ	Dynamic viscosity [Pa·s^{-1}]
ρ	Density [kg·m^{-3}]
ω	Extinction coefficient [m^{-1}]
Abbreviation	**Description**
2-EH	2-Ethylhexanol
CPC	Compound parabolic collector
CTC	Cylindeical trough collector
EG	Ethylene glycol
ETC	Evacuated tubes collector
FLC	Fresnel lens collector

Abbreviation	**Description**
FPC	Flat plate collector
MWR	Minimum wetting rate
PMC	Phenylmethylcarbinol, 1−Phenylethanol
PTC	Parabolic trough collector
TIM	Transparent insulation materials
VLE	Vapor-liquid equilibrium
wt	Weight ratio **Subscripts**
& Superscripts	**Description**
abs	Solar absorber(Solar collector system)
aux	Auxiliary power
ABS	Absorber(Absorption system)
AMB	Ambient
ch	Absorption chiller
col	Collector
CON	Condenser
EVA	Evaporator
El	Electricity
EX	Exergy
f	Fluid
GEN	Generator
heat	Heating power
in	Inlet
load	Energy loaded
out	Outlet
ot	Other
rad	Radiation
solar	Solar power
sys	System
tank	Storage tank
tot	Total
Th	Thermal

References

[1] R. Febrer, J. Castro, J. Zheng, J. Rigola, A. Oliva, D. Kizildag, Mathematical Modeling and Experimental Validation of a Highly Efficient Flat Plate Solar Collector with compound Transparent Insulation Materials including a Silica Layer, Proceedings - ISES Solar World Congress 2021 (2021) 408–419`doi:10.18086/swc.2021.22.03`.

[2] J. Zheng, R. Febrer, J. Castro, J. Rigola, D. Kizildag, Experimental Testing of a Solar Thermal Collector with composite TIM of plastic Honeycomb and Silica Aerogel Polyurethane Containers, in: Proceedings - EuroSun 2022, 2022.

[3] J. Zheng, J. Castro, C. Oliet, Dynamic simulations of an absorption system with different working pairs at chiller and heat pump application, in: Purdue Congress, 2021, pp. 1–10.

[4] Y. Tian, C. Y. Zhao, A review of solar collectors and thermal energy storage in solar thermal applications, Applied Energy 104 (2013) 538–553. `doi:10.1016/j.apenergy.2012.11.051`.

[5] A. K. Sharma, C. Sharma, S. C. Mullick, T. C. Kandpal, Solar industrial process heating: A review, Renewable and Sustainable Energy Reviews 78 (January) (2017) 124–137. `doi:10.1016/j.rser.2017.04.079`.

[6] T. Sokhansefat, A. Kasaeian, K. Rahmani, A. H. Heidari, F. Aghakhani, O. Mahian, Thermoeconomic and environmental analysis of solar flat plate and evacuated tube collectors in cold climatic conditions, Renewable Energy 115 (2018) 501–508. `doi:10.1016/j.renene.2017.08.057`.

[7] J. D. Osorio, A. Rivera-Alvarez, P. Girurugwiro, S. Yang, R. Hovsapian, J. C. Ordonez, Integration of transparent insulation materials into solar collector devices, Solar Energy 147 (2017) 8–21. `doi:10.1016/j.solener.2017.03.011`.

[8] S. Klier, Z. Klier, M. Adel, R. Efron, System and method for temperature limiting in a sealed solar energy collector.

[9] T. Beikircher, V. Berger, P. Osgyan, M. Reuß, G. Streib, Low-e confined air chambers in solar flat-plate collectors as an economic new type of rear side insulation avoiding moisture problems, Solar Energy 105 (2014) 280–289. `doi:10.1016/j.solener.2014.03.033`.

[10] L. Zhou, Y. Wang, Q. Huang, Parametric analysis on the performance of flat plate collector with transparent insulation material, Energy 174 (2019) 534–542. `doi:10.1016/j.energy.2019.02.168`.

[11] M. Ammar, A. Mokni, H. Mhiri, P. Bournot, Parametric investigation on the performance of natural convection flat plate solar air collector with additional transparent insulation material parallel slats (TIM-PS), Solar Energy 231 (November 2021) (2022) 379–401. `doi:10.1016/j.solener.2021.11.053`.

[12] D. Kizildag, J. Castro, H. Kessentini, E. Schillaci, J. Rigola, First test field performance of highly efficient flat plate solar collectors with transparent insulation and low-cost overheating protection, Solar Energy 236 (December 2021) (2022) 239–248. `doi:10.1016/j.solener.2022.02.007`.

[13] L. Wu, B. Zhao, X. Ao, H. Yang, X. Ren, Q. Yu, K. Guo, M. Hu, G. Pei, Performance analysis of the aerogel-based PV/T collector: A numerical study, Solar Energy 228 (September) (2021) 339–348. `doi:10.1016/j.solener.2021.09.077`.

[14] J. Ziegler, N. Nichols, Optimum settings for PID controllers, Transactions of ASME 64 (1942) 759–768.

[15] J. Lopez, O. Lehmkuhl, R. Damle, J. Rigola, A parallel and object-oriented general purpose code for simulation of multiphysics and multiscale systems, in: Proceedings of the 24th International Conference on Parallel CFD, 2012.

[16] D. Kizildag, J. Castro, H. Kessentini, J. Rigola, A. Oliva, Development, optimization and test performance of highly efficient flat plate solar collector with transparent insulation and low-cost overheating protection, in: ISES Sol. World Congr. 2017-IEA SHC Int. Conf. Sol. Heat. Cool. Build. Ind. 2017, Proc, 2017, pp. 2031–2042. `doi:10.18086/swc.2017.31.07`.

[17] H. Kessentini, J. Castro, R. Capdevila, A. Oliva, Development of flat plate collector with plastic transparent insulation and low-cost overheating protection system, Applied Energy 133 (2014) 206–223. `doi:10.1016/j.apenergy.2014.07.093`.

[18] H. Kessentini, R. Capdevila, J. Castro, A. Oliva, C. Bouden, Three dimensional heat transfer analysis of combined conduction and radiation in honeycomb transparent insulation, Solar Energy 105 (2014) 58–70. `doi:10.1016/j.solener.2014.02.027`.

[19] R. Febrer Cordoba, J. Castro González, J. Zheng, J. Rigola Serrano, A. Oliva, Mathematical Modeling and Experimental Validation of a Highly Efficient Flat Plate Solar Collector with compound Transparent Insulation Materials including a Silica Layer, in: International Society of Exposure Science (ISES), 2021, pp. 74–78.

[20] J. Zheng, R. Febrer, J. Castro, J. Rigola, D. Kizildag, Experimental Testing of a Solar Thermal Collector with composite TIM of plastic Honeycomb and Silica Aerogel Polyurethane Containers, in: ISES and IEA SHC International Conference on Solar Energy for Buildings and Industry, 2022, pp. 74–78.

[21] I. E. Agency, Iea spain 2021 energy policy review (2021).

[22] R. A. Alvarez, S. W. Pacala, J. J. Winebrake, W. L. Chameides, S. P. Hamburg, Greater focus needed on methane leakage from natural gas infrastructure, Proceedings of the National Academy of Sciences 109 (17) (2012) 6435–6440.

8

General conclusions and Future work

ABSTRACT

The conclusions of the thesis are developed and summarised in this chapter. In this thesis, the thermophysical properties of working pairs are modelled mathematically, such as entropy, exergy, activity coefficient, and nanofluid properties, or measured experimentally, such as electrical conductivity, surface tension, and contact angle. The reported properties are employed later in the simulation.

Besides, an experimental set-up is set to measure the minimum wetting rate of falling film and the temperature distribution alongside the liquid film with and without nanofluid. Moreover, the temperature and concentration distribution of the vertical liquid falling film is solved via numerical simulation and verified using an analytical solution. This code is validated with experimental data generated from the set-up of falling film for pure heat transfer cases and using data from other's authors for absorption cases. The validated falling film code is used for assessing the enhancement of the heat and mass transfer coefficients due to nanoparticles.

Once the details in the falling film are determined, the simulation of the absorption system is carried out with energy and exergy analysis of two working pairs, LiBr-H_2O and Carrol-H_2O. Enhancement methods are also applied in the absorption system to improve the system's performance. The enhancement method could improve the working capacity by 5-10%.

Finally, a flat plate solar collector is integrated to the air-cooled machine in a solar heating/cooling system. The development details of a solar collector are demonstrated with experimental results, and solar-heated water is introduced as the heat source. As a final result, the absorption system could have a 4-8 kW refrigeration capacity and 15-20 kW heating capacity, with a *COP* at 0.75 and 1.65 at cooling and heating, respectively.

8.1 Conclusions

The main object of this thesis is convert the absorption system from chiller mode to heat pump mode, which could be employed in climatization applications as a low-carbon emission option. The optimization has been focused on the working pairs, falling film heat and mass transfer model, and steady-state/dynamic simulation. The work of this thesis into several principal tasks:

- Identification of the detailed thermophysical properties of working pairs LiBr-H_2O and Carrol-H_2O.
- Identification of the minimum wetting rate with numerical modelling and experiments with water, EG, LiBr-H_2O, and Carrol-H_2O in the presence of surfactant in liquid or vapor phase on tubes of different materials.
- Identification of the numerical modelling and experimental falling film heat and mass transfer. Quantify the heat and mass transfer coefficients of vertical falling film of working pairs LiBr-H_2O and Carrol-H_2O.
- Identification of the energy and exergy performance of an air-cooled absorption system with numerical studies in heating and cooling application with working pairs LiBr-H_2O and Carrol-H_2O.
- Identification of performance enhancement with numerical simulation of the air-cooled absorption machine system, investigate the effect on the *COP* and capacity of the enhancements of different methods to the heat and mass transfer coefficients.
- Identification of working performance of a solar-driven absorption system. A solar thermal collector works as the heat source to the absorption system and the integrated system is simulated with meteorological data from Madrid or Barcelona. Find the final working performance of a solar-driven absorption system performance in climatization applications.

The main conclusions are listed in the following subsections.

8.1.1 Thermophysical properties of working pairs

The related information were published in the works [1], [2], [3], [4].

- The properties of the working pairs are measured by experiments or modelled mathematically. For LiBr−H_2O and Carrol−H_2O. Specific entropy and exergy are calculated mathematically, with other parameters like activity coefficients. The activity coefficients are calculated with the UNIQUAC/LIQUAC method, and a simplification of correlation is provided. The activity coefficient of EG in the solution is usually pretty small (γ<2.5E-5 and P_{EG}<1 Pa). Hence the partial pressure of EG in the solution could be neglected. These properties are utilized in the exergy analysis.

- The electrical conductivity as a secondary property is measured for both working pairs at a wide range of temperature and concentration. The electrical conductivity could be used to measure the density of the solution as a cost-space effective method, especially in a compact absorption machine. For the temperature range, 30−80°C, concentration 40-70%, the electrical conductivity will increase with both temperature and concentration in a range of 100-400 mS/cm for both working pairs.

- The surface tension of both working pairs is measured with and without surfactant. Correlations of the surface tension with temperature and concentration are provided in the final results. Besides, the experimental results show that liquid and gaseous surfactants have a similar effect on the surface tension of the solution, needing more concentration for gaseous surfactants. The surface tension increase with concentration and decrease with temperature in a range of 60−100 mN·m^{-1}. With liquid or gaseous surfactant, the 60wt% LiBr solution with 2−EH could reach 35 mN·m^{-1} while the value is 40 for 65% Carrol solution with PMC.

- With untreated surfaces of stainless steel, copper, and PVC, the contact angle of two working pairs varies from 75−100∘. However, with a super hydrophilic surface treatment to stainless steel, the contact angle is reduced to 30∘.

- Nanoparticles of CuO and Al_2O_3 are also used to make nanofluids of the working pairs. The thermophysical properties are predicted with functions from literature, in which thermal conductivity has a high potential and could reach as high as 50%. E414 was introduced to stabilize the solution.

8.1.2 Experimental results of MWR of liquid vertical falling film

The related information were published in the previous work [3].

- Minimum wetting rate is calculated and compared with experimental results. The correlation results fit well with the experimental measurements in various fluid types and tube materials. The final experimental results agree with the correlation from [5] as shown in Equation 4.13.
- The contact angle is a critical parameter in the MWR measurement, and the super hydrophilic coating of the tube could significantly reduce the flow rate. The MWR of water on the super hydrophilic surface could reach 0.025 $\mathrm{kg(m\cdot s)^{-1}}$, while the corresponding value for a nontreated stainless steel surface is 0.096 $\mathrm{kg(m\cdot s)^{-1}}$.
- The surfactant will barely affect the MWR of the vertical falling film according to the experimental results.

8.1.3 Simulation and experimental results of heat and mass trasnfer in vertical falling film

The related information were partilly published in the works [6].

- A numerical simulation model of heat and mass transfer processes on the vertical falling film has been implemented with an in-house code based on C++. In the first stage, the numerical simulation was focused on pure heat transfer phenomena. The numerical results have been compared with the analytical solution and another experimental correlation, with good agreement. Then, the heat transfer coefficient for several cases was obtained numerically. When the mass flow rate is in the range of 0.15-0.6 $\mathrm{kg\cdot m^{-1}s^{-1}}$, the heat transfer coefficient for EG, LiBr55%, Carrol60%, and water is around 700-1500, 1600-2200, 1800-2400 and 2800-3800 $\mathrm{W\cdot m^{-2}K^{-1}}$, respectively. With a nanofluid of 0.5% Al_2O_3, the heat transfer coefficient could increase around 10%.
- The numerical simulation model has been extended to heat and mass transfer processes on the vertical falling film with LiBr-H_2O and Carrol-H_2O as working fluids. The numerical model has been validated with experimental data extracted

from other authors. While in the low Re number range ($Re < 300$), the smooth laminar film model has been enough for predicting the heat and mass transfer performance. The mass transfer ability will increase with higher inlet temperature, higher inlet concentration, lower coolant temperature, and higher absorption potential pressure. And the LiBr-H_2O solution generally has a higher absorbing ability than the Carrol-H_2O solution.

8.1.4 Simulation of absorption system and thermodynamic analysis

The related information were published in the works [7], [4], [8], [6].

- The virtual absorption system is based on the physical data from the current absorption machine, when the machine is put into different applications like heating and cooling, different working pairs will be introduced and other parameters will not change. In the cooling application, the machine will be loaded with LiBr-H_2O to the generator and H_2O to the evaporator. Meanwhile, for the heating application, Carrol-H_2O is introduced into the generator and H_2O-EG will be introduced into the evaporator. The other auxiliary components like the fan, pump, and secondary circuit will not be affected.

- For the absorption system in the chiller mode, the Carrol system has around 6−10% higher COP and 5% higher COP_{EX} than the LiBr system at the same condition, while the total cooling capacity is only 80% of LiBr system.

- When EG is introduced in the evaporator of the Carrol system, the air-sourced heat pump application could overcome the freezing limit in the evaporator. Also, high heat source temperatures will not always lead to a higher heat capacity: the heat capacity will increase, reach a maximum value, and decrease along with the heat source temperature at a certain operating condition. Meanwhile, both COP and COP_{EX} will decrease.

- When the ambient temperature is set to 20°C, an optimum heat source temperature will be around 75-80°C, and the recommended EG mass concentration is 30%, the system heat capacity is around 15kW at a COP 1.5, COP_{EX} 1.0 and $E_{\mathrm{D,tot}}$ 2.75kW.

- Also, lower evaporator secondary inlet temperature leads to lower COP, lower heat capacity, and higher crystallization risk.

- If the wettability factor increased from 0.44 to 1.0, the working capacity of LiBr and Carrol could increase 10%, and 20%, respectively.
- Adding surfactants to the working pairs could reduce surface tension and strengthen the Marangoni effect, improving the heat and mass transfer effect. With surfactant 2−EH in the system under the same operating condition, the working capacity could increase by 3.2 – 7.8%, 4.8 – 13.1% for LiBr and Carrol working pairs, respectively. Meanwhile the COP, COP_{EX}, $E_{\text{D,tot}}$ stays at the same level.
- Similar to surfactants, the nanofluid could also change the thermophysical properties of working pairs by increasing the thermal conductivity. The thermal conductivity will increase by 30% for both working fluid pairs, and the working capacity will increase by around 5%.
- Besides, the vibration could also help to improve the working performance and has a similar effect to nanofluid. Also, all these enhancements could be applied to the same system simultaneously. The simulation may not predict the final performance since the enhancements may interfere with each other somehow.

8.1.5 Development of the new FPC and integration in a solar-driven absorption system for climatization

The related information were published in the works [7], [9], [10].

- During the manufacturing of the new version of the collector, the air-silica compactness ratio has become a relevant issue. The higher the stability of the silica inside the collector and the less air contained inside, the better the thermal efficiency is.
- It was observed that the silica-honeycomb collectors' optical efficiency is lower compared to the pure plastic honeycomb TIM collector. However, its efficiency is higher in the $\Delta T/G > 0.074$ region.
- Another relevant lesson learned is that high-transmittance glasses are needed since the silica aerogel decreases optical performance. However, this fact is compensated by the improved insulation, as the efficiency curve is flattered at high temperatures, becoming a potentially competitive FPC.
- The long-term simulations with a whole solar cooling/heating absorption system, using meteorologic data from Madrid and Barcelona, demonstrate that on a sunny

day, the solar-heated water could fulfill 40-65% of total energy consumption, even in winter conditions. As a result, the average COP_{Th} in chiller mode is 0.73-0.81, and 1.6 as a heat pump.

8.2 Future works

With the current working procedure, future work can be divided into numerical and experimental parts.

8.2.1 Numerical simulation

- The numerical model for the falling film should be further developed for heat and mass transfer details.
    - The 2D model of smooth laminar film theory is limited for the prediction of temperature distribution of the vertical liquid falling film. A CFD model using OpenFOAM is under construction to predict the wave information at different ranges of Re.
    - For the wavy regime of the falling film, an in-house code based on C++ model based on the VOF method is under consideration for a better prediction of the fluid dynamics and heat and mass transfer.
- The system simulation of the solar collector and absorption system is complemented in the NEST platform.
    - Improvement for NEST platform for dynamic and steady-state simulation integrated with solar collector and absorption system in terms of new working pairs, enhancements, processing time, etc.
    - New control strategies for the solar collector and absorption system should be designed for improved dynamic operation performance.

8.2.2 Experiment and laboratory prototypes

- The current version of FPC has a higher efficiency in $\Delta T/G > 0.074$ region. Tests of the temperature limit should be carried out to find the max operating temperature before the burnt of TIM inside the collector. And more strategies could be employed to improve the general performance

  - Nanofluid could be employed in the circuit to reach a better heat transfer performance.
  - Polymer absorber is also an option for further reducing the cost and weight of the solar collector, especially the 3D printed components could be easily employing the enhancement method or advanced absorber surface.
  - Different control strategies for the mass flow could also be used to capture more energy from solar radiation.

- Vertical falling film experiment could be used to locate the fluid dynamic and heat transfer characteristics or the absorption details when in vacuum condition.
  - Absorption tests with $LiBr-H_2O$ and $Carrol-H_2O$ should be carried out to investigate the absorption performance possible improvements.
  - Working pairs with surfactant and nanofluid could also be employed to test the absorption performance.
  - Active methods for heat and mass transfer improvements could be added to the absorption system, such as electromagnetic field, ultrasonic vaporization, or mechanical vibration. One or combined strategies could be added to test the final results.
- Future work of compact absorption machine and separated modular system
  - The compact design of the absorption machine prototype should be reviewed, as the machine could be set as several modules, allowing to test of each component separately to facilitate the design of experiments.
  - Comparison between the pool boiling evaporation and the horizontal falling film evaporation under low pressure, with water and water-EG binary mixture, with and without surfactant.
  - A reliable vertical falling film distribution system should be applied to the absorber to ensure wettability.

8.2.3 DAC system

Furthermore, during the experiments, the DAC system is always a time-labor-cost-consuming problem. For a complex experiment/prototype, the traditional sensor-DAC-PC system could satisfy the necessities, while for a simple test with various sensors, the system may result too heavily. Considering this problem, a Python-Raspberry Pi based system is under construction as a portable plug-visualization DAC system with several inlets of different signals to reduce work.

Nomenclature

Name	**Description**
COP	Coefficient of performance [-]
COP_{EX}	Exergetic coefficient [-]
E_{D}	Exergy destruction rate [kJ·kg^{-1}]
G	Total solar radiation kW
P	Pressure [Pa]
Re	Reynolds number [-]
T	Temperature [°C]
Greek letter	**Description**
γ	Activity coefficient [-]
Δ	Difference [-]
Abbreviation	**Description**
2-EH	2-Ethylhexanol
EG	Ethylene glycol
FPC	Flat plate collector
MWR	Minimum wetting rate
PMC	Phenylmethylcarbinol, 1−Phenylethanol
VOF	Volume of fluid
Subscripts & Superscripts	**Description**
D	Destruction
EG	Ethylene glycol
EX	Exergy
Th	Thermal
tot	Total

References

[1] J. Zheng, J. Chiva, J. Castro, Y. Liu, A. Oliva, Electrical conductivity of concentrated LiBr Ethylene-Glycol and water ternary system, Journal of Physics: Conference Series 2116 (1) (2021) 012069. `doi:10.1088/1742-6596/2116/1/012069`.

[2] J. Zheng, J. Castro, C. Oliet, A. Oliva, Surface tension and contact angle measurement of LiBr and Carrol solution, in: International sorption Heat pump Congress, 2021, pp. 74—-78.

[3] J. Zheng, J. Castro, E. Garcia-Rivera, C. Oliet, A. Oliva, Study of the influence of surfactants and surface treatments on the minimum wetting rate of falling films of aqueous LiBr and Carrol solutions, International Journal of Refrigeration 141 (May) (2022) 146–157. `doi:10.1016/j.ijrefrig.2022.05.023`.

[4] J. Zheng, J. Castro, A. Oliva, C. Oliet, Energy and exergy analysis of an absorption system with working pairs LiBr-H2O and Carrol-H2O at applications of cooling and heating, International Journal of Refrigeration 132 (September) (2021) 156–171. `doi:10.1016/j.ijrefrig.2021.09.011`.

[5] K. R. Morison, Q. A. G. Worth, N. P. O'Dea, Minimum wetting and distribution rates in falling film evaporators, Food and Bioproducts Processing 84 (4 C) (2006) 302–310. `doi:10.1205/fbp06031`.

[6] J. Zheng, J. Castro, G. Papakokkinos, A. Oliva, Sensitivity study to an absorption system performance considering heat and mass transfer enhancements, in: Purdue Congress, 2022.

[7] J. Zheng, J. Castro, C. Oliet, Dynamic simulations of an absorption system with different working pairs at chiller and heat pump application, in: Purdue Congress, 2021, pp. 1–10.

[8] J. Castro, J. Farnós, G. Papakokkinos, J. Zheng, C. Oliet, Transient model for the development of an air-cooled LiBr-H2O absorption chiller based on heat and mass transfer empirical correlations, International Journal of Refrigeration 120 (2020) 406–419. `doi:10.1016/j.ijrefrig.2020.08.030`.

[9] R. Febrer, J. Castro, J. Zheng, J. Rigola, A. Oliva, D. Kizildag, Mathematical Modeling and Experimental Validation of a Highly Efficient Flat Plate Solar Collector with compound Transparent Insulation Materials including a Silica

Layer, Proceedings - ISES Solar World Congress 2021 (2021) 408–419`doi:10.18086/swc.2021.22.03`.

[10] J. Zheng, R. Febrer, J. Castro, J. Rigola, D. Kizildag, Experimental Testing of a Solar Thermal Collector with composite TIM of plastic Honeycomb and Silica Aerogel Polyurethane Containers, in: Proceedings - EuroSun 2022, 2022.

Appendix A

Appendix 1 Physical model of stable dry patch and uncertainties of experimental results

A.1 Uncertainties calculation of experiments

The type A uncertainty of the experimental results in this work is calculated as Equation A.1

$$\varepsilon = \left[\sum_{i=1}^{n} (m_i - \bar{m})^2 / (n-1) \right]^{\frac{1}{2}} \tag{A.1}$$

where ε represents the uncertainty at n times, and $\bar{m}$ is the average value of the test value. With other factors taken into consideration, the final uncertainty of the experiment result is shown as Equation A.2, proposed in [1], including type A and type B uncertainties.

$$\varepsilon_{\text{final}} = \left(\sum_{i=1}^{n} (\varepsilon_i)^2 \right)^{\frac{1}{2}} \tag{A.2}$$

where ε_i represents the uncertainty yields by n independent parameters like chemical purity, balance resolution, temperature measurement, etc. The purity of the distilled water, LiBr powder, EG, 2-EH and PCM is 99%. The temperature sensor PT100 has an accuracy at 0.1°C, the Coriolis flowmeter has a relative error at 1%, the electronic balance has an accuracy at 0.01 g, the tensiometer has a resolution of 0.1 $\text{mN}\cdot\text{m}^{-1}$. The temperature accuracy is 0.1°C, and this temperature variation would cause a maximum change in surface tension of approximately 0.02 mN/m for pure water and 0.03 for 60% LiBr solution. Considering all the parameters above, the type B uncertainty is around 0.55% for pure water and 0.7% for 60% LiBr solution in the measurement of surface tension. The uncertainty $\varepsilon_{\text{final}}$ is 1.5% of the pure liquid sample and 2.3% of the sample with gaseous surfactants. On the other hand, the uncertainty for the contact angle measurement is around 1%. Finally, the uncertainty for the MWR measurement is around 8%.

A.2 Physical model of a stable dry patch

A prediction model is used here for a laminar gravity annular flow of liquid film over a tube. A schematic of a stable dry patch in [2] as shown in Figure A.2.1. The model was solved by balancing the surface tension force along the dry patch edge, as shown in Equation A.3.

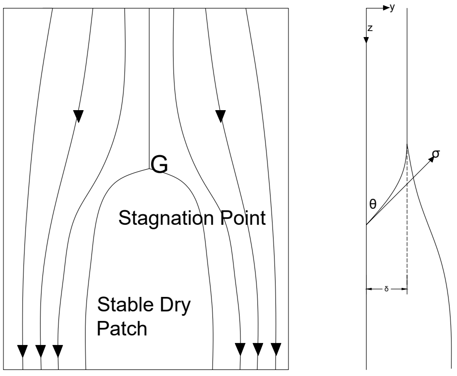

Figure A.2.1: A schematic of a stable dry patch

$$\int_0^\delta \rho u^2 \mathrm{d}y = \sigma(1-\cos\theta) \tag{A.3}$$

where u is the axial velocity, σ is the effective surface tension, and θ is the corresponding contact angle. Also, a fully developed laminar flow is assumed around the tube due to

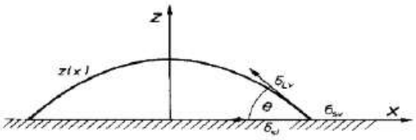

Figure A.2.2: Single rivulet profile

the low mass flow rate. And in the velocity profile is shown as Equation A.4

$$u = \frac{\rho g}{2\mu}\left(\delta^2 - y^2\right) \tag{A.4}$$

where $\delta = \left(\frac{3\mu\gamma}{\rho^2 g}\right)^{\frac{1}{3}}$ is the film thickness, μ is viscosity in Pa·s^{-1}. Thus the final result could be obtained as Equation A.5

$$\frac{\Gamma}{\mu} = 1.116(1-\cos\theta)^{0.6}\left(\frac{\rho\sigma^3}{\mu^4 g}\right)^{\frac{1}{3}} \tag{A.5}$$

while in [3], regarding the same physical model, the momentum equations are the same as A.3, considering the liquid flows transversely after bumping into a stagnation point of the dry patch. A friction force of flow caused in the horizontal direction and its reaction force, R, tends to wet the dry patch, $R = K_1\mu\bar{u}$. Hence, Equation A.3 is modified to Equation A.6 and A.7, in case of low viscosity liquid, Equation A.7 could be reduced to A.3.

$$K_1\mu\bar{\mu} + \int_0^\delta \rho u^2 \mathrm{d}y = \sigma(1-\cos\theta) \tag{A.6}$$

$$K\left(\frac{\gamma}{\mu}\right)^{2/3} + \frac{2\cdot 3^{5/3}}{15}\left(\frac{\gamma}{\mu}\right)^{5/3} = A\left(\frac{\rho\sigma^3}{\mu^4 g}\right)^{1/3} \tag{A.7}$$

where mean velocity $\bar{u} = \gamma/(\rho\delta)$, K=K$_1^{1/3}$ is a proportional constant, $A = (1-\cos\theta)$. Coefficients K and A are determined with the experimental data.

In [4], a laminar rivulet thickness has been considered. The total energy of the rivulet segment of length Δy is as shown in Equation A.8, the corresponding volumetric flow is Equation A.9, as shown in Figure A.2.2.

$$E = 2\sigma\Delta y\int_0^b \left(W_1 z'^5 + \sqrt{1+z''^2} + \cos\theta\right)\mathrm{d}x \tag{A.8}$$

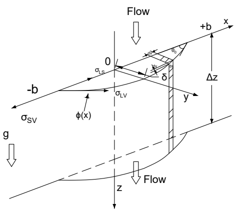

(a) Liquid flow in a rivulet

(b) Force acting on a liquid rivulet

(c) Change in dimension of a stale rivulet with liquid flow rate(Q_1<Q_2<Q_3)

Figure A.2.3: A stable liquid rivluet flowing down an isothermal vertical wall

$$Q = \frac{2}{3}\frac{\rho g}{\mu}\int_0^b z^3 \mathrm{d}x \tag{A.9}$$

and then the Equations are calculated resulting Equation A.10

$$\delta = \left(\frac{45}{7}\right)^{1/5}\left(\frac{\mu^2\sigma}{\rho^3 g^2}\right)(1-\cos\theta)^{1/5} \tag{A.10}$$

Also, the corresponding wetting rate is

$$\gamma = \frac{1}{3}\left(\frac{3}{5}\right)^{3/5}\left(\frac{\rho\mu}{g}\right)^{1/5}\sigma^{3/5}(1-\cos\theta)^{3/5} \tag{A.11}$$

In [5], a similar model of rivulet as shown in Figure A.2.3. Also, the kinetic energy $\mathrm{d}e_{\mathrm{k}}$ per unit length of the rivulet is given as Equation A.12

$$\mathrm{d}e_{\mathrm{k}} = \left(\int_0^\delta \frac{\rho}{2}u^2(x,y)\right)\mathrm{d}x \tag{A.12}$$

and the total energy e_{tot} is given as A.13

$$e_{\mathrm{tot}} = 2\int_0^b \left[\left(\int_0^\delta \frac{\rho}{2}u^2 \mathrm{d}y\right) + \left(\sigma\sqrt{1+\left(\mathrm{d}\phi/\mathrm{d}x\right)^2}\right) - \sigma\cos\theta + \sigma_{\mathrm{SV}}\right]\mathrm{d}x \tag{A.13}$$

And after determination of the velocity distribution using Ritz method, the velocity distribution in the liquid rivulet as Equation A.14

$$U(X,Y) = \sum_{i=1}^{3} c_i \cos\frac{2i-1}{\alpha} 2X \sin i\alpha Y \tag{A.14}$$

and finally the dimensionless MWR Γ_{min} is given as A.16

$$\Gamma_{\text{min}} = (15)^{3/5}(\Delta_{\text{min}})^3 \int_0^1 \sum_{i=1}^{3} \frac{c_i}{i\alpha} \cos\frac{(2i-1)\alpha}{2} X \times (1-\cos i\alpha\Phi(X))\,\mathrm{d}X \tag{A.15}$$

After evaluated numerically, the dimensionless MWR Γ_{min} and dimensionless MLFT Δ_{min} could be expressed as Equation A.16 and A.17

$$\Gamma_{\text{min}} = 0.67\Delta_{\text{min}}^{2.83} + 0.26\Delta_{\text{min}}^{9.51} \tag{A.16}$$

$$\Delta_{\text{min}} = (1-\cos\theta)^{0.22} \tag{A.17}$$

NOMENCLATURE

Name	**Description**
A	Experimental correlated coefficients A.7 [-]
b	Rivulet half-width [m]
c	Dimensionless coefficient [-]
D	Mass diffusivity coefficient [$\mathrm{m}^2 \cdot \mathrm{s}^{-1}$]
e	Energy [$\mathrm{J} \cdot \mathrm{m}^{-1}$]
E	Dimensionless energy $\frac{e}{\sigma}$
g	Acceleration of gravity [$\mathrm{m} \cdot \mathrm{s}^{-2}$]
i	Sequence of numbers [-]
K	Experimental correlated coefficients A.7 [-]
K_1	Experimental correlated coefficients A.6 [-]
m	Measured value [-]
n	Repeat times [-]
Q	Dimensionless flow rate $\frac{\gamma\mu}{\rho\sigma^3 g b}$ [-]
R	Reaction force [-]
Re	Reynolds number $\frac{4\gamma}{\mu}$ [$-$]
T	Temperature [°C]
u	Velocity [$\mathrm{m} \cdot \mathrm{s}^{-1}$]
$\bar{u}$	Mean velocity [$\mathrm{m} \cdot \mathrm{s}^{-1}$]
U	Dimensionless velocity $\frac{u\mu}{g\rho\sigma^2}$ [-]
W_1	Experimental correlated coefficients A.8 [-]
x, y, z	Coordinate direction [m]
X, Y	Dimensionless length $\frac{x}{b}, \frac{y}{\sigma}$
z', z''	Experimental correlated coefficients A.8 [-]
Greek letter	**Description**
α	Damping coefficient [-]
γ	Mass flow rate [$\mathrm{kg} \cdot \mathrm{m}^{-1} \cdot \mathrm{s}^{-1}$]
Γ	Dimensionless mass flow rate$\frac{\gamma}{(\rho\mu\sigma^3/g)^{\frac{1}{5}}}$
δ	Mean film thickness [m]
Δ	Dimensionless film thickness$\sigma(\rho^3 g^2/15\mu^2\sigma)^{\frac{1}{5}}$
ε	Relative error [$-$]
σ	Surface tension [$\mathrm{mN} \cdot \mathrm{m}$]
ϕ	Rivulet profile [m]
Φ	Dimensionless rivulet profile ϕ/δ [-]
θ	Dynamic viscosity [$\mathrm{Pa} \cdot \mathrm{s}^{-1}$] [-]
μ	Contac angle [°]
ρ	Density [$\mathrm{kg} \cdot \mathrm{m}^{-3}$]

Abbreviation	**Description**
MWR	Minimum wetting rate
MLFT	Minimum liquid film thickness
MTE	Minimum total energy
Subscripts & Superscripts	**Description**
i	Subscript index
k	Kinetic
min	Minimum
tot	Total
SV	Solid-vapour

References

[1] R. J. Moffat, Describing the uncertainties in experimental results, Experimental Thermal and Fluid Science 1 (1) (1988) 3–17. `doi:10.1016/0894-1777(88)90043-X`.

[2] A. B. Ponter, G. A. Davies, T. K. Ross, P. G. Thornley, The influence of mass transfer on liquid film breakdown, International Journal of Heat and Mass Transfer 10 (3) (1967) 349–352. `doi:10.1016/0017-9310(67)90151-2`.

[3] T. Munakata, K. Watanabe, K. Miyashita, Minimum wetting rate on wetted-wall column, Journal of Chemical Engineering of Japan 8 (6) (1975) 440–444.

[4] A. Doniec, Flow of a laminar liquid film down a vertical surface, Chemical Engineering Science 43 (4) (1988) 847–854. `doi:10.1016/0009-2509(88)80080-0`.

[5] M. S. El-Genk, H. H. Saber, Minimum thickness of a flowing down liquid film on a vertical surface, International Journal of Heat and Mass Transfer 44 (15) (2001) 2809–2825. `doi:10.1016/S0017-9310(00)00326-4`.